

ABSTRACT

KLEINERT, JAIRUS MATTHEW. Liquid Transport and Colloidal Self Assembly in Thin Wetting Films Driven by Electric Fields. (Under the direction of Dr. Orlin D. Velev).

Three systems in which electric fields are used to control the flow of liquid in thin wetting films are presented. First, a new technique that combines evaporative convective deposition of colloidal crystal coatings with an electric field to achieve more rapid assembly and reduce the occurrence of defects in the crystal structure is reported. When an ac voltage was applied across the particle suspension and the substrate in the convective assembly process, a longer film spread from the meniscus by the electrowetting effect. The data suggest that the electrowetting-increased liquid surface area resulted in increased evaporation-driven particle flux and crystal assembly that was up to five times more rapid than without voltage applied. The extended drying film also provided more time for particle rearrangement before the structure became fixed, resulting in formation of crystal domains an order of magnitude larger than those deposited by convective assembly alone. The results demonstrate that electrowetting is a facile tool for controlling particle assembly processes in wetting films. The technique could be used in improved large-scale colloidal crystal coating processes.

Second, oil films that separate water droplets from solid surfaces in microfluidic systems are examined during actuation of droplets using an electric field. The films are critical to lubrication of droplet motion and prevention of fouling of the devices. The factors that determine whether the films rupture or remain stable when translational droplet transport is driven by electrowetting are not yet thoroughly understood but were experimentally investigated in this study. The experiments were performed using a standard digital

microfluidic cartridge in which water droplets were enclosed in an oil-filled gap over an array of electrodes. Programmable electrode switching sequences actuated two-dimensional droplet motion driven by electrowetting. Stable, continuous oil films separated the droplets from the surfaces when the droplets were stationary. During droplet transport, waves trailed the receding oil meniscus in the film over the electrode-embedded surface. The waves evolved into semispherical oil lenses. Droplet deformation and oil displacement caused the film at the surface above the droplet to transform into a dimple of oil. Lower actuation voltages were associated with slower film thinning and fewer but larger oil lenses. Lower frequencies induced vibrations in the droplets that caused the films to rupture. Films were also destabilized by addition of surfactants to the oil or droplets. The understanding of oil film behavior provided by this work will enable more robust electrowetting-actuated lab-on-a-chip devices through minimization of molecular transfer between droplets.

Finally, a novel nanofluidic system based on electroosmotic flow in nanoscale-thin aqueous wetting films is described. The water films formed spontaneously on mica substrates in a saturation humidity environment. The film thickness was determined to be a few tens of nanometers by optical interference and fluorescence intensity measurements and was consistent with a theoretical evaluation of the thickness of a film based on the competing forces of electrostatic repulsion and capillary pressure. Lateral flow was induced by applying a dc electric field tangential to the film and characterized by tracking the position of a fluorescent probe. The mobilities of the thin fluid layer and the flow marker were lower than the predictions of electrokinetic theory, which may be a result of adsorption of the fluorescent molecules to the mica. Confinement of the film to two-dimensional “channels” was achieved by microcontact printing of patterned hydrophobic monolayers onto the

substrate. This system has the advantage of simple and inexpensive fabrication in comparison to nanofluidic devices made by traditional lithography techniques.

Liquid Transport and Colloidal Self Assembly in
Thin Wetting Films Driven by Electric Fields

by
Jairus Matthew Kleinert

A dissertation submitted to the Graduate Faculty of
North Carolina State University
in partial fulfillment of the
requirements for the degree of
Doctor of Philosophy

Chemical Engineering

Raleigh, North Carolina

2013

APPROVED BY:

Orlin D. Velev
Committee Chair

Jan Genzer

Michael Dickey

Glenn M. Walker

Sergei Sheiko

BIOGRAPHY

Jairus Kleinert was born on May 18, 1984 in Grand Rapids, Michigan to John and Karen Kleinert, a chemical engineer and a teacher. He was raised in Livingston County, Michigan with his sister Anna and brothers, Jonathan and Benjamin. While attending high school near Charlotte, North Carolina, Jairus realized that his deepest interests were in the fields of chemistry and biology. Upon enrolling as an undergraduate at Michigan State University (MSU), he elected to major in chemical engineering, attracted to a curriculum that emphasized using knowledge of the physical world to solve significant problems in practical ways. Throughout his time at MSU, Jairus worked in the research lab of Professor Robert M. Worden, developing novel biosensors and catalysts based on redox enzymes. After earning his bachelor's degree, he began graduate school at North Carolina State University, studying colloid science under Professor Orlin D. Velev. With an interest in microfluidic devices, Jairus performed some of his dissertation work at Advanced Liquid Logic (ALL), a newly established, local company developing a lab-on-a-chip platform based on electrowetting. Jairus has continued working at ALL and is now developing microfluidic assays that are enabling expanded screening and early treatment of newborns for several potentially debilitating conditions.

ACKNOWLEDGMENTS

I am grateful to the many people who have contributed to my endeavors in graduate school. From the beginning, my family has supported my education and encouraged my aspirations. Significant sacrifices by parents and grandparents over the years have opened critical opportunities to me.

Several excellent teachers have prepared me for graduate research. Recognition is especially due to Tradd Medford, my high school chemistry and physics teacher, who kindled my early interest in science, and Professor Worden, my undergraduate advisor, who generously hired me when I knew very little and taught me what doing research really means.

The distinguished and collegial faculty and helpful staff at North Carolina State University have contributed greatly to my learning. I have been especially influenced by Professors Genzer, Walker, and Dickey, who have served on my committee, taught interesting courses, and contributed professional advice. The support of Professor Kelly through the Molecular Biotechnology Training Program has added a valuable dimension to my expertise. Sandra Bailey has been indispensable in navigating the various university departments and procedures.

My graduate research experience has been enriched by interactions with faculty and colleagues and at other institutions as well. In the Department of Chemistry at the University of North Carolina at Chapel Hill, Michael Barrett and Professor Sheiko engaged with us in a stimulating collaboration on polymer flows. Abigail Turner, Jacob Grohman, and Professor Allbritton provided valuable assistance with electrokinetic measurements. At Advanced Liquid Logic, Pallavi Daggumati and Ryan Sturmer supported my research with expertise in

lithography and electrical engineering. Arnaud Rival and Cyril Delattre shared complementary observations of droplet dynamics. Ramakrishna Sista and Theodore Winger provided useful advice. Vijay Srinivasan welcomed me to the company and is a reservoir of electrowetting knowledge.

Working with the talented assembly of researchers in the Velev Group has been a privilege. The senior graduate students and postdocs—Brian Prevo, Ketan Bhatt, Daniel Kuncicky, Shalini Gupta, Suk Tai Chang, Lindsey Jerrim, Vinayak Rastogi, Sumit Gangwal, Bridgette Budhlall, Stoyan Smoukov, and Elena Blanco—have been role models of uncommon intelligence, dedication, and kindness. I am especially grateful to Sejong Kim who helped me to begin my experiments. The camaraderie among my contemporaries in the group—Elizabeth Melvin, Hyung Jun Koo, Jessica Jenkins, Burak Uçar, Rachita Sharma, Stephanie Lam, and Tian Tian—is deeply appreciated.

My friends at NCSU, Matthew Anderson, Christopher Bonino, Jeremy Palmer, Sara Arvidson, Michelle Casper, Kristen Roskov, and Joshua McClure, have made the past six years happy ones.

Finally, two excellent mentors have been chiefly responsible for my intellectual and professional development during graduate school. Vamsee Pamula, who has overseen my research at Advanced Liquid Logic, has motivated me with his passion and energy, challenged me to think more quickly with his countless questions, and inspired me with his commitment to improve the lives of other people. Above all, my advisor, Professor Velev has provided consistent and essential support. He has encouraged me with his irrepressible enthusiasm and hard work, deepened my appreciation for science with his remarkable

creativity, and guided my work with graciousness and patience. He will always have my deepest appreciation and admiration.

TABLE OF CONTENTS

LIST OF TABLES	viii
LIST OF FIGURES	ix
Chapter 1: Introduction to Wetting Films, Electric Field Effects, Microfluidics, and Colloidal Self Assembly	1
1.1 Introduction	1
1.2 Wetting Films	2
1.2.1 <i>Wetting Thermodynamics</i>	2
1.2.2 <i>Disjoining Pressure</i>	4
1.2.3 <i>External Forces</i>	8
1.3 Electric Field Effects in Colloidal Systems	9
1.3.1 <i>Electrophoresis and Electroosmosis</i>	9
1.3.2 <i>Dielectrophoresis</i>	11
1.3.3 <i>Electrowetting</i>	12
1.4 Microfluidics	15
1.4.1 <i>Applications</i>	15
1.4.2 <i>Physics of Microscale Flow</i>	18
1.4.3 <i>Microfabrication</i>	21
1.4.4 <i>Device Configurations</i>	23
1.4.5 <i>Nanofluidics</i>	25
1.5 Colloidal Self-Assembly	26
1.5.1 <i>Applications</i>	26
1.5.2 <i>Assembly Driven by External Fields</i>	29
1.5.3 <i>Assembly Driven by Solvent Flow</i>	30
1.5.4 <i>Assembly Driven by Molecular Interactions</i>	32
1.5.5 <i>Assembly with Anisotropic Particles</i>	33
1.6 Overview of Dissertation	34
1.7 References	35
Chapter 2: Electric-Field-Assisted Convective Assembly of Colloidal Crystal Coatings	50
2.1 Introduction	50
2.2 Materials and Methods	51
2.2.1 <i>Materials</i>	51
2.2.2 <i>Coating Deposition</i>	52
2.2.3 <i>Characterization of the Coatings</i>	54
2.3 Results and Discussion	55
2.3.1 <i>Effect of Applied Voltage on Coating Deposition Rate</i>	55

2.3.2 <i>Effect of Electric Field on Crystal Uniformity</i>	64
2.4 Conclusions	69
2.5 References	70
Chapter 3: The Dynamics and Stability of Lubricating Oil Films During Droplet Transport by Electrowetting in Microfluidic Devices	72
3.1 Introduction	72
3.2 Materials and Methods	77
3.2.1 <i>Microfluidic Cartridge Construction</i>	77
3.2.2 <i>Liquid Phase Materials</i>	79
3.2.3 <i>Electrical Instrumentation</i>	79
3.2.4 <i>Characterization</i>	80
3.3 Results	81
3.3.1 <i>Static Oil Films</i>	81
3.3.2 <i>Oil Films Formed During Stationary-Droplet Electrowetting</i>	83
3.3.3 <i>Dynamics of Oil Films During Electrowetting-Driven Droplet Transport</i>	84
3.3.4 <i>Effects of Voltage Magnitude and Frequency</i>	88
3.3.5 <i>Effects of Surfactants</i>	92
3.4 Discussion	94
3.5 Conclusions	101
3.6 References	102
Chapter 4: Electric-Field-Controlled Flow in Nanoscale-Thin Wetting Films	104
4.1 Introduction	104
4.2 Materials and Methods	105
4.2.1 <i>Flow System Construction</i>	105
4.2.2 <i>Characterization of Wetting Films and Flow Behavior</i>	109
4.3 Results	110
4.3.1 <i>Initial Demonstration of Wetting Film Formation and Flow</i>	110
4.3.2 <i>Measurement of Film Thickness</i>	112
4.3.3 <i>Measurement of Electroosmotic Mobility</i>	115
4.4 Discussion	120
4.5 Conclusions	125
4.6 References	126
Chapter 5: Summary and Outlook	129
5.1 Summary	129
5.2 Outlook	131
5.3 References	134

LIST OF TABLES

Table 3.1. Effect of voltage magnitude and frequency on droplet transport and oil film evolution.....	89
Table 3.2. Effect of surfactant concentration on droplet-oil interfacial tension and film behavior.....	93

LIST OF FIGURES

Figure 1.1. Schematics of partial and complete wetting configurations of a liquid on a solid substrate and contributions to disjoining pressure that determine wetting film thickness.....	3
Figure 1.2. Schematic depiction of the electric field effects that are operative in microscale systems.....	11
Figure 1.3. Composite of schematics and images of microfluidic devices.....	20
Figure 1.4. Images of colloidal assemblies.....	29
Figure 1.5. Schematic of convective assembly coating deposition process.....	32
Figure 1.6. Images of colloidal assemblies from anisotropic particles.....	34
Figure 2.1. Schematics of the apparatus used to deposit colloidal crystal coatings by convective assembly in an electric field.	53
Figure 2.2. Plot of the average thicknesses of crystal coatings deposited with different voltages applied.....	58
Figure 2.3. Schematic of the parameters for the model of voltage-driven extension of the particle suspension drying film.....	60
Figure 2.4. Images of crystal domains in coatings deposited with and without an electric field and optical micrograph showing individual particles in a crystal coating deposited without an electric field and the alignments of domains.....	65
Figure 2.5. Histogram comparing the sizes of crystal domains in coatings deposited with and without an electric field.....	67
Figure 2.6. Histogram comparing the alignments of crystal domains in coatings deposited with and without an electric field.	68
Figure 3.1. Schematic illustrating side and top view of electrowetting-actuated microfluidic device.	78
Figure 3.2. Schematic and interference micrograph showing a thin film between a droplet and cartridge surface before voltage was applied.....	82

Figure 3.3. Schematics and interference micrographs showing the evolution of an oil film between a stationary droplet and the electrowetting surface after voltage was applied.....	84
Figure 3.4. Top view and side view images and schematics showing the evolution of the oil films and droplet shape as a droplet was transported along a path of individual electrodes by electrowetting.	86
Figure 3.5. Images and schematic showing the evolutions of the oil films at the reference and electrowetting surfaces when droplets were transported at 100 V.....	90
Figure 3.6. Images and schematic showing how the evolutions of the oil films at the reference and dielectric-coated surfaces change when a 10 Hz ac voltage is used to transport droplets instead of a standard 100 Hz ac signal.....	91
Figure 3.7. Images and schematic showing the evolution of the oil film at the electrowetting surface when surfactant (Tween-20) is added to a droplet at concentrations of 0.003% and 0.1%.	94
Figure 4.1. Schematic of the nanoscale-thin wetting film flow system.	106
Figure 4.2. Schematic of the creation of two-dimensional channels by microcontact printing and flow through the channels.	107
Figure 4.3. Brightfield and fluorescence micrographs showing interference fringes indicating the transition between a droplet and a thin film and a thin film containing dye flowing through a two-dimensional channel.....	112
Figure 4.4. Plot of the light intensity from an image of an interference pattern at the transition from a droplet to a thin film presumed to be in the zeroth order of interference.	114
Figure 4.5. Example of fluorescence micrographs and plots used to estimate the velocity of marker motion in the wetting film.	117
Figure 4.6. Plot of film electroosmotic mobility versus electric field strength for the nanoscale-thin film flow system.	120
Figure 4.7. Schematic of the physical principles of film formation and electroosmotic flow.	121
Figure 5.1. Atomic force micrograph of polymer brushes moving along the wall of a “virtual channel.”	134

Chapter 1

Introduction to Wetting Films, Electric Field Effects, Microfluidics, and Colloidal Self Assembly

1.1 Introduction

Wetting films, thin layers of liquid covering solid substrates, have been studied for over a century¹ and are present in countless systems. In daily life, wetting films can be seen when rain falls on a roadway or when a soapy solution is used to wash a window. In the human body, the mucus layers that line the lungs² and protect the eye³ are examples of wetting films. Industrially, wetting films feature prominently in coating,⁴ lubrication, and chemical processing systems. Recent developments in microscale engineering and attention to nanotechnology give new significance to wetting films, which often have thicknesses in the micrometer and nanometer range. Wetting films are often present in microfluidic systems, either as the primary vehicle for liquid transport or as a layer surrounding droplets or bubbles moving in a continuous phase.

Electric fields are commonly used to manipulate liquids and particles in colloidal systems.^{5,6} The motion of charged particles through liquid and liquid through charged capillaries in dc fields was first observed over two centuries ago.⁷ Techniques for manipulating particles⁸ and liquids^{9,10} in ac fields have come into use more recently. Separation of DNA by electrophoresis has enabled dramatic advances in molecular biology in the past several decades. Electric field effects have been widely implemented to drive flow in microfluidic devices.¹¹ Also, many techniques for assembly of materials rely on electric fields to direct the organization of micro- or nanoparticles.¹²

Because electric fields are convenient for manipulating nanometer to micrometer objects, they could provide a powerful route to controlling processes in thin films with thicknesses at the same scale. However, there are not many examples of systems taking advantage of both wetting film properties and electric field effects, and the number of studies about the effects of electric fields on wetting films is limited. This dissertation presents three novel systems in which wetting films are manipulated by applied electric fields, including a method for assembly of coatings that are structured at the microscale in films of which the shape is controlled by an electric field, a microfluidic device in which droplet movement is lubricated by wetting films and actuated by electric fields, and a platform in which flow in a nanoscale-thin wetting films is driven by an electric field, demonstrating a concept that may be useful for manipulating individual molecules. First, however, the basic physics of wetting films and electric field effects in colloidal systems and research in the fields of microfluidics and colloidal self-assembly are reviewed.

1.2 Wetting Films

1.2.1 Wetting Thermodynamics

Liquid deposited on top of a horizontally-oriented solid surface takes one of two configurations depending on the energies of the interfaces between the drop, the surface, and the ambient phase, which may be a gas or immiscible liquid. If the sum of the drop-solid and drop-ambient phase interfacial energies is larger than the solid-ambient phase interfacial energy, then the energy of the system will be minimized with the drop only partially wetting the surface and retaining a semispherical shape with a finite contact angle at the three-phase

contact line, as depicted in Figure 1.1a. Otherwise, the drop will spread and flatten to completely cover the solid in the form of a wetting film, as in Figure 1.1b. The corresponding energies can be compared by calculating the spreading parameter

$$S = \gamma_{SA} - \gamma_{DS} - \gamma_{DA} \quad (1.1)$$

where γ_{SA} , γ_{DS} , and γ_{DA} are the solid-ambient, droplet-solid, and droplet-ambient phase interfacial energies, and the partial wetting and complete wetting states are represented by $S < 0$ and $S > 0$. The contact angle at the periphery of a partially wetting drop is given by the Young equation,

$$\cos \theta = \frac{\gamma_{SA} - \gamma_{DS}}{\gamma_{DA}} \quad (1.2)$$

The forces governing the thickness of the film in a complete wetting state are discussed in the next section.

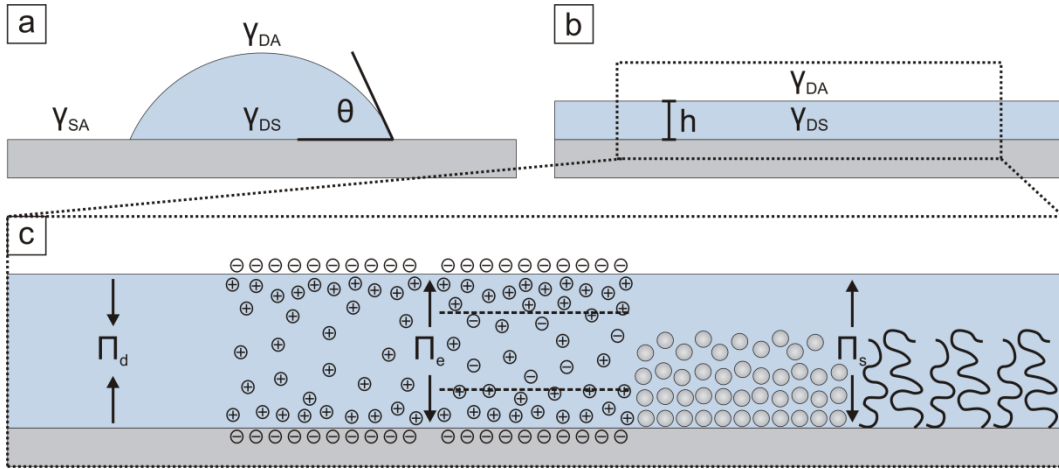


Figure 1.1. Schematics of (a) partial and (b) complete wetting configurations of a liquid on a solid substrate and (c) contributions to disjoining pressure that determine wetting film thickness, including (from left to right) van der Waals forces, electrostatic forces without and with electrolyte, oscillatory forces, and polymer interactions.

1.2.2 Disjoining Pressure

The thickness of a wetting film is determined by the disjoining pressure that arises from the intermolecular forces between the solid surface and the free interface where the film and the ambient phase meet. The disjoining pressure Π may have dispersion Π_d , electrostatic Π_e , and structural Π_s components which can be considered additive such that

$$\Pi = \Pi_d + \Pi_e + \Pi_s \quad (1.3)$$

Examples of forces that contribute to the disjoining pressure are depicted in Figure 1.1c.

The dispersion contribution to the disjoining pressure arises from the van der Waals interactions in the system and, for a planar film, can be calculated using

$$\Pi_d = \frac{A}{6\pi h} \quad (1.4)$$

where A is the Hamaker constant, which accounts for the dielectric properties of the phases, and h is the distance between the film surfaces.¹³ The van der Waals forces are repulsive, with $A < 0$, only if the film has an intermediate dielectric permittivity relative to the ambient and solid phases. Otherwise, and as is typically true, the forces are attractive, with $A > 0$, and the dispersion component of the disjoining pressure acts to thin the film.

The electrostatic component of the disjoining pressure is a result of an osmotic effect driven by accumulation of charges at the film surfaces. The charges may result from dissociation of ions from the solid surface or adsorption of species to the solid from the liquid. The fixed charges at the surfaces are balanced by bound and mobile counterions in the liquid to maintain the overall electrical neutrality of the system. The concentration of

counterions ρ and the electrical potential ψ at any distance x from the midpoint of a film between two identically charged surfaces are given by the Poisson-Boltzmann equation,

$$\frac{d^2\psi}{dx^2} = -\frac{ze\rho}{\varepsilon\varepsilon_0} = -\left(\frac{ze\rho_0}{\varepsilon\varepsilon_0}\right)e^{-\frac{ze\psi}{kT}} \quad (1.5)$$

subject to the boundary conditions

$$\left(\frac{d\psi}{dx}\right)_0 = 0 \quad (1.6)$$

$$\left(\frac{d\psi}{dx}\right)_{h/2} = \frac{\sigma}{\varepsilon\varepsilon_0} \quad (1.7)$$

where z is the ion valency, e is the charge of an electron, ε is the dielectric constant of the film, k is the Boltzmann constant, T is the temperature, σ is the surface charge density, and the subscripts 0 and $h/2$ denote the midplane of the film and the film surfaces, respectively.¹³

The solution to eq 1.5 is

$$\psi = \left(\frac{kT}{ze}\right) \log(\cos^2 Kx) \quad (1.8)$$

where

$$K^2 = \frac{(ze)^2 \rho_0}{2\varepsilon\varepsilon_0 kT} \quad (1.9)$$

The entropy of the system is increased by the diffusion of the counterions away from the surface and each other, and, thus, the film becomes thicker as the surface charge and the concentration of counterions increase. For a film of pure liquid, the repulsion can be calculated from the osmotic pressure using

$$\Pi_e = kT\rho_0 \quad (1.10)$$

where ρ_0 can be determined from the Poisson-Boltzmann equation if h and σ are known.¹³

Most films contain electrolyte, and the additional ions from their dissociation suppress some of the repulsive effects of the counterions. The charge distribution and electrical potential of the film may still be described by the Poisson-Boltzmann equation as long as terms are added for each ionic species i such that

$$\frac{d^2\psi}{dx^2} = -\frac{\sum_i z_i e \rho_i}{\epsilon \epsilon_0} \quad (1.11)$$

Approximations are required to calculate the repulsion from this more complex version of the Poisson-Boltzmann equation. The most commonly used is the Guoy-Chapmann theory,¹³ which gives

$$\Pi_e = 64kT \rho_\infty \left[\tanh\left(\frac{ze\psi_{h/2}}{4kT}\right) \right]^2 e^{-\kappa h} \quad (1.12)$$

Here, ρ_∞ is the concentration of electrolyte far from the surface and

$$\kappa = \left(\sum_i \frac{\rho_{\infty i} e^2 z_i^2}{\epsilon \epsilon_0 kT} \right)^{\frac{1}{2}} \quad (1.13)$$

The Debye length $1/\kappa$ approximates the distance that the counterion layer extends from the surface.

An additional complicating factor for wetting films is that the solid-liquid and liquid-ambient interfaces likely have different potentials while the standard models assume a symmetric system. For an electrostatically asymmetric film, the repulsion may be calculated

using approximate analytical equations¹⁴ or numerical solutions¹⁵ for the Poisson-Boltzmann equation.

Structural contributions to the disjoining pressure exist because of steric effects of the molecules in the film or ordering of the molecules. The effects are typically short ranged, acting within a few molecular diameters of the surface, and include the oscillatory force, the hydration force, the hydrophobic force, and polymer interactions. The oscillatory force arises from the tendency of molecules to align at a solid surface. The molecules become oriented such that they are most likely to be located with their centers at the distance from the surface matching the molecular radius with decreasingly well aligned layers extending out from the surface. If the film thickness is no greater than a few times the diameter of the molecules, a pressure arises between the film surfaces that is either repulsive or attractive if the thickness is a multiple of the size of the molecules and thus promotes ordering of the molecules into layers and a low entropy state or if the thickness is between multiples of the size of the molecules and thus disrupts the ordering and promotes a high entropy state.¹³

The disjoining pressure becomes predominantly repulsive or attractive with high or low affinity of the molecules in the film for the surface, which enhances or suppresses the ordering.¹³ Hydration forces are active when the surface is hydrophilic and the molecules in the film have ionic groups or hydrogen bonding groups that engender a high affinity between the liquid and the surface. Hydrophobic forces drive the film surfaces together and the liquid out if the surfaces and liquid have low affinity for each other.

Polymers that are grafted or adsorbed to the surfaces can promote either film thickening or thinning depending on their affinity for the liquid.¹³ If the liquid is a good

solvent for the polymer, the polymer will extend into the film and prevent thinning by steric repulsion. If the liquid is a poor solvent, the polymer will form a coil and the surfaces may be attracted to each other by the hydrophobic force. If the polymer has affinity for both surfaces but is initially attached to only one surface, it may form attractive bridges by attaching to the opposite surface.

1.2.3 External Forces

In some systems, external forces may affect the film thickness. Gravity acts on every practical system, but it is likely to be insignificant for most thin wetting films. The Bond number evaluates the ratio of gravitational to surface forces in a system and is given by

$$Bo = \frac{\Delta\rho gh}{\gamma} \quad (1.14)$$

where $\Delta\rho$ and γ are the density difference and interfacial tension between the film and the ambient phase and g is the gravitational acceleration. Even for a horizontally-oriented thick film in air and with low interfacial tension, assuming $\Delta\rho = 1000 \text{ kg/m}^3$, $h = 100 \text{ }\mu\text{m}$, and $\gamma = 1 \text{ mN/m}$, $Bo = 0.1$, while gravity is assumed to be insignificant for $Bo < 1$.

In contrast, an electrical field applied normal to the film surface may be sufficiently strong to affect the shape and thickness of the film. If a film is supported on an electrode, the liquid can be attracted to a second oppositely charged or polarized electrode some distance above the film.^{16,17} The effect arises from charge accumulation at the surface of a conducting film or polarization of an insulating film, and may result in semispherical deformations in the free interface of the film or columnar liquid structures connecting the film to the distant electrode, depending on the intensity of the electric field relative to the energy of the free

surface of the film. Other electric field effects, which may be useful as a means of driving liquid, molecular, or colloidal particle transport in a film, are discussed in the next section.

In some systems, a wetting film may exist in equilibrium with a drop of liquid so that a meniscus forms where the drop meets the film. A capillary pressure arises from the curvature of the meniscus that acts to drain the film. The capillary pressure can be calculated from the Laplace equation

$$P_c = \frac{\gamma}{R} \quad (1.15)$$

where γ is the surface tension of the film and droplet and R is the radius of the meniscus, assuming that the meniscus is linear. In this case, the disjoining pressure is balanced by the capillary pressure to determine the film thickness.

1.3 Electric Field Effects in Colloidal Systems

1.3.1 Electrophoresis and Electroosmosis

The related effects of electrophoresis and electroosmosis can be employed to transport colloidal particles through liquid or liquids through capillaries.⁵ The effects arise from electrostatic forces acting on surface charges in a dc electric field. A particle suspended in liquid typically acquires surface charges and is surrounded by a layer of counterions. When a dc electric field is applied across the system, the counterions partially migrate to the side of the particle facing the electrode with the opposite charge. The movement of the ions creates a flow that pushes the particle in the opposite direction, as illustrated in Figure 1.2a. When a solid surface is stationary but in contact with a mobile liquid, such as in a liquid-

filled capillary, the counterions along the charged surface are also drawn toward the oppositely charged electrode when a dc field is applied. The ions moving along the surface drag the bulk liquid, engendering a plug flow, as shown in Figure 1.2b. The speed of a particle or liquid flow is characterized by the electrophoretic or electroosmotic mobility

$$\mu = \frac{U}{E} \quad (1.16)$$

which relates the velocity of the particle or liquid U to the electric field strength E . The mobility is constant in ideal systems. For particles, the electrophoretic mobility depends on the ratio of κ/D where D is the diameter of the particle. At the limit where $\kappa \ll D$, the mobility can be estimated using the Helmholtz-Smoluchowski equation

$$\mu = \frac{\varepsilon\varepsilon_0\zeta}{\eta} \quad (1.17)$$

where ζ is the zeta potential of the particle, the experimentally measurable electrical potential at the boundary between the bound and mobile counterions, and η is the viscosity of the liquid. The same equation holds true for the electroosmotic mobility of a liquid in a capillary. At the limit where $\kappa \gg D$, the electrophoretic mobility can be estimated using the Hückel-Onsager equation

$$\mu = \frac{2\varepsilon\varepsilon_0\zeta}{3\eta} \quad (1.18)$$

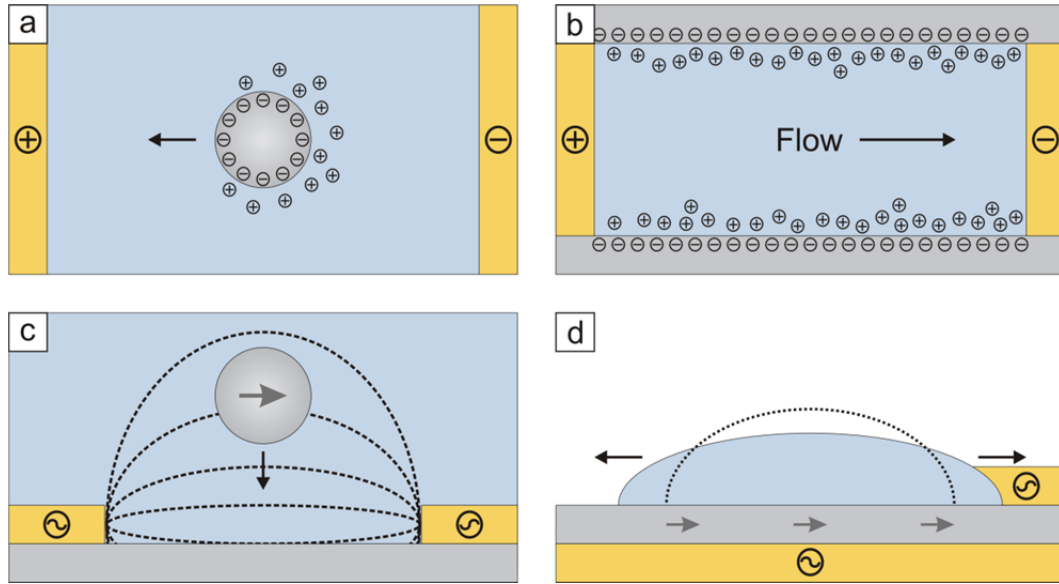


Figure 1.2. Schematic depiction of the electric field effects that are operative in microscale systems, including (a) electrophoresis, (b) electroosmosis, (c) dielectrophoresis, and (d) electrowetting.

1.3.2 Dielectrophoresis

An alternative method for transporting colloidal particles or liquids is dielectrophoresis, which affects materials in ac electric fields on the basis of their relative polarizabilities.⁸ A particle in an ac field acquires an induced dipole. If the field is nonuniform, the particle moves into or away from the area of highest field intensity depending on if the particle is more or less polarizable than the surrounding media. Figure 1.2c depicts a highly polarizable particle in a less polarizable liquid moving to the high electric field intensity between two electrodes. The dielectrophoretic force on a particle or droplet is given by the equation

$$F_{DEP} = 2\pi\epsilon_p R^3 C \nabla E^2 \quad (1.19)$$

where C is the Clausius-Mossotti function

$$C = \frac{\varepsilon_M - \varepsilon_P}{\varepsilon_M + \varepsilon_P} \quad (1.20)$$

ε_P and ε_M are the dielectric constants of the particle and medium, and ∇E is the electric field gradient. Dielectrophoresis is advantageous compared to electrophoresis because particles may be manipulated without also generating electroosmotic flow and because electrolysis may be avoided by using an ac field.

1.3.3 Electrowetting

Electrowetting is a method for moving liquid and controlling the shapes of droplets using electric fields. Originally, electrowetting was performed with water on metal electrodes.¹⁰ A voltage applied between the droplet and the electrode causes charges to accumulate at the liquid-electrode interface and lowers the effective interfacial energy so that the droplet spreads and wets more of the electrode area. The occurrence of electrolysis limits the usefulness of this system. More recently, electrowetting has been demonstrated on an electrode coated by a thin dielectric layer.^{10,18} The insulator blocks the transfer of charge from the electrode to the liquid, permitting operation at higher voltages where the effect is more significant. The voltage drop occurs primarily over the dielectric layer, as the droplet is assumed to be a perfect conductor. The electric field polarizes the dielectric, increasing its affinity for the polar water molecules and causing the liquid to spread, as shown in Figure 1.2d. The electrowetting force on the three phase contact line in this configuration, which has become the most widely used, is given by

$$F_{EW} = \frac{\varepsilon_D \varepsilon_0}{2d} V^2 \quad (1.21)$$

where ϵ_D and d are the permittivity and thickness of the dielectric layer and V is the applied voltage. The interfacial energy is effectively reduced by application of voltage as given by the Lippmann equation

$$\gamma_{EW} = \gamma_{SD} - \frac{\epsilon_D \epsilon_0}{2d} V^2 \quad (1.22)$$

Reducing the solid-droplet interfacial tension reduces the apparent contact angle of the droplet. By combining the Young and Lippmann equations, the electrowetting contact angle is given by

$$\cos \theta_{EW} = \cos \theta + \frac{\epsilon_D \epsilon_0}{2d \gamma_{SD}} V^2 \quad (1.23)$$

where θ is the contact angle with no voltage applied.¹⁰ However, microscopic observations have indicated that the contact angle is not changed by application of voltage from the prediction of the Young equation, but the electric field near the substrate deforms the droplet to create the macroscopic appearance of contact angle reduction.¹⁹

The equations above describe the electrowetting behavior only up to a certain critical voltage and frequency. Above this saturation voltage, no additional droplet spreading is observed.¹⁰ The effects leading to saturation have not been firmly established. One hypothesis is that charge trapping in the insulating layer lowers the strength of the electric field.²⁰ Another is that air is ionized at the droplet contact line, allowing charge to leak from the liquid and reducing the electrowetting effect.²¹ Saturation has also been attributed to deviation from the assumption of a perfectly conducting droplet and a perfectly insulating dielectric layer which may be expected in any real system.²² There is also a maximum ac

frequency at which electrowetting can be performed. Electrowetting is diminished at high frequencies where the liquid behaves as a dielectric rather than a conductor.¹⁰

A critical component of any electrowetting system is the dielectric film. Desirable coating materials have high dielectric permittivity to maximize the voltage that can be applied without charge transfer across the insulating layer. The material should also be highly hydrophobic to achieve a significant difference in droplet shape between the zero voltage and maximum wetting states. Low contact angle hysteresis is necessary for electrowetting to be reversible. The most commonly used dielectric materials include amorphous fluoropolymers,²³ parylene,²⁴ and polydimethylsiloxane (PDMS).²⁵ Alternative materials with higher dielectric constants which can be deposited in thinner layers, such as silicon dioxide,²⁶ barium strontium titanate,²⁶ and an aluminum oxide layer formed by atomic layer deposition,²⁷ can reduce the voltage required to achieve similar electrowetting behavior as seen at higher voltages with thicker insulators. If not natively hydrophobic, dielectric materials may be coated with a thin layer of fluoropolymer. The contact angle hysteresis can be reduced by immersing the droplet and substrate in an oil phase which infuses the dielectric layer.

Electrowetting has found prominent applications in optics, displays, and bioanalytical devices. A water droplet confined to an oil-filled cell can function as an adjustable optical lens which can be focused by applying voltage to change the shape of the droplet.^{28,29} An electronic reflective display can be created from an array of similar cells. A colored liquid can be switched from a state that covers most of the cell to a state that covers only a fraction of the cell such that it functions as a pixel that can be switched on and off.³⁰ The most

extensive application of electrowetting, however, has been in the field of droplet-based lab-on-a-chip devices, which are described in the following section.

1.4 Microfluidics

1.4.1 Applications

Microfluidic devices are miniaturized flow systems in which liquids are confined in spaces with at least one dimension of less than 1 mm.¹¹ Devices for manipulating small volumes of liquid have been widely championed as “labs-on-chips” performing chemical and biological analyses in units with overall dimensions typically at the centimeter scale. A primary advantage of these systems is that processes can be performed with very small liquid volumes when reagents are expensive or sample volumes are limited. Miniaturization can also permit a high number of process steps or duplicate processes to be integrated into one device, enabling automation of operations and high throughput of samples or assays. Heat transport is faster in small volumes, reducing the time required for analyses. Microfluidics may also enable techniques that are simply not possible in larger-scale systems, such as probing individual cells or molecules, while taking advantage of the unique physics of microscale flows, as discussed in the following section.

Many types of bioanalytical operations have been demonstrated in microfluidic devices. The typical device consists of a channel through which the sample flows between mixers, reaction chambers, separation structures, and detection points where the steps required for the analysis occur. Often the process begins with sample treatment, such as purification of nucleic acids from blood^{31,32} and amplification of DNA by polymerase chain

reaction (PCR).^{33,34} Reactions may occur as liquids flow through channels or are held in larger chambers. The most common separation technique employed in microfluidic devices is electrophoresis, which can be used to separate molecules of different sizes or charges.³²⁻³⁵ By applying the electric field perpendicularly to the flow and positioning outlets for different size molecules at the end of the channel, continuous separations may be performed.³⁶ The sieving matrix may be microfabricated into the device in the form of an array of posts.^{37,38} Virtual posts can be created using dielectrophoresis to repel molecules from the area over an electrode.³⁹ Bacteria⁴⁰ and viruses⁴¹ can be collected on electrodes by dielectrophoresis. Different cell types can be separated by optical trapping⁴² or dielectrophoresis.^{43,44} Cells may be sorted into different channels by switching valves in response to fluorescence readings of individual cells.⁴⁵ Detection of separated species may be achieved by fluorescence or electrochemical⁴⁶ potentials. Immunassays⁴⁷ and DNA hybridization assays^{40,48} have also been demonstrated. Although most lab on a chip devices are targeted for bioanalytical applications, chemical synthesis and purification may also be performed.⁴⁹

Many microfluidic devices have been developed for synthesis of micro- and nanoparticles in addition to lab-on-a-chip applications. Microfluidic reactors for the synthesis of metallic nanoparticles⁵⁰⁻⁵² and silica colloidal particles⁵³ allow precise control over the timing and temperature of the reaction, yielding particles with tight size distribution. Microfluidic devices that generate droplets are particularly applicable for particle synthesis if the droplets can be solidified.⁵⁴ Droplets containing monomer may undergo UV⁵⁵ or thermal⁵⁴ polymerization or interfacial polymerization to form capsules.⁵⁶ Solidification of droplets containing micro- or nanoparticles may occur by evaporation-driven colloidal

crystallization.⁵⁵ Particles may also be created from aqueous gels⁵⁷ and low temperature melting metals.⁵⁴ Shape anisotropic particles may be produced by confining the droplets in channels of different height and width during polymerization.^{54,58} By an alternative method, polymer particles may be created directly in a continuous stream of monomer by UV polymerization with a masked illumination source.⁵⁹ Particles of any shape or pattern matching an opening in an opaque mask will solidify in the liquid stream when the stream is illuminated by light through the mask.⁶⁰

Particles with a variety of complex compositions may be produced by microfluidic devices. Chemically anisotropic particles may be produced by combining two adjacent streams in droplet-generating^{61,62} or masked photopolymerization⁶³ devices so that the resulting droplets and particles consist of two halves made of different materials. Multiple emulsions can be produced by performing a set of droplet-generating steps in series.^{64,65} For instance, a water-in-oil-in-water emulsion may be formed by first generating a sequence of water droplets in an oil stream, and then, from that oil stream, splitting off a series of droplets in a second water stream.⁶⁴ Such devices may be used to produce particles with polymer vesicles^{66,67} that may be useful for transporting cells and proteins by encapsulation⁶⁸ or particles with magnetic cores.⁶⁹

Other less widely implemented applications of microfluidic devices have also been demonstrated. Microfluidic heat exchangers based on channel flow^{70,71} and droplet transport⁷² have been constructed. The small sizes of these devices makes them well suited for cooling integrated circuits. The thin dimensions of microfluidic channels enable even optically transparent heat exchangers.⁷³ Materials embedded with microfluidic channels can

be continuously replenished with chemicals and may be useful for applications such as culturing biological tissues.⁷⁴ If the liquid in the microchannels is polymerizable, the channels can act as a rigid skeleton for a shape-memory material.⁷⁵ Microfluidic devices may have optical applications including tunable waveguides⁷⁶ and filters.⁷³ Liquid-based computers employing microfluidic architectures have even been proposed,⁷⁷ in which droplets in highly repetitive channel structures may act as data bits.⁷⁸

1.4.2 Physics of Microscale Flow

Microscale flow is dominated by viscous and surface forces. One consequence is that the flow is laminar, in contrast to flows of larger volumes, in which inertia leads to turbulent mixing between flow streams with random trajectories. The absence of convection in microfluidic systems means that liquid mixing occurs only by the slower process of diffusion between adjacent, parallel flow streams.¹¹ Laminar flow in microfluidic devices may enable some processes that are not possible in larger scale systems. For instance, fast-diffusing molecules may be separated from slow-diffusing molecules or particles from one stream into an adjacently flowing clean stream,⁷⁹ as depicted in Figure 1.3a. Separations may be performed by transferring particles between coflowing streams using hydrodynamic forces,⁸⁰ optical trapping,^{42,81} dielectrophoresis,^{43,44} magnetophoresis,⁸² or acoustic waves,⁸³ as Figure 1.3b illustrates. Conversely, if different species in two separate streams diffuse together and interact or react, the process can be monitored spatially and quantified.⁸⁴ The effects of different chemicals on a single cell can be tested by transporting multiple chemicals over the

cells in parallel flows.⁸⁵ Surface patterning⁸⁶ and materials fabrication⁸⁷ can be performed at high precision by reaction at the interface between streams containing different reagents.

The laminar flow, on the other hand, presents challenges when rapid mixing and reaction are desired.¹¹ Significant efforts have been made to develop methods for enhancing mixing of liquids in microfluidic devices. Mixing can occur passively as liquids move through specially designed device structures. In a simple example, liquids can be mixed by pumping through a loop. Because the liquid at the center of the channel moves faster than the liquid at the channel walls in pressure-driven flow, the interfacial area between two segments of liquid increases as the liquids travel around the loop together, and the distances required for complete mixing to be achieved by diffusion become smaller.⁸⁸ Serpentine channel routes⁸⁹ and grooves⁹⁰ or wells⁹¹ in channel walls may deform the interface between two coflowing liquids, causing liquid layers to fold over each other and reducing the distance required for diffusive mixing between the two liquids, a process termed chaotic advection. Individual reactions may be confined to droplets^{92,93} or segments of liquid between bubbles⁹⁴ in which circulating flows are engendered by shear as the droplets or segments move along the device walls or a fluid boundary with a viscosity gradient. Active mixing strategies, in which external energy is imparted to the system, have also been demonstrated and include using ultrasonic vibrations⁹⁵ and electric and magnetic field-induced flow vortices.^{96–99}

Microfluidic devices are also characterized by high surface-area-to-volume ratios, which have significant implications for actuating and directing liquid flow. If the surfaces are charged, electroosmotic flow may be induced. Flows can be confined to specific pathways on a surface by patterning hydrophilic and hydrophobic zones.^{100–102} Liquid may be transported

along surface energy gradients that are fixed¹⁰³ or controllable by thermal,¹⁰⁴ electrical,¹⁰⁵ electrochemical,¹⁰⁶ or light-based¹⁰⁷ mechanisms. Liquid can also be moved by capillary forces imposed by the geometry of the device.¹⁰⁸

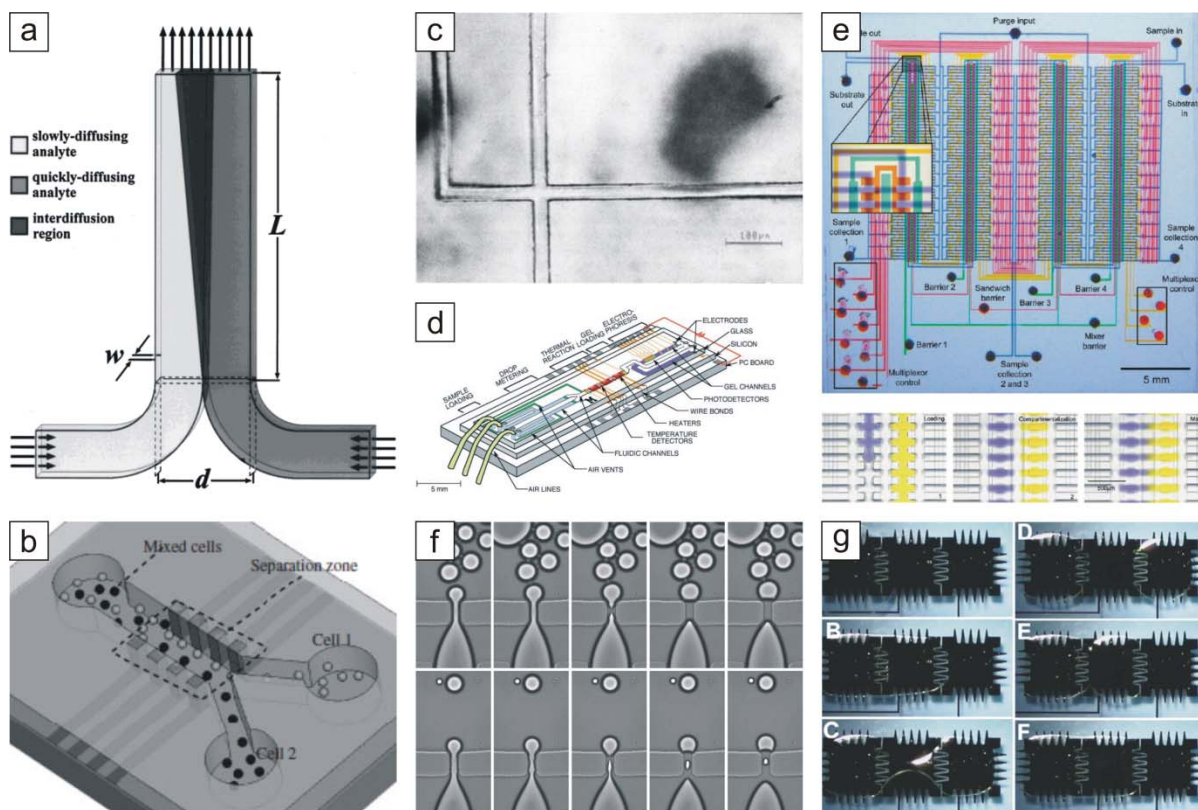


Figure 1.3. Composite of schematics and images of microfluidic devices, including (a) a T-sensor for measuring diffusion between coflowing laminar streams,⁸⁴ (b) a microfluidic system for separations based on dielectrophoresis,⁴⁴ (c) an early glass microfluidic channel used to perform separations by electrophoresis,³⁵ (d) a more advanced microfluidic electrophoresis chip that also performs sample preparation steps,³⁴ (e) a high throughput microfluidic device consisting of an array of parallel channels in which individual reactions can be isolated by pneumatically actuated elastomer valves,¹⁴¹ (f) a flow-focusing aperture in a droplet-generating microfluidic device,¹⁴⁷ and (g) splitting and merging of a droplet in an electrowetting-actuated microfluidic device.¹⁵⁵

1.4.3 Microfabrication

Early microfluidic devices were made using the photolithography and etching methods developed by the integrated circuit industry and were fabricated from silicon^{33,36} or glass.³⁵ An example of such a device is pictured in Figure 1.3c. An advantage of this class of techniques and materials is that fluidic channels with dimensions smaller than 100 nm can be produced readily. However, to create nanoscale features, electron-beam¹⁰⁹ or interferometric lithography¹¹⁰ must be used instead of standard photolithography, or a focused ion beam¹¹¹ or laser¹¹² must be used to directly etch the channels into the surface. These lithography-based methods require multiple complex processing steps, expensive equipment, and clean room facilities.

More economical microfluidic devices have been made from polymer materials, for which simpler and lower cost processing methods are available. One common method is soft lithography, whereby a reusable inverse mold of the desired channel structure is fabricated by traditional photolithography and filled in with a liquid elastomer, usually PDMS, which is then cured and removed from the mold.^{113,114} The method has the advantage of being easy to perform with no complex equipment required after the initial mold is produced. Another method is hot embossing,¹¹⁵ which may also be called nanoimprint lithography¹¹⁶ or step-and-flash imprint lithography.¹¹⁷ In these techniques, the mold is pressed into a liquid polymer coating on a substrate, and the polymer is cured by cooling below the glass transition temperature or photopolymerization by exposure to UV light. Closed channels can be formed by vapor deposition of material over the trenches in the polymer.¹¹⁸ Injection molding of more conventional polymers such as polycarbonate, polymethylmethacrylate, and

cycloolefins is more suitable for mass production of microfluidic devices at low cost but requires a large initial investment in machinery.^{119–120}

Polymer surfaces can be modified by a variety of means to attain properties desirable for a particular application. Microfluidic devices are often enhanced by rendering polymers more hydrophilic than their native states because filling the devices with aqueous solutions becomes easier and liquid transport by electroosmosis becomes more efficient with charged channel walls. Also, hydrophilic surfaces are resistant to fouling with biomolecules that may adsorb due to hydrophobic interactions. In other applications, such as for culturing cells, it is desirable to immobilize proteins on device surfaces.^{121,122} Chemical modification of polymethylmethacrylate and polycarbonate to make more hydrophilic microchannels has been described.^{123,124} Much of the work on controlling surface properties has focused on PDMS. Silane chemistry has been used to obtain PDMS materials with a range of surface energies.¹²⁵ Silica filler material and ion adsorption have been speculated to be sources of surface charge on PDMS.^{126,127} Oxygen plasma¹²⁸ and ultraviolet/ozone¹²⁹ treatments, which create silanol groups, are popular methods for hydrophilization of PDMS. Addition of surfactant to the liquid in the device can also make the surfaces more wettable, enhance electroosmotic flow,^{130,131} and minimize fouling by biomolecules.¹³² Surface functionalization by chemical vapor deposition¹³³ and layer-by-layer adsorption of charged molecules¹³⁴ has also been described.

1.4.4 Device Configurations

Microfluidic devices have been developed in several different formats. The first devices consisted of systems of closed channels through which sample and reagent liquids flowed as different operations were performed in series. Flow through the channels has been driven by electroosmosis³⁵ or external pressure.⁸⁴ An example of such a device is shown in Figure 1.3d.

Repetition of channel structures may enable high throughput applications. One unique type of device in this category is the so-called “LabCD.” This platform features an array of repeating channel structures arranged in a circle around a thin flat plastic disk. When the disk is rotated, the centrifugal force drives the liquid through the channels from the center of the disk to the perimeter.¹³⁵ This platform may be uniquely well suited for processes that can be enhanced by strong gravitational-like forces, such as driving liquid through a chromatography column¹³⁶ or separating blood components¹³⁷ before performing an assay.^{138,139}

Another prominent example of a high-throughput device, shown in Figure 1.3e, consists of two layers of channels in a soft elastomer. Liquid traveling through the channels in one layer can be manipulated by deforming with pressurized air the channels in the other layer.^{140,141} This type of platform is particularly useful for comparing many different experimental conditions, such as for protein crystallization,¹⁴² cell culture,¹⁴³ protein expression by cells,¹⁴⁴ and synthesis of chemical libraries.¹⁴⁵

Another way to achieve high throughput without repeating channel structures is to break up the flow into droplets separated by an immiscible phase. Unique conditions can be

maintained in each droplet, which functions as an individual reactor. Droplets can be formed at a T-junction¹⁴⁶ or by a flow focusing aperture,¹⁴⁷ as shown in Figure 1.3f. Droplets can be combined by merging at a Y-junction¹⁴⁸ or split upon reaching a T-junction or a column in the middle of a channel.^{148,149} Sorting can be performed by using dielectrophoresis to force droplets to one or the other outlet of a Y-junction.¹⁵⁰ Like the parallel channel devices, a variety of applications of the droplet devices have been demonstrated, including kinetics studies,¹⁵¹ protein crystallization,¹⁵² cell culture,¹⁵³ and drug screening,¹⁵⁴ with the goal of comparing a large number of conditions and achieving high throughput.

Another platform for droplet-based microfluidics uses electrowetting to generate and manipulate droplets. Droplets are contained in a slit between two parallel plates where they can be transported in two dimensions. One plate has an array of electrodes beneath a thin dielectric film while the other plate serves as a reference electrode. As the electrodes are sequentially activated, the droplets preferentially wet the dielectric surface where the voltage is applied and move along a pathway.¹⁰⁵ Droplets stretched over multiple electrodes can be split by switching off an electrode in the center, while switching on an electrode between two nearby droplets can cause the droplets to merge. Droplets can be formed by extending a finger of liquid from a reservoir of liquid along several electrodes and then switching off electrodes between the reservoir and the desired droplet.¹⁵⁵ These operations are shown in Figure 1.3g. While the throughput permitted by this approach may be smaller than the platform on which droplets move through channels by pressure, the electrode array scheme allows more flexible computer-programmable and reconfigurable droplet routing. The

electrowetting microfluidic devices have been used for colorimetric assays,¹⁵⁶ enzymatic assays,¹⁵⁷ immunoassays,¹⁵⁸ PCR,¹⁵⁹ and DNA sequencing.¹⁶⁰

1.4.5 Nanofluidics

The trend of miniaturization of flow systems presently involves many research efforts focused on the nanofluidics regime, which encompasses systems with at least one dimension below 100 nm. Nanofluidic structures have size scales comparable to the diameters of macromolecules and the thicknesses of the electric double layers at charged surfaces, resulting in unique molecular confinement and electrokinetic effects.

The most direct advantage gained by operating at the nanoscale is the ability to perform chemical and biochemical operations with liquid volumes that can be small enough to isolate individual molecules. Confining a polymer to a space narrower than the size of its coiled state leads to extension of the molecule. Such stretching of DNA has permitted analyses on single molecules including measuring length,¹⁶¹ detecting interactions with single proteins,¹⁶² and restriction mapping.¹⁶³ Base sequencing of individual DNA strands may soon be accomplished in nanofluidic devices.¹⁶⁴ Gaps smaller than molecular diameters can also enable separation of discrete numbers of molecules, either by steric exclusion of larger molecules¹⁶⁵ or by forcing molecules to adopt less entropically favorable conformations, for which the probability of occurrence depends on molecular size.¹⁶⁶

The high surface-area-to-volume ratio of nanoscale flow systems means that surface charges dominate transport and electrokinetic processes, a unique effect which can be harnessed for separations of small numbers of molecules based on charge instead of size. As

the channel diameter approaches the thickness of the layer of counterions screening the surface charges, molecules with the same charge as the surface are repelled to the center of the channel, and species of charge opposite to the surface are attracted to the channel wall.¹⁶⁷ Because the velocity profile through the counterion layer is parabolic, the species at the center of the channel flow faster than species at the wall. In very small channels, molecules with the same charge as the surface may be excluded from the channel entirely.¹⁶⁸ More sophisticated nanofluidic devices can actively direct separations by using electrodes rather than surface charge to control the electrical potential in the channel.¹⁶⁹

1.5 Colloidal Self-Assembly

1.5.1 Applications

Colloidal crystals are materials with micro- or nanometer periodic ordering. Features of sub-micrometer resolution can be fabricated by top-down methods including photolithography, soft lithography, and embossing¹⁷⁰⁻¹⁷¹ as described in the previous section for microfluidic devices. However, these techniques typically require multiple processing steps and expensive equipment. An elegant alternative is bottom-up self-assembly of colloidal particles. Micro- or nanoparticles spontaneously form repeating structures under the right balance of attractive and repulsive external and intermolecular forces, as shown in Figures 1.4a–c. The typical building blocks for colloidal crystals are metallic nanoparticles and polystyrene and silica microspheres. The resulting materials are being used in a variety of systems, demonstrating the versatility of the approach.

Colloidal crystals have received most attention because of their unique optical properties. It is often envisioned that colloidal crystals can serve as photonic band gap materials blocking penetration by light of certain wavelengths corresponding to crystal periodicity.¹⁷²⁻¹⁷⁴ By introducing designed defects into the crystals, integrated circuits for light waves instead of electrons may be created. These photonic circuits require formation of defect-free crystals which is practically difficult, so this application remains futuristic. However, colloidal crystal coatings for other optical applications may find more immediate use. Tunable diffraction gratings can be created by embedding a colloidal crystal in a polymer matrix that can swell and contract to adjust the spacing of the periodic ordering.¹⁷⁵ Colloidal crystals can also function as antireflective coatings.¹⁷⁶ When the periodicity of the crystal is smaller than the wavelength of light, the refractive index of the material may be taken as the average of the particles and the space between, enabling calibration of the refractive index on which the reflective characteristics of the material depend. These coatings have been shown to improve the efficiency of solar cells.¹⁷⁷

Colloidal crystals can also serve as templates for fabrication of other microstructures. To create surface patterns and textures, metal can be evaporated^{178,179} or the substrate can be etched^{178,180} in the spaces between the particles of a deposited colloidal monolayer, which can be subsequently removed. Figures 1.4d–e show a surface patterned with metal and an array of pillars, respectively, produced by such colloidal crystal lithography masks. Colloidal crystals can also serve as templates for more complex three-dimensional porous structures. In this case, the interstitial space between polymer spheres comprising a crystal is filled in with smaller silica¹⁸¹ or metallic¹⁸² nanoparticles which are annealed to form a continuous

network. Subsequent dissolution of the polymer spheres leaves a porous structure with periodic order, as shown in Figure 1.4f. The large surface area presented by such materials makes them useful as catalysts or sensors.¹⁸³ In particular, these materials have demonstrated promise as surface enhanced Raman spectroscopy substrates exhibiting enhanced and repeatable absorbance.^{184,185} Formation of a colloidal crystal at an emulsion droplet interface instead of on a solid substrate is a technique for creating shells that can encapsulate drugs or cells.¹⁸⁶

Colloidal crystals can function as chemical sensors if the constituent particles are functionalized with molecules or embedded in hydrogels that change size in the presence of specific chemicals. Variation in the interparticle spacing can change the electrical resistance of the crystal¹⁸⁷ or the color by changing the wavelength of light diffracted by the crystal.¹⁸⁸ Antibody-¹⁸⁹ or DNA-mediated¹⁹⁰ interactions that cause conductive particles to coagulate and close a circuit can provide a basis for biosensors that produce an electrical signal.

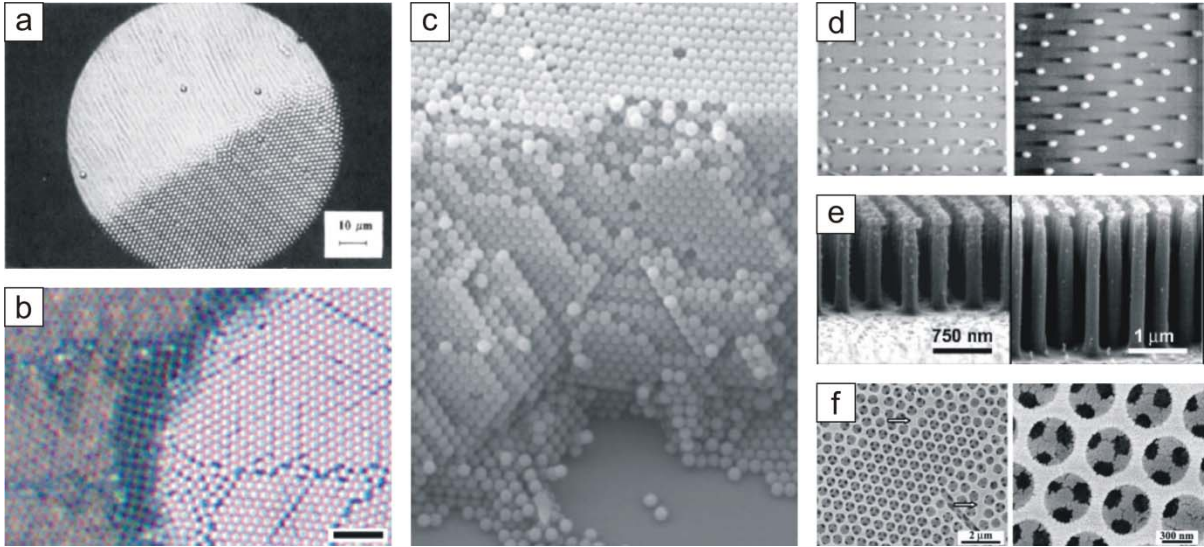


Figure 1.4. Images of colloidal assemblies, including (a) microspheres packing into a crystalline monolayer by convective assembly,²²⁰ (b) the transition from a bilayer to a monolayer of microspheres in a colloidal crystal coating,²²⁵ (c) a three-dimensional photonic crystal,²⁶⁰ (d) a metal pattern evaporated¹⁷⁹ and (e) microscale pillars etched¹⁸⁰ on surfaces using colloidal crystal lithography masks, and (f) a porous microstructure with periodic ordering templated by a colloidal crystal.²⁶¹

1.5.2 Assembly Driven by External Fields

In a gravitational field, colloidal particles that are sufficiently large eventually settle out of suspension. As they accumulate, the particles adopt a face-centered cubic¹⁹¹ or hexagonal close packed arrangement.¹⁹²⁻¹⁹³ Substrates with microscale holes^{194,195} or grooves¹⁹⁶ or patches patterned with charged molecules¹⁹⁷ can be used to control the locations of particles on the substrate and nucleate the growth of a single-domain colloidal crystal. Centrifugation may be used to accelerate the settling of the particles, but the time scale for the process remains hours.^{198,199}

Electrophoresis has been used to draw particles more rapidly to an electrode surface where they are packed into a crystalline structure.^{200,201} Electrohydrodynamic flows may

cause the particles at the surface to move laterally toward each other, enhancing the packing.²⁰² Patterns of crystals on surfaces can be created by illuminating a transparent indium tin oxide electrode with light in the desired crystal shape. The light increases the current density and, thus, the electrophoretic force in the illuminated areas.²⁰³ Similar to electrophoresis, a magnetic field may be used to drive assembly of crystals from magnetic particles.^{204,205}

Particles may be collected between planar electrodes by dielectrophoresis.²⁰⁶ This force acts on almost any type of particle, charged or uncharged, making dielectrophoretic assembly potentially widely applicable. The electric field induces dipoles in the particles because the polarizability of the counterionic layer around the particle surfaces is larger than the polarizability of the particles or the surrounding media. The dipoles induced by the electric field cause the particles to align in chains²⁰⁷ which can then pack into single-domain crystals.²⁰⁸ Dielectrophoresis has also been demonstrated to cause metallic nanoparticles to concentrate and aggregate linearly between the electrodes, forming a microwire and bridging the gap.^{209,210} Projection of an optical image onto a light sensitive electrode can create high resolution electric fields with individual regions of electric field intensity maxima to independently position thousands of particles in an array.²¹¹ Smaller numbers of individual particles may also be positioned by optical trapping in a laser beam.²¹²

1.5.3 Assembly Driven by Solvent Flow

Techniques relying on solvent flow to concentrate particles have also been demonstrated. Hard spheres²¹³ and diblock copolymer micelles²¹⁴ at high concentration may

organize into hexagonally close packed planes in shear flow so that the particles can move more easily past each other. Oscillatory shear flows may assist in the formation of single-domain crystals.²¹³ Shear-ordered colloidal crystal coatings can be deposited by spin coating.^{215,216}

Particles adsorbed to a liquid interface can be compressed into a two-dimensional ordered structure using a Langmuir trough.²¹⁷ The floating crystal layer formed by this method can be transferred to a solid substrate that is withdrawn from the liquid phase.^{218,219}

The most widely studied assembly technique based on flow is convective assembly. In this method, evaporation of the liquid medium from a suspension of particles engenders a flux in the liquid that transports the particles to the substrate-liquid-air contact line, as can be seen in the upper left of Figure 1.4a. There, attractive capillary forces may assist the accumulating particles in forming a close-packed array.²²⁰ The convective assembly mechanism is responsible for the ring of particles that forms as a sessile droplet of a suspension evaporates, the so-called “coffee ring effect.”²²¹ By vertically dipping a substrate into a dilute particle suspension and slowly withdrawing it^{222,223} or by immersing a substrate in a particle suspension and allowing the suspension medium to evaporate completely,²²⁴ a large uniform crystal coating can be deposited on the substrate by convective assembly. A more rapid and better controlled method of crystal coating deposition has been engineered by pinning a high volume fraction particle suspension in a wedge and dragging it across a horizontally oriented substrate, as illustrated in Figure 1.5.²²⁵ The structure of the coating can vary from submonolayer to a few complete layers, as shown in Figure 1.4b. The height of the coating increases as the withdrawal speed of the particle suspension decreases or the particle

concentration, evaporation rate, or drying length increase. The method is applicable to a variety of types of particles including polystyrene microspheres,²²⁵ metallic²²⁶ and inorganic²²⁷ nanoparticles, virus particles,²²⁸ and live cells.²²⁹

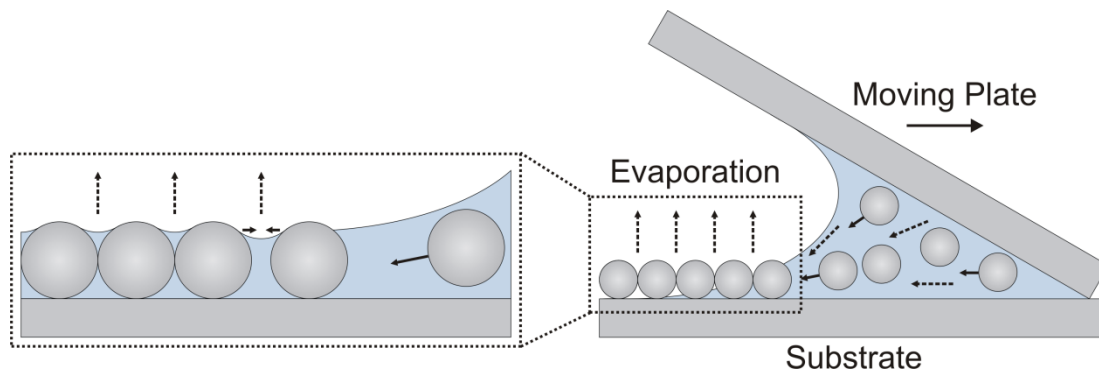


Figure 1.5. Schematic of convective assembly coating deposition process. A suspension of colloidal particles is pinned between two plates and dragged across the substrate. Evaporation from the thin film at the trailing meniscus of the suspension droplet drives particle transport to the growing crystal coating in the film. As particles accumulate in the film, they adopt a hexagonal close packed structure assisted by capillary forces.

1.5.4 Assembly Driven by Molecular Interactions

Molecular linkers can be used to bind particles to each other to create colloidal assemblies. This approach is generally applied to particles in the nanometer size range, where the ratio of surface-area-to-particle-mass is high. Synthetic polymers,²³⁰ complementary DNA strands,^{231,232} and antibody-antigen relationships²³³ have been used to bind particles together to form larger structures. Additional synthetic linkers which are sensitive to light,^{234,235} temperature^{236,237} solvent polarity,^{238,239} pH^{237,240,241} and electrochemical activity²⁴² have been used to assemble structures in response to environmental stimuli. Nanoparticles assembled by molecular interactions are typically organized into clusters

without crystalline ordering, a limitation to the technique. However, DNA linker molecules with precisely tuned sequence and length have been shown to lead to crystalline ordering.^{243,244} Linker molecules can be used to regulate the spacing between particles, providing a means to tune the optical properties.²⁴⁵

1.5.5 Assembly with Anisotropic Particles

A richer variety of microstructures can be assembled from anisotropic particles. For instance, assembly of particles having nonspherical geometries including ellipsoids,²⁴⁶ rods,^{247–249} viral rods,²²⁸ peanuts,²⁵⁰ and pentagon-shaped particles²⁵¹ can result in one-, two-, and three-dimensional structures that are not achievable with simple spherical particles alone. A multilayer assembly of rods is shown in Figure 1.6a. Electric²⁵² and magnetic²⁵³ fields can be used to align ellipsoidal particles in one direction during assembly, resulting in materials with directionally dependent properties. Material or chemical anisotropies may also be used to direct the way that particles align and organize. Spherical particles with a dielectric core and one side coated with a metallic²⁵⁴ or magnetic²⁵⁵ layer form chains as well as two- and three-dimensional structures with the coated sides of the particles facing each other when an electric or magnetic field is applied, as shown in Figure 1.6b. Particles with surface energy anisotropy can be oriented at a liquid interface.²⁵⁶ Selective chemical modification can define which regions of the particles are attractive to each other and thus control the arrangement of the final structure^{257,258} or the order of a multistep assembly.²⁵⁹ Figure 1.6c shows how cubic particles functionalized to have attractive interactions on only 4 sides assemble into sheets.

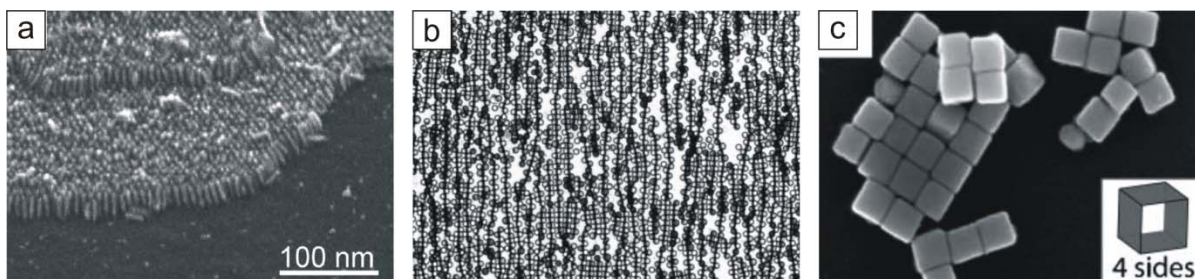


Figure 1.6. Images of colloidal assemblies from anisotropic particles, including (a) rod-shaped particles assembled into a colloidal crystal,²⁴⁹ (b) metallodielectric Janus particles that assemble in staggered chains with metal sides facing,²⁵⁴ and (c) cube-shaped particles that assemble into sheets because only 4 sides are functionalized to be attractive.²⁵⁸

1.6 Overview of Dissertation

Three new systems in which electric fields govern the shape of and flow in wetting films are described in the following chapters. In Chapter 2, an improved method of convective assembly of colloidal crystal coatings that incorporates electrowetting is discussed. Applying voltage during the coating deposition causes the film in which the particles assemble to be extended. The rate of assembly and homogeneity of the crystal are increased, and the process is explained using a model. Chapter 3 explains the behavior of wetting films between droplets and microfluidic device surfaces when electrowetting is used to move the droplets. While the motion of the droplets entrains liquid in the films, the electric field tends to thin the films. The effects of these competing forces are characterized on the basis of the applied voltage, ac frequency, and addition of surfactants to the system. Then, in Chapter 4, a nanoscale flow system based on electroosmosis in wetting films with thicknesses of tens of nanometers is described. The liquid flows over an open surface and is confined laterally by patterned hydrophobic monolayers, making the device simple to

construct relative to the more typical configuration of liquid enclosed in channels formed by lithography.

1.7 References

1. Reynolds, O. *Philos. T. R. Soc.* **1886**, 177, 157–234.
2. Grotberg, J. B. *Annu. Rev. Fluid Mech.* **1994**, 26, 529–571.
3. Sharma, A.; Ruckenstein, E. *J. Colloid Interf. Sci.* **1986**, 113, 456–479.
4. Ruschak, K. J. *Annu. Rev. Fluid Mech.* **1985**, 17, 65–89.
5. Evans, D. F.; Wennerström, H. *The Colloidal Domain: Where Physics, Chemistry, Biology, and Technology Meet, Second Ed.*; Wiley-VCH: New York, 1999.
6. Morgan, H.; Green, N. G. *AC Electrokinetics: Colloids and Nanoparticles*; Research Studies Press: Philadelphia, 2003.
7. Ruess, F. F. *Mem. Soc. Imperiale Naturalistes Moscow* **1809**, 2, 327–337.
8. Pohl, H. A. *J. Appl. Phys.* **1951**, 22, 869–871.
9. Ramos, A.; Morgan, H.; Green, N. G.; Castellanos, A. *J. Colloid Interf. Sci.* **1999**, 217, 420–422.
10. Mugele, F.; Baret, J.-C. *J. Phys.: Condens. Matter* **2005**, 17, R705–R774.
11. Stone, H. A.; Stroock, A. D.; Ajdari, A. *Annu. Rev. Fluid Mech.* **2004**, 36, 381–411.
12. Velev, O. D.; Bhatt, K. H. *Soft Matter* **2006**, 2, 738–750.
13. Israelachvili, J. N. *Intermolecular and Surface Forces, Second Ed.*; Academic Press: London, 1991.
14. Ohshima, H.; Healy, T. W.; White, L. R. *J. Colloid Interface Sci.* **1982**, 89, 484–493.
15. Devereux, O. F.; de Bruyn, P. L. *Interaction of Plane-Parallel Double Layers*; M.I.T. Press: Cambridge, 1963.
16. Taylor, G. I.; McEwan, A. D. *J. Fluid Mech.* **1965**, 22, 1–15.
17. Schäffer, E.; Thurn-Albrecht, T.; Russell, T. P.; Steiner, U. *Nature* **2000**, 403, 874–877.

18. Berge, B. *C. R. Acad. Sci. II* **1993**, *317*, 157–163.
19. Mugele, F.; Buehrle, J. *J. Phys.: Condens. Matter* **2007**, *19*, 375112.
20. Verheijen, H. J. J.; Prins, M. W. J. *Langmuir* **1999**, *15*, 6616–6620.
21. Vallet, M.; Vallade, M.; Berge, B. *Eur. Phys. J. B* **1999**, *11*, 583–591.
22. Shapiro, B.; Moon, H.; Garrell, R. L.; Kim, C.-J. *J. Appl. Phys.* **2003**, *93*, 5794–5811.
23. Seyrat, E.; Hayes, R. A. *J. Appl. Phys.* **2001**, *90*, 1383–1386.
24. Welters, W. J. J.; Fokkink, L. G. J. *Langmuir* **1998**, *14*, 1535–1538.
25. Kuo, J. S.; Spicar-Mihalic, P.; Rodriguez, I.; Chiu, D. T. *Langmuir*, **2003**, *19*, 250–255.
26. Moon, H.; Cho, S. K.; Garrell, R. L.; Kim, C.-J. *J. Appl. Phys.* **2002**, *92*, 4080–4087.
27. Chang, J.-H.; Choi, D. Y.; Han, S.; Pak, J. J. *Microfluid. Nanofluid.* **2010**, *8*, 269–273.
28. Berge, B.; Peseux, J. *Eur. Phys. J. E* **2000**, *3*, 159–163.
29. Kuiper, S.; Hendriks, B. H. W. *Appl. Phys. Lett.* **2004**, *85*, 1128–1130.
30. Hayes, R. A.; Feenstra, B. J. *Nature* **2003**, *425*, 383–385.
31. Hong, J. W.; Studer, V.; Hang, G.; Anderson, W. F.; Quake, S. R. *Nat. Biotechnol.* **2004**, *22*, 435–439.
32. Easley, C. J.; Karlinsey, J. M.; Bienvenue, J. M.; Legendre, L. A.; Roper, M. G.; Feldman, S. H.; Hughes, M. A.; Hewlett, E. L.; Merkel, T. J.; Ferrance, J. P.; Landers, J. P. *Nat. Acad. Sci. USA* **2006**, *103*, 19272–19277.
33. Woolley, A. T.; Hadley, D.; Landre, P.; deMello, A. J.; Mathies, R. A.; Northrup, M. A. *Anal. Chem.* **1996**, *68*, 4081–4086.
34. Burns, M. A.; Johnson, B. N.; Brahmasandra, S. N.; Handique, K.; Webster, J. R.; Krishnan, M.; Sammarco, T. S.; Man, P. M.; Jones, D.; Heldsinger, D.; Mastrangelo, C. H.; Burke, D. T. *Science* **1998**, *282*, 484–487.
35. Harrison, D. J.; Manz, A.; Fan, Z. Lüdi, H.; Widmer, H. M. *Anal. Chem.* **1992**, *64*, 1926–1932.
36. Raymond, D. E.; Manz, A.; Widmer, H. M. *Anal. Chem.* **1994**, *66*, 2858–2865.

37. Duke, T. A. J.; Austin, R. H. *Phys. Rev. Lett.* **1998**, *80*, 1552–1555.
38. Cabodi, M.; Turner, S. W. P.; Craighead, H. G. *Anal. Chem.* **2002**, *74*, 5169–5174.
39. Chang, S.; Cho, Y.-H. *Lab Chip* **2008**, *8*, 1930–1936.
40. Cheng, J.; Sheldon, E. L.; Wu, L.; Uribe, A.; Gerrue, L. O.; Carrino, J.; Heller, M. J.; O’Connell, J. P. *Nat. Biotechnol.* **1998**, *16*, 541–546.
41. Morgan, H.; Hughes, M. P.; Green, N. G. *Biophys. J.* **1999**, *77*, 516–525.
42. Wang, M. M.; Tu, E.; Raymond, D. E.; Yang, J. M.; Zhang, H.; Hagen, N.; Dees, B.; Mercer, E. M.; Forster, A. H.; Kariv, I.; Marchand, P. J.; Butler, W. F. *Nat. Biotechnol.* **2005**, *23*, 83–87.
43. Kim, U.; Shu, C.-W.; Dane, K. Y.; Daugherty, P. S.; Wang, J. Y. J.; Soh, H. T. *P. Nat. Acad. Sci. USA* **2007**, *104*, 20708–20712.
44. Wang, L.; Lu, J.; Marchenko, S. A.; Monuki, E. S.; Flanagan, L. A.; Lee, A. P. *Electrophoresis* **2009**, *30*, 782–791.
45. Fu, A. Y.; Chou, H.-P.; Spence, C.; Arnold, F. H.; Quake, S. R. *Anal. Chem.* **2002**, *74*, 2451–2457.
46. Woolley, A. T.; Lao, K.; Glazer, A. N.; Mathies, R. A. *Anal. Chem.* **1998**, *70*, 684–688.
47. Lai, S.; Wang, S.; Luo, J.; Lee, L. J.; Yang, S.-T.; Madou, M. J. *Anal. Chem.* **2004**, *76*, 1832–1837.
48. Liu, R. H.; Yang, J.; Lenigk, R.; Bonanno, J.; Grodzinski, P. *Anal. Chem.* **2004**, *76*, 1824–1831.
49. Sahoo, H. R.; Kralj, J. G.; Jensen, K. F. *Angew. Chem. Int. Ed.* **2007**, *46*, 5704–5708.
50. Edel, J. B.; Fortt, R.; deMello, J. C.; deMello, A. J. *Chem. Commun.* **2002**, 1136–1137.
51. Chan, E. M.; Mathies, R. A.; Alivisatos, A. P. *Nano Lett.* **2003**, *3*, 199–201.
52. Wagner, J.; Köhler, J. M. *Nano Lett.* **2005**, *5*, 685–691.
53. Khan, S. A.; Günther, A.; Schmidt, M. A.; Jensen, K. F. *Langmuir* **2004**, *20*, 8604–8611.

54. Xu, S.; Nie, Z.; Seo, M.; Lewis, P.; Kumacheva, E.; Stone, H. A.; Garstecki, P.; Weibel, D. B.; Gitlin, I.; Whitesides, G. M. *Angew. Chem. Int. Ed.* **2005**, *44*, 724–728.
55. Millman, J. R.; Bhatt, K. H.; Prevo, B. G.; Velev, O. D. *Nat. Mater.* **2005**, *4*, 98–102.
56. Zhang, H.; Tumarkin, E.; Peerani, R.; Nie, Z.; Sullan, R. M. A.; Walker, C. W.; Kumacheva, E. *J. Am. Chem. Soc.* **2006**, *128*, 12205–12210.
57. De Geest, B. G.; Urbanski, J. P.; Thorsen, T.; Demeester, J.; De Smedt, S. C. *Langmuir* **2005**, *21*, 10275–10279.
58. Dendukuri, D.; Tsoi, K.; Hatton, A.; Doyle, P. S. *Langmuir* **2005**, *21*, 2113–2116.
59. Dendukuri, D.; Pregibon, D. C.; Collins, J.; Hatton, T. A.; Doyle, P. S. *Nat. Mater.* **2006**, *5*, 365–369.
60. Pregibon, D. C.; Toner, M.; Doyle, P. S. *Science* **2007**, *315*, 1393–1396.
61. Nie, Z.; Seo, M.; Xu, S.; Kumacheva, E. *J. Am. Chem. Soc.* **2006**, *128*, 9408–9412.
62. Nisisako, T.; Torii, T.; Takahashi, T.; Takizawa, Y. *Adv. Mater.* **2006**, *18*, 1152–1156.
63. Dendukuri, D.; Hatton, T. A.; Doyle, P. S. *Langmuir* **2007**, *23*, 4669–4674.
64. Okushima, S.; Nisisako, T.; Torii, T.; Higuchi, T. *Langmuir* **2004**, *20*, 9905–9908.
65. Utada, A. S.; Lorenceau, E.; Link, D. R.; Kaplan, P. D.; Stone, H. A.; Weitz, D. A. *Science* **2005**, *308*, 537–541.
66. Nie, Z.; Xu, S.; Seo, M.; Lewis, P. C.; Kumacheva, E. *J. Am. Chem. Soc.* **2005**, *127*, 8058–8063.
67. Lorenceau, E.; Utada, A. S.; Link, D. R.; Galder, C.; Joanicot, M.; Weitz, D. A. *Langmuir* **2005**, *21*, 9183–9186.
68. Tan, Y.-C.; Hettiarachchi, K.; Siu, M.; Pan, Y.-R.; Lee, A. P. *J. Am. Chem. Soc.* **2006**, *128*, 5656–5658.
69. Chen, C.-H.; Abate, A. R.; Lee, D.; Terentjev, E. M.; Weitz, D. A. *Adv. Mater.* **2009**, *21*, 3201–3204.
70. Tuckerman, D. B.; Pease, R. F. W. *IEEE Electr. Dev. L.* **1981**, *2*, 126–129.

71. Linan, J.; Mikkelsen, J.; Koo, J.-M.; Huber, D.; Yao, S.; Zhang, L.; Zhou, P.; Maveety, J. G.; Prasher, R.; Santiago, J. G.; Kenny, T. W.; Goodson, K. E. *IEEE T. Compon. Pack. T.* **2002**, *25*, 347–355.
72. Paik, P. Y.; Pamula, V. K.; Chakrabarty, K. *IEEE T. VLSI Syst.* **2008**, *16*, 432–443.
73. Uçar, A. B.; Velev, O. D. *Soft Matter* **2012**, *8*, 11232–11235.
74. Choi, N. W.; Cabodi, M.; Held, B.; Gleghorn, J. P.; Bonassar, L. J.; Stroock, A. D. *Nat. Mater.* **2007**, *6*, 908–915.
75. Chang, S. T.; Uçar, A. B.; Swindlehurst, G. R.; Bradley, R. O.; Renk, F. J.; Velev, O. D. *Adv. Mater.* **2009**, *21*, 2803–2807.
76. Erickson, D.; Rockwood, T.; Emery, T.; Scherer, A.; Psaltis, D. *Opt. Lett.* **2006**, *31*, 59–61.
77. Groisman, A.; Enzelberger, M.; Quake, S. R. *Science* **2003**, *300*, 955–958.
78. Prakash, M.; Gershenfeld, N. *Science* **2007**, *315*, 832–835.
79. Brody, J. P.; Yager, P. *Sensor. Actuat. A* **1997**, *58*, 13–18.
80. Yamada, M.; Nakashima, M.; Seki, M. *Anal. Chem.* **2004**, *76*, 5465–5471.
81. MacDonald, M. P.; Spalding, G. C.; Dholakia, K. *Nature* **2003**, *426*, 421–424.
82. Pamme, N.; Manz, A. *Anal. Chem.* **2004**, *76*, 7250–7256.
83. Laurell, T.; Petersson, F.; Nilsson, A. *Chem. Soc. Rev.* **2007**, *36*, 492–506.
84. Kamholz, A. E.; Weigl, B. H.; Finlayson, B. A.; Yager, P. *Anal. Chem.* **1999**, *71*, 5340–5347.
85. Takayama, S.; Ostuni, E.; LeDuc, P.; Naruse, K.; Ingber, D. E.; Whitesides, G. M. *Nature* **2001**, *411*, 1016.
86. Takayama, S.; McDonald, J. C.; Ostuni, E.; Liang, M. N.; Kenis, P. J. A.; Ismagilov, R. F.; Whitesides, G. M. *P. Nat. Acad. Sci. USA* **1999**, *96*, 5545–5548.
87. Kenis, P. J. A.; Ismagilov, R. F.; Whitesides, G. M. *Science* **1999**, *285*, 83–85.
88. Chou, H.-P.; Unger, M. A.; Quake, S. R. *Biomed. Microdevices* **2001**, *3*, 323–330.
89. Liu, R. H.; Stremler, M. A.; Sharp, K. V.; Olsen, M. G.; Santiago, J. G.; Adrian, R. J.; Aref, H.; Beebe, D. J. *J. Microelectromech. S.* **2000**, *9*, 190–197.

90. Stroock, A. D.; Dertinger, S. K. W.; Ajdari, A.; Mezić, I.; Stone, H. A.; Whitesides, G. M. *Science* **2002**, *295*, 647–651.
91. Johnson, T. J.; Ross, D.; Locascio, L. E. *Anal. Chem.* **2002**, *74*, 45–51.
92. Paik, P.; Pamula, V. K.; Fair, R. B. *Lab Chip* **2003**, *3*, 253–259.
93. Song, H.; Bringer, M. R.; Tice, J. D.; Gerdtts, C. J.; Ismagilov, R. F. *Appl. Phys. Lett.* **2003**, *83*, 4664–4666.
94. Gunther, A.; Khan, S. A.; Thalmann, M.; Trachsel, F.; Jensen, K. F. *Lab Chip* **2004**, *4*, 278–286.
95. Yang, Z.; Matsumoto, S.; Goto, H.; Matsumoto, M.; Maeda, R. *Sens. Actuat. A* **2001**, *93*, 266–272.
96. Oddy, M. H.; Santiago, J. G.; Mikkelsen, J. C. *Anal. Chem.* **2001**, *73*, 5822–5832.
97. Bazant, M. Z.; Squires, T. M. *Phys. Rev. Lett.* **2004**, *92*, 066101.
98. Chang, S. T.; Beaumont, E.; Petsev, D. N.; Velev, O. D. *Lab Chip* **2008**, *8*, 117–124.
99. Bau H. H.; Zhong, J.; Yi, M. *Sens. Actuat. B* **2001**, *79*, 207–215.
100. Gau, H.; Herminghaus, S.; Lenz, P.; Lipowsky, R. *Science* **1999**, *283*, 46–49.
101. Kataoka, D. E.; Troian, S. M. *Nature* **1999**, *402*, 794–797.
102. Zhao, B.; Moore, J. S.; Beebe, D. J. *Science* **2001**, *291*, 1023–1026.
103. Chaudury, M. K.; Whitesides, G. M. *Science* **1992**, *256*, 1539–1541.
104. Burns, M. A.; Mastrangelo, C. H.; Sammarco, T. S.; Man, F. P.; Webster, J. R.; Johnson, B. N.; Foerster, B.; Jones, D.; Fields, Y.; Kaiser, A. R.; Burke, D. T. *P. Nat. Acad. Sci. USA* **1996**, *93*, 5556–5561.
105. Pollack, M. G.; Fair, R. B.; Shenderov, A. D. *Appl. Phys. Lett.* **2000**, *77*, 1725–1726.
106. Gallardo, B. S.; Gupta, V. K.; Eagerton, F. D.; Jong, L. I.; Craig, V. S.; Shah, R. R.; Abbott, N. L. *Science* **1999**, *283*, 57–60.
107. Ichimura, K.; Oh, S.-K.; Nakagawa, M. *Science* **2000**, *288*, 1624–1626.
108. Juncker, D.; Schmid, H.; Drechsler, U.; Wolf, H.; Michel, B.; de Rooij, N.; Delamarche, E. *Anal. Chem.* **2002**, *74*, 6139–6144.

109. Reccius, C. H.; Mannion, J. T.; Cross, J. D.; Craighead, H. G. *Phys. Rev. Lett.* **2005**, *95*, 268101.
110. O'Brien, M. J.; Bisong, P.; Ista, L. K.; Rabinovich, E. M.; Garcia, A. L.; Sibbett, S. S.; Lopez, G. P.; Brueck, S. R. J. *J. Vac. Sci. Technol., B* **2003**, *21*, 2941–2945.
111. Campbell, L. C.; Wilkinson, M. J.; Manz, A.; Camilleri, P.; Humphreys, C. J. *Lab Chip* **2004**, *4*, 225–229.
112. Mullenborn, M.; Dirac, H.; Petersen, J. W. *Appl. Surf. Sci.* **1995**, *86*, 568–576.
113. Delamarche, E.; Bernard, A.; Schmid, H.; Michel, B.; Biebuyck, H. *Science* **1997**, *276*, 779–781.
114. Effenhauser, C. S.; Bruin, G. J. M.; Paulus, A.; Ehrat, M. *Anal. Chem.* **1997**, *69*, 3451–3457.
115. Becker, H.; Heim, U. *Sens. Actuat. A* **2000**, *83*, 130–135.
116. Chou, S. Y.; Krauss, P. R.; Renstrom, P. J. *Science* **1996**, *272*, 85–87.
117. Colburn, M.; Johnson, S.; Stewart, M.; Damle, S.; Bailey, T.; Choi, B.; Wedlake, M.; Michaelson, T.; Sreenivasan, S. V.; Ekerdt, J.; Willson, C. G. *Proc. Soc. Photo-Opt. Instrum. Eng.* **1999**, *3676*, 379–389.
118. Cao, H.; Yu, Z.; Wang, J.; Tegenfeldt, J. O.; Austin, R. H.; Chen, E.; Wu, W.; Chou, S. Y. *Appl. Phys. Lett.* **2002**, *81*, 174–176.
119. McCormick, R. M.; Nelson, R. J.; Alonso-Amigo, M. G.; Benvegnu, D. J.; Hooper, H. H. *Anal. Chem.* **1997**, *69*, 2626–2630.
120. Becker, H.; Gartner, C. *Anal. Bioanal. Chem.* **2008**, *390*, 89–111.
121. Patrio, N.; McCague, C.; Norton, P. R.; Petersen, N. O. *Langmuir* **2007**, *23*, 715–719.
122. Qin, M.; Wang, L.-K.; Feng, X.-Z. *Langmuir* **2007**, *23*, 4465–4471.
123. Soper, S. A.; Henry, A. C.; Vaidya, B.; Galloway, M.; Wabuyele, M.; McCarley, R. L. *Anal. Chim. Acta* **2002**, *470*, 87–99.
124. Bi, H.; Meng, S.; Li, Y.; Guo, K.; Chen, Y.; Kong, J.; Yang, P.; Zhong, W.; Liu, B. *Lab Chip* **2006**, *6*, 769–775.
125. Chaudhury, M. K.; Whitesides, G. M. *Science*, **1992**, *255*, 1230–1232.

126. Ocvirk, G.; Munroe, M.; Tang, T.; Oleschuk, R.; Westra, K.; Harrison, D. J. *Electrophoresis*, **2000**, *21*, 107–115.
127. Roman, G. T.; Hlaus, T.; Bass, K. J.; Seelhammer, T. G.; Culbertson, C. T. *Anal. Chem.* **2005**, *77*, 1414–1422.
128. Ren, X.; Bachman, M.; Sims, C.; Li, G. P.; Allbritton, N. J. *J. Chromatogr. B* **2001**, *762*, 117–125.
129. Efimenko, K.; Wallace, W. E.; Genzer, J. J. *J. Coll. Interf. Sci.* **2002**, *254*, 306–315.
130. Garcia, C. D.; Dressen, B. M.; Henderson, A.; Henry, C. S. *Electrophoresis* **2005**, *26*, 703–709.
131. Liu, B.-F.; Ozaki, M.; Hisamoto, H.; Luo, Q.; Utsumi, Y.; Hattori, T.; Terabe, S. *Anal. Chem.* **2005**, *77*, 573–578,
132. Huang, B.; Wu, H.; Kim, S.; Zare, R. N. *Lab Chip* **2005**, *5*, 1005–1007.
133. Chen, H.-Y.; Elkasabi, Y.; Lahann, J. *J. Am. Chem. Soc.* **2006**, *128*, 374–380.
134. Wang, A.-J.; Xu, J.-J.; Chen, H.-Y. *J. Chromatogr. A* **2006**, *1107*, 257–264.
135. Madou, M. J.; Kellogg, G. J. *Proc. Soc. Photo-Opt. Instrum. Eng.* **1998**, *3259*, 80–93.
136. Penrose, A.; Myers, P.; Bartle, K.; McCrossen, S. *Analyst* **2004**, *129*, 704–709.
137. Haerberle, S.; Brenner, T.; Zengerle, R.; Ducleé, J. *Lab Chip* **2006**, *6*, 776–781.
138. Steigert, J.; Grumann, M.; Brenner, T.; Riegger, L.; Harter, J.; Zengerle, R.; Ducleé, J. *Lab Chip* **2006**, *6*, 1040–1044.
139. Cho, Y.-K.; Lee, J.-G.; Park, J.-M.; Lee, B.-S.; Lee, Y.; Ko, C. *Lab Chip* **2007**, *7*, 565–573.
140. Unger, M. A.; Chou, H.-P.; Thorsen, T.; Scherer, A.; Quake, S. R. *Science* **2000**, *288*, 113–116.
141. Thorsen, T.; Maerkl, S. J.; Quake, S. R. *Science* **2002**, *198*, 580–584.
142. Hansen, C. L.; Skordalakes, E.; Berger, J. M.; Quake S. R. *P. Nat. Acad. Sci. USA* **2002**, *99*, 16531–16536.
143. Gómez-Sjöberg, R.; Leyrat, A. A.; Pirone, D. M.; Chen, C. S.; Quake, S. R. *Anal. Chem.* **2007**, *79*, 8557–8563.

144. Cai, L.; Friedman, N.; Xie, X. S. *Nature* **2006**, *440*, 358–362.
145. Lee, C.-C.; Sui, G.; Elizarov, A.; Shu, C. J.; Shin, Y.-S.; Dooley, A. N.; Huang, J.; Daridon, A.; Wyatt, P.; Stout, D.; Kolb, H. C.; Witte, O. N.; Satyamurthy, N.; Heath, J. R.; Phelps, M. E.; Quake, S. R.; Tseng, H.-R. *Science* **2005**, *310*, 1793.
146. Thorsen, T.; Roberts, R. W.; Arnold, F. H.; Quake, S. R. *Phys. Rev. Lett.* **2001**, *86*, 4163–4166.
147. Anna, S. L.; Bontoux, N.; Stone, H. A. *Appl. Phys. Lett.* **2003**, *82*, 364–366.
148. Song, H.; Tice, J. D.; Ismagilov, R. F. *Angew. Chem. Int. Ed.* **2003**, *42*, 767–772.
149. Link, D. R.; Anna, S. L.; Weitz, D. A.; Stone, H. A. *Phys. Rev. Lett.* **2004**, *92*, 054503.
150. Ahn, K.; Kerbage, C.; Hunt, T. P.; Westervelt, R. M.; Link, D. R.; Weitz, D. A. *Appl. Phys. Lett.* **2006**, *88*, 024104.
151. Song, H.; Ismagilov, R. F. *J. Am. Chem. Soc.* **2003**, *125*, 14613–14619.
152. Zheng, B.; Roach, L. R.; Ismagilov, R. F. *J. Am. Chem. Soc.* **2003**, *125*, 11170–11171.
153. Martin, K.; Henkel, T.; Baier, V.; Grodrian, A.; Schön, T.; Roth, M.; Köhler, J. M.; Metze, J. *Lab Chip* **2003**, *3*, 202–207.
154. Boedicker, J. Q.; Li, L.; Kline, T. R.; Ismagilov, R. F. *Lab Chip* **2008**, *8*, 1265–1272.
155. Pollack, M. G.; Shenderov, A. D.; Fair, R. B. *Lab Chip* **2002**, *2*, 96–101.
156. Srinivasan, V.; Pamula, V. K.; Fair, R. B. *Anal. Chim. Acta* **2004**, *507*, 145–150.
157. Sista, R. S.; Eckhardt, A. E.; Wang, T.; Graham, C.; Rouse, J. L.; Norton, S. M.; Srinivasan, V.; Pollack, M. G.; Tolun, A. A.; Bali, D.; Millington, D. S.; Pamula, V. K. *Clin. Chem.* **2011**, *57*, 1444–1451.
158. Sista, R. S.; Eckhardt, A. E.; Srinivasan, V.; Pollack, M. G.; Palanki, S.; Pamula, V. K. *Lab Chip* **2008**, *8*, 2188–2196.
159. Hua, Z.; Rouse, J. L.; Eckhardt, A. E.; Srinivasan, V.; Pamula, V. K.; Schell, W. A.; Benton, J. L.; Mitchell, T. G.; Pollack, M. G. *Anal. Chem.* **2010**, *82*, 2310–2316.
160. Boles, D. J.; Benton, J. L.; Siew, G. J.; Levy, M. H.; Thwar, P. K.; Sandahl, M. A.; Rouse, J. L.; Perkins, L. C.; Sudarsan, A. P.; Jalili, R.; Pamula, V. K.; Srinivasan, V.;

- Fair, R. B.; Griffin, P. B.; Eckhardt, A. E.; Pollack, M. G. *Anal. Chem.* **2011**, *83*, 8439–8447.
161. Tegenfeldt, J. O.; Prinz, C.; Cao, H.; Chou, S.; Reisner, W. W.; Riehn, R.; Wang, Y. M.; Cox, E. C.; Sturm, J. C.; Silberzan, P.; Austin, R. H. *P. Nat. Acad. Sci. USA* **2004**, *101*, 10979–10983.
162. Wang, Y. M.; Tegenfeldt, J. O.; Reisner, W.; Riehn, R.; Guan, X.-J.; Guo, L.; Golding, I.; Cox, E. C.; Sturm, J.; Austin, R. H. *P. Nat. Acad. Sci. USA* **2005**, *102*, 9796–9801.
163. Riehn, R.; Lu, M.; Wang, Y.-M.; Lim, S. F.; Cox, E. C.; Austin, R. H. *P. Nat. Acad. Sci. USA* **2005**, *102*, 10012–10016.
164. Lagerqvist, J.; Zwolak, M.; Di Ventra, M. *Nano Lett.* **2006**, *6*, 779–782.
165. Fu, J.; Schoch, R. B.; Stevens, A. L.; Tannenbaum, S. R.; Han, J. *Nat. Nanotechnol.* **2007**, *2*, 121–128.
166. Han, J.; Turner, S. W.; Craighead, H. G. *Phys. Rev. Lett.* **1999**, *83*, 1688–1691.
167. Garcia, A. L.; Ista, L. K.; Petsev, D. N.; O’Brien, M. J.; Bisong, P.; Mammoli, A. A.; Brueck, S. R. J.; López, G. P. *Lab Chip* **2005**, *5*, 1271–1276.
168. Schoch, R. B.; Bertsch, A.; Renaud, P. *Nano Lett.* **2006**, *6*, 543–547.
169. Karnik, R.; Castelino, K.; Majumdar, A. *Appl. Phys. Lett.* **2006**, *88*, 123114.
170. Gates, B. D.; Xu, Q.; Stewart, M.; Ryan, D.; Willson, C. G.; Whitesides, G. M. *Chem. Rev.* **2005**, *105*, 1171–1196.
171. Xia, Y.; Whitesides, G. M. *Annu. Rev. Mater. Sci.* **1998**, *28*, 153–184.
172. Flaugh, P. L.; O’Donnell, S. E.; Asher, S. A. *Appl. Spectrosc.* **1984**, *38*, 847–850.
173. Tarhan, İ. İ.; Watson, G. H. *Phys. Rev. Lett.* **1996**, *76*, 315–318.
174. Joannopoulos, J. D.; Villeneuve, P. R.; Fan, S. *Nature* **1997**, *386*, 143–149.
175. Weissman, J. M.; Sunkara, H. B.; Tse, A. S.; Asher, S. A. *Science* **1996**, *274*, 959–960.
176. Prevo, B. G.; Hwang, Y.; Velev, O. D. *Chem. Mater.* **2005**, *17*, 3642–3651.
177. Prevo, B. G.; Hon, E. W.; Velev, O. D. *J. Mater. Chem.* **2007**, *17*, 791–799.

178. Deckman, H. W.; Dunsmuir, J. H. *Appl. Phys. Lett.* **1982**, *41*, 377–379.
179. Hulteen, J. C.; Van Duyne, R. P. *J. Vac. Sci. Technol. A* **1995**, *13*, 1553–1558.
180. Cheung, C. L.; Nikolić, R. J.; Reinhardt, C. E.; Wang, T. F. *Nanotechnology* **2006**, *17*, 1339–1343.
181. Velev, O. D.; Jede, T. A.; Lobo, R. F.; Lenhoff, A. M. *Nature* **1997**, *389*, 447–448.
182. Velev, O. D.; Tessier, P. M.; Lenhoff, A. M.; Kaler, E. W. *Nature* **1999**, *401*, 548.
183. Song, Y.-Y.; Zhang, D.; Gao, W.; Xia, X.-H. *Chem. Eur. J.* **2005**, *11*, 2177–2182.
184. Freeman, R. G.; Grabar, K. C.; Allison, K. J.; Bright, R. M.; Davis, J. A.; Guthrie, A. P.; Hommer, M. B.; Jackson, M. A.; Smith, P. C.; Walter, D. G.; Natan, M. J. *Science* **1995**, *267*, 1629–1632.
185. Kuncicky, D. M.; Christesen, S. D.; Velev, O. D. *Appl. Spectrosc.* **2005**, *59*, 401–409.
186. Dinsmore, A. D.; Hsu, M. F.; Nikolaides, M. G.; Marquez, M.; Bausch, A. R.; Weitz, D. A. *Science* **2002**, *298*, 1006–1009.
187. Wang, L.; Shi, X.; Kariuki, N. N.; Schadt, M.; Wang, G. R.; Rendeng, Q.; Choi, J.; Luo, J.; Lu, S.; Zhong, C.-J. *J. Am. Chem. Soc.* **2007**, *129*, 2161–2170.
188. Holtz, J. H.; Asher, S. A. *Nature* **1997**, *389*, 829–832.
189. Velev, O. D.; Kaler, E. W. *Langmuir* **1999**, *15*, 3693–3698.
190. Park, S.-J.; Taton, T. A.; Mirkin, C. A. *Science* **2002**, *295*, 1503–1506.
191. Míguez, H.; Meseguer, F.; López, C.; Mifsud, A.; Moya, J. S.; Vázquez, L. *Langmuir* **1997**, *13*, 6009–6011.
192. Davis, K. E.; Russel, W. B.; Glantschnig, W. J. *Science* **1989**, *245*, 507–510.
193. Zhu, J.; Li, M.; Rogers, R.; Meyer, W.; Ottewill, R. H.; STS-73 Space Shuttle Crew; Russel, W. B.; Chaikin, P. M. *Nature* **1997**, *387*, 883–885.
194. van Blaaderen, A.; Ruel, R.; Wilzlus, P. *Nature* **1997**, *385*, 321–324.
195. Yin, Y.; Lu, Y.; Gates, B.; Xia, Y. *J. Am. Chem. Soc.* **2001**, *123*, 8718–8729.
196. Lin, K.; Crocker, J. C.; Prasad, V.; Schofield, A.; Weitz, D. A.; Lubensky, T. C.; Yodh, A. G. *Phys. Rev. Lett.* **2000**, *85*, 1770–1773.

197. Zheng, H.; Rubner, M. F.; Hammond, P. T. *Langmuir* **2002**, *18*, 4505–4510.
198. Wijnhoven, J. E. G. J.; Vos, W. L. *Science* **1998**, *281*, 802–804.
199. Holland, B. T.; Blanford, C. F.; Do, T.; Stein, A. *Chem. Mater.* **1999**, *11*, 795–805.
200. Giersig, M.; Mulvaney, P. *Langmuir* **1993**, *9*, 3408–3413.
201. Holgado, M.; García-Santamaría, F.; Blanco, A.; Ibisate, M.; Cintas, A.; Míguez, H.; Serna, C. J.; Molpeceres, C.; Requena, J.; Mifsud, A.; Meseguer, F.; López, C. *Langmuir* **1999**, *15*, 4701–4704.
202. Trau, M.; Saville, D. A.; Aksa, I. A. *Science* **1996**, *272*, 706–709.
203. Hayward, R. C.; Saville, D. A.; Aksay, I. A. *Nature* **2000**, *404*, 56–59.
204. Dimitrov, A. S.; Takahashi, T.; Furusawa, K.; Nagayama, K. *J. Phys. Chem.* **1996**, *100*, 3163–3168.
205. Butter, K.; Bomans, P. H. H.; Frederik, P. M.; Vroege, G. J.; Philipse, A. P. *Nat. Mater.* **2003**, *2*, 88–91.
206. Pethig, R.; Huang, Y.; Wang, X.-B.; Burt, J. P. H. *J. Phys. D: Appl. Phys.* **1992**, *24*, 881–888.
207. Fraden, S.; Hurd, A. J.; Meyer, R. B. *Phys. Rev. Lett.* **1989**, *63*, 2373–2376.
208. Lumsdon, S. O.; Kaler, E. W.; Williams, J. P.; Velev, O. D. *Appl. Phys. Lett.* **2003**, *82*, 949–951.
209. Hermanson, K. D.; Lumsdon, S. O.; Williams, J. P.; Kaler, E. W.; Velev, O. D. *Science* **2001**, *294*, 1082–1086.
210. Bhatt, K. H.; Velev, O. D. *Langmuir* **2004**, *20*, 467–476.
211. Chiou, P. Y.; Ohta, A. T.; Wu, M. C. *Nature* **2005**, *436*, 370–372.
212. Misawa, H.; Sasaki, K.; Koshioka, M.; Kitamura, N.; Masuhara, H. *Appl. Phys. Lett.* **1992**, *60*, 310–312.
213. Ackerson, B. J. *J. Rheol.* **1990**, *34*, 553–590.
214. McConnell, G. A.; Lin, M. Y.; Gast, A. P. *Macromolecules*, **1995**, *28*, 6754–6764.
215. Jiang, P.; McFarland, M. J. *J. Am. Chem. Soc.* **2004**, *126*, 13778–13786.

216. Mihi, A.; Ocaña, M.; Míguez, H. *Adv. Mater.* **2006**, *18*, 2244–2249.
217. Aveyard, R.; Clint, J. H.; Nees, D.; Paunov, V. N. *Langmuir* **2000**, *16*, 1969–1979.
218. Szekeres, M.; Kamalin, O.; Grobet, P. G.; Schoonheydt, R. A.; Wostyn, K.; Clays, K.; Persoons, A.; Dékány, I. *Colloid. Surface. A* **2003**, *227*, 77–83.
219. Tao, A. R.; Huang, J.; Yang, P. *Accounts Chem. Res.* **2008**, *41*, 1662–1673.
220. Denkov, N. D.; Velev, O. D.; Kralchevsky, P. A.; Ivanov, I. B.; Yoshimura, H.; Nagayama, K. *Langmuir* **1992**, *8*, 3183–3190.
221. Deegan, R. D.; Bakajin, O.; Dupont, T. F.; Huber, G.; Nagel, S. R.; Witten, T. A. *Nature* **1997**, *389*, 827–829.
222. Dimitrov, A. S.; Nagayama, K. *Langmuir* **1996**, *12*, 1303–1311.
223. Gu, Z.-Z.; Fujishima, A.; Sato, O. *Chem. Mater.* **2002**, *14*, 760–765.
224. Jiang, P.; Bertone, J. F.; Hwang, K. S.; Colvin, V. L. *Chem. Mater.* **1999**, *11*, 2132–2140.
225. Prevo, B. G.; Velev, O. D. *Langmuir* **2004**, *20*, 2099–2107.
226. Prevo, B. G.; Fuller, J. C.; Velev, O. D. *Chem. Mater.* **2005**, *17*, 28–35.
227. Finkel, N. H.; Prevo, B. G.; Velev, O. D.; He, L. *Anal. Chem.* **2005**, *77*, 1088–1095.
228. Kuncicky, D. M.; Naik, R. R.; Velev, O. D. *Small* **2006**, *2*, 1462–1466.
229. Jerrim, L. B.; Velev, O. D. *Langmuir* **2009**, *25*, 5692–5702.
230. Boal, A. K.; Ilhan, F.; DeRouchey, J. E.; Thurn-Albrecht, T.; Russell, T. P.; Rotello, V. M. *Nature* **2000**, *404*, 746–748.
231. Mirkin, C. A.; Letsinger, R. L.; Mucic, R. C.; Storhoff, J. J. *Nature* **1996**, *382*, 607–609.
232. Alivisatos, A. P.; Johnsson, K. P.; Peng, X.; Wilson, T. E.; Loweth, C. J.; Bruchez, M. P.; Schultz, P. G. *Nature*, **1996**, *382*, 609–611.
233. Shenton, W.; Davis, S. A.; Mann, S. *Adv. Mater.* **1999**, *11*, 449–452.
234. Ipe, B. I.; Mahima, S.; Thomas, K. G. *J. Am. Chem. Soc.* **2003**, *125*, 7174–7175.

235. Plunkett, K. N.; Mohraz, A.; Haasch, R. T.; Lewis, J. A.; Moore, J. S. *J. Am. Chem. Soc.* **2005**, *127*, 14574–14575.
236. Naka, K.; Itoh, H.; Chujo, Y. *Langmuir* **2003**, *19*, 5496–5501.
237. Isojima, T.; Lattuada, M.; Vander Sande, J. B.; Hatton, T. A. *ACS Nano* **2008**, *2*, 1799–1806.
238. Yamada, M.; Shen, Z.; Miyake, M. *Chem. Commun.* **2006**, 2569–2571.
239. Nie, Z.; Fava, D.; Kumacheva, E.; Zou, S.; Walker, G. C.; Rubinstein, M. *Nat. Mater.* **2007**, *6*, 609–614.
240. Lim, I. S.; Mott, D.; Ip, W.; Njoki, P. N.; Pan, Y.; Zhou, S.; Zhong, C.-J. *Langmuir* **2008**, *24*, 8857–8863.
241. Sun, Z.; Weihai, N.; Yang, Z.; Kou, X.; Li, L.; Wang, J. *Small* **2008**, *4*, 1287–1292.
242. Klajn, R.; Fang, L.; Coskun, A.; Olson, M. A.; Wesson, P. J.; Stoddart, J. F.; Grzybowski, B. A. *J. Am. Chem. Soc.* **2009**, *131*, 4233–4235.
243. Nykypanchuk, D.; Maye, M. M.; van der Lelie, D.; Gang, O. *Nature* **2008**, *451*, 549–552.
244. Park, S. Y.; Lytton-Jean, A. K. R.; Lee, B.; Weigand, S.; Schatz, G. C.; Mirkin, C. A. *Nature* **2008**, *451*, 553–556.
245. Sidhaye, D. S.; Kashyap, S.; Sastry, M.; Hotha, S.; Prasad, B. L. V. *Langmuir* **2005**, *21*, 7979–7984.
246. Singh, J. P.; Lee, P. P.; Nettesheim, F.; Wagner, N. J.; Furst, E. M. *Phys. Rev. E* **2009**, *79*, 050401.
247. Ming, T.; Kou, X.; Chen, H.; Wang, T.; Tam, H.-L.; Cheah, K.-W.; Chen, J.-Y.; Wang, J. *Angew. Chem. Int. Ed.* **2008**, *47*, 9685–9690.
248. Guerrero-Martínez, A.; Pérez-Juste, J.; Carbó-Argibay, E.; Tardajos, G.; Liz-Marzán, L. *Angew. Chem. Int. Ed.* **2009**, *48*, 9484–9488.
249. Zhao, N.; Liu, K.; Greener, J.; Nie, Z.; Kumacheva, E. *Nano Lett.* **2009**, *9*, 3077–3081.
250. Lee, S. H.; Liddell, C. M. *Small* **2009**, *5*, 1957–1962.
251. Pietrobon, B.; McEachran, M.; Kitaev, V. *ACS Nano* **2009**, *3*, 21–26.

252. Mittal, M.; Furst, E. M. *Adv. Mater.* **2009**, *19*, 3271–3278.
253. Ding, T.; Song, K.; Clays, K.; Tung, C.-H. *Adv. Mater.* **2009**, *21*, 1936–1940.
254. Gangwal, S.; Cayre, O. J.; Velev, O. D. *Langmuir* **2008**, *24*, 13312–13320.
255. Smoukov, S. K.; Gangwal, S.; Marquez, M.; Velev, O. D. *Soft Matter* **2009**, *5*, 1285–1292.
256. Brown, A. B. D.; Smith, C. G.; Rennie, A. R. *Phys. Rev. E* **2000**, *62*, 951–960.
257. Snyder, C. E.; Yake, A. M.; Feick, J. D.; Velegol, D. *Langmuir* **2004**, *21*, 4813–4815.
258. Rycenga, M.; McLellan, J. M.; Xia, Y. *Adv. Mater.* **2008**, *20*, 2416–2420.
259. Onoe, H.; Matsumoto, K.; Shimoyama, I. *Small* **2007**, *3*, 1383–1389.
260. Galisteo-López, J. F.; Ibisate, M.; Sapienza, R.; Froufe-Pérez, L. S.; Blanco, Á.; López, C. *Adv. Mater.* **2011**, *23*, 30–69.
261. Wang, D.; Salgueiriño-Maceira, V.; Liz-Marzán, L. M.; Caruso, F. *Adv. Mater.* **2002**, *14*, 908–912.

Chapter 2

Electric-Field-Assisted Convective Assembly of Colloidal Crystal Coatings

2.1 Introduction

A variety of methods have been demonstrated for self-assembly of colloidal crystals from suspensions of particles, as discussed in the previous chapter. Gravity¹ or electrophoresis² may be used to concentrate the particles, although the time for these processes may be long. Dielectrophoresis³⁻⁶ or magnetophoresis⁷ may also be used with the added benefit that the particles become polarized and align in chains so that they pack into single-domain crystals. Although the crystals that form are well-ordered, it is difficult to immobilize them permanently because the particles become resuspended when the field is removed. Convective assembly is another widely used colloidal assembly technique, which can be used for formation and deposition of thin crystalline coatings.⁸⁻¹² Convective assembly facilitates immobilization of the crystals and can be scaled up to coat large surfaces.^{13,14} However, it lacks mechanisms for aligning the particles that typically exist in the directed assembly methods based on external fields. Thus, the convective assembly process results in coatings that contain many small, randomly oriented crystal domains.

Several strategies for reducing the number of defects in coatings deposited by convective assembly have been tested. Marginal improvements in crystal uniformity have been achieved by incorporating sonication¹⁵ and using patterned substrate surfaces¹⁶ in the convective assembly method. The literature also contains one report of an electric field applied during convective assembly of colloidal particles.¹⁷ In this electric-field-based method, crystal coatings are deposited from an evaporating droplet moving by gravity down

an inclined substrate while an ac field is applied via electrodes along the edge of the substrate perpendicular to the droplet contact line. The field induces particle chaining parallel to the contact line, orienting the particles as they pack into a crystal structure, so fewer defects are observed compared to coatings deposited without an electric field. However, assembly by this technique is slow, requiring hours for a crystal of only a few square centimeters to form.

Here a new method for convective assembly in an electric field that achieves both rapid coating deposition and improved long-range ordering of particles is reported. This method is based on the electrowetting effect. In the electric-field-enhanced convective assembly method described here, electrowetting is used to extend a thin liquid film from the particle suspension meniscus. The following sections describe how this effect results in more rapid assembly of more uniform crystal coatings. The data are interpreted on the basis of enlargement of the area for solvent evaporation, which increases the evaporative flux and particle transport rate. The formation of larger crystal domains, believed to occur because electrowetting extends the space available for particle rearrangement, is also discussed.

2.2 Materials and Methods

2.2.1 Materials

Colloidal crystal coatings were assembled from 1.0 μm diameter polystyrene microspheres from Invitrogen (Carlsbad, CA) suspended in deionized (DI) water. The spheres were washed three times before use by centrifugation with a Fisher Marathon microA microcentrifuge (Waltham, MA) for 5 min at 3400 g and resuspension in DI water by sonication in a Branson 2510 ultrasonic cleaner (Branson Ultrasonics, Danbury, CT).

Following the final wash, the microspheres were resuspended at 16% volume fraction in a 0.05 wt% solution of Tween-20 from Sigma-Aldrich (St. Louis, MO) in DI water. The Tween-20 ensures uniform wetting of the substrate and thus prevents streaked coatings but does not affect the electrical properties of the suspension because of its low concentration. The water was supplied from a Millipore Milli-Q Plus water purification system (Billerica, MA).

The coatings were deposited on substrates from grade V1 mica sheets from Ted Pella (Redding, CA). Mica was chosen because it is hydrophilic, allowing formation of a wetting film of the particle suspension in which evaporative assembly can occur, and because it can be cleaved into thin sheets so the voltage drop across the substrates is low. One side of each sheet was coated with a 13 nm layer of chromium followed by a 100 nm layer of gold by metal vapor deposition. The mica was cleaved immediately before the convective assembly experiments to obtain 50–100 μm thick sheets with gold coatings on the bottom side and clean mica surfaces for coating deposition on the top side. The thicknesses of the mica sheets were measured using a Marathon electronic digital micrometer (model no. 030025) from Marathon Watch (Richmond Hill, ON).

2.2.2 Coating Deposition

The coatings were deposited using an apparatus operating by the convective assembly procedure described previously¹³ with an added capability for applying an electric field during the process. The apparatus is illustrated in Figure 2.1. The system consists of a clean glass microscope slide positioned at an angle in contact with a mica substrate. A droplet of a

suspension of microspheres is pinned in the wedge between the glass slide and the mica. As a linear motor pushes the glass slide, the particle suspension is dragged across the substrate and the crystal coating assembles at the trailing edge of the meniscus.

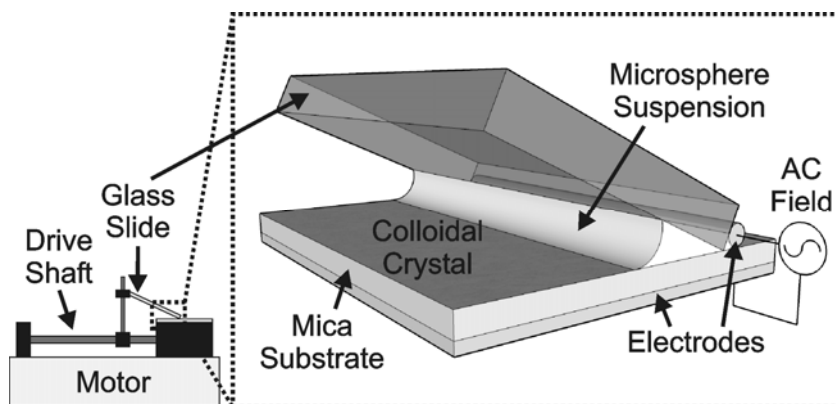


Figure 2.1. Schematics of the apparatus used to deposit colloidal crystal coatings by convective assembly in an electric field.

During assembly, a voltage was applied across the mica substrate and particle suspension droplet by two electrodes. The gold coating on the back of the mica substrate functioned as the working electrode. Copper tape was attached to the gold layer to provide a connection point for the voltage source. A copper wire was attached to the moving top glass slide at the edge where the slide contacted the mica substrate to function as the ground electrode. The particle suspension is drawn into contact with this wire by capillarity, and the wire moves with the top slide so that it is always in contact with the particle suspension. A 3 kHz ac electric field was applied between the electrodes. The frequency of 3 kHz was sufficiently high to avoid inducing vibration of the particle suspension meniscus, which was observed to break up the assembled coating at frequencies below 100 Hz. The amplitude of

the voltage varied from 0 V to 500 V. The voltage was supplied by a GW Instek GFG-8210 function generator (Tuchen City, Taiwan) connected to a Trek PZD700 amplifier (Medina, NY). A 0.68 μF 400 V capacitor was included in the circuit to remove any dc offset. An Agilent 34405A digital multimeter (Santa Clara, CA) was used to measure the voltage.

To begin the coating deposition, a 10 μl droplet of particle suspension was injected into a wedge between a mica substrate and a glass slide. The glass slide was pushed by a linear motor initially at a rate of 31.7 $\mu\text{m/s}$ until a coating began to form across the entire width of the substrate. At this time, a voltage was applied, and the rate was increased to 47.5 $\mu\text{m/s}$, which was approximately the rate at which a complete monolayer of microspheres assembled with no voltage applied. A continuous coating was deposited over a length of about 4 mm before the voltage was changed to another value. The particles deposited at a faster rate than the liquid evaporated, so the particle suspension concentration decreased as the coating grew. At the time the voltage was changed, the particle suspension was replaced with a fresh sample to maintain a consistent particle suspension concentration. The apparatus was enclosed in a plastic chamber so that the relative humidity could be maintained at 20–30%.

2.2.3 Characterization of the Coatings

The coatings deposited by this procedure were imaged by optical microscopy for analysis of the crystal structure. An Olympus SZ61 macroscope (Tokyo, Japan) with objective variable from 1X to 4X magnification equipped with a Sony DSC-V1 digital camera (Tokyo, Japan) was used to record millimeter scale images of coatings illuminated

with reflected white light. To view coatings at the micrometer scale, an Olympus BX61 microscope was used. The coatings were illuminated with transmitted white light, and images at 4X, 10X, and 50X objective magnification were recorded with an Olympus DP70 CCD camera.

2.3 Results and Discussion

2.3.1 Effect of Applied Voltage on Coating Deposition Rate

The deposition of uniform ordered particle films in the absence of electric field followed the process for convective assembly from high volume fraction colloidal suspensions described in detail earlier.¹³ The addition of an electric field to the process visibly increased the coating deposition rate and the size of the crystal domains. The relationship between crystal assembly rate and applied voltage was characterized by changing the voltage several times during coating deposition and measuring the number of particle layers deposited at each voltage.

The coating thickness was determined by optical microscopy. Crystals of different thicknesses were distinguished by the color arising from interference and diffraction of light transmitted through different numbers of particle layers.¹⁸ The monolayer areas were identified by the color of the coating adjacent to the uncoated substrate. The numbers of particle layers in multilayer domains of the coating were determined by counting the number of differently colored multilayer bands between these domains and the uncoated substrate. Additionally, bands of square-packed particles, the formation of which at the boundaries between different numbers of hexagonally-packed layers has been well described,¹⁰ were

used as visual indications of the transitions between areas containing different numbers of particle layers. In some cases, the voltage was higher than that required to deposit a certain number of particle layers but lower than that required to deposit the next higher number of layers, so the thickness alternated across the coating. The fractional average number of layers in these coatings was calculated by measuring the surface fraction of the coating made up of each color.

As a control, all of the coatings were deposited with 100 V applied initially, after which the voltage was changed to different values for each coating. The thickness of the mica substrate, which affects the voltage drop between the electrode under the substrate and the particle suspension, was identified as the primary factor that varied between each coating deposition experiment. Cleaving the mica to achieve exactly the same thickness for each sample was difficult, so the thicknesses of the substrates varied from 63 μm to 95 μm . To quantify the effect of the substrate thickness on the coating thickness, the data for the number of particle layers in the sections of the coatings deposited with 100 V applied were analyzed. A linear regression on the data found that the coating thickness is related to the substrate thickness by the equation

$$h_c = -0.0318h_s + 4.95 \quad (2.1)$$

where h_c is the average number of particle layers in the coating and h_s is the thickness of the substrate in μm . To compare the thicknesses of coatings deposited on substrates with different thicknesses, each coating thickness measurement $h_{c,meas}$ was converted to a normalized coating thickness value $h_{c,norm}$ corresponding to a substrate thickness of $h_s = 80 \mu\text{m}$ using a scaling relationship based on eq 2.1:

$$h_{c,norm} = \left(\frac{-0.0318(80) + 4.95}{-0.0318h_s + 4.95} \right) h_{c,meas} . \quad (2.2)$$

The substrate-thickness-normalized data are plotted in Figure 2.2. As the plot shows, the number of particle layers in the coatings increased severalfold with applied voltage. Even thicker crystal coatings were assembled with 250–500 V applied, but these coatings were too opaque to distinguish the number of particle layers by optical microscopy. The results suggest that the pronounced increase in the number of particle layers deposited as the applied voltage increases arises from spreading of the wetting film in front of the meniscus of the particle suspension by the electrowetting effect. In this system, the electrowetting effect occurs because the electric field polarizes the deposited porous coating, increasing its wettability by the particle suspension liquid and allowing the film to penetrate into the coating. The liquid flux compensating for evaporation from this drying film drives the crystal assembly in the convective deposition technique. The field-driven extension of the film increases the area for solvent evaporation and, therefore, the rate of convective transport of particles to the crystal growing at the meniscus.

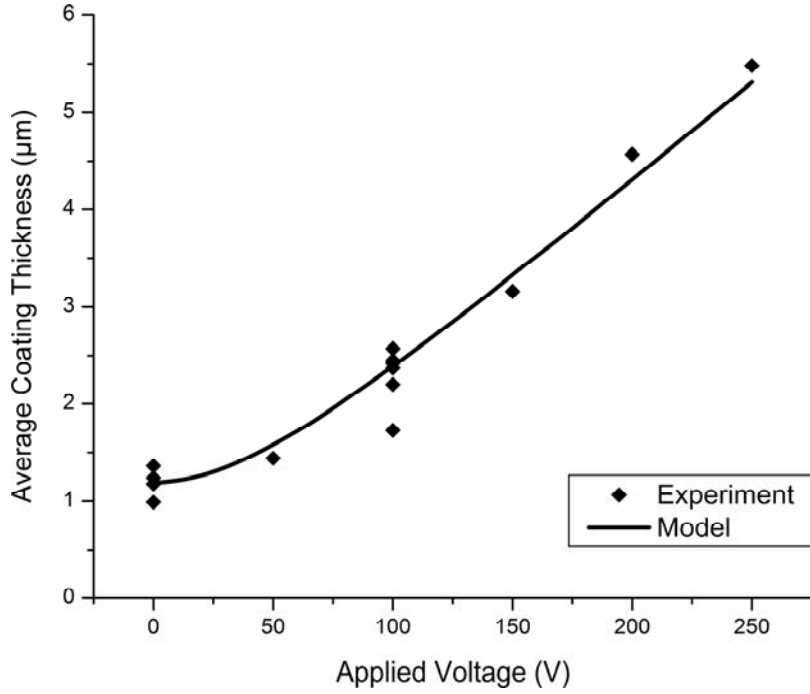


Figure 2.2. Plot of the average thicknesses of crystal coatings deposited with different voltages applied. The thicknesses of the coatings increased with the voltage. A model, which assumes that the increased assembly rate arises from electrowetting driven extension of the liquid film where the crystal forms, fits the experimental data well.

The process was analyzed quantitatively by combining convective assembly and electrowetting theories. The mass balance of the liquid flow during the convective assembly process has been described previously by the equation

$$v_c = \frac{\beta j_e l \varphi}{h(1-p)(1-\varphi)} \quad (2.3)$$

where v_c is the meniscus withdrawal speed, β accounts for particle-particle and particle-substrate interactions and approaches unity for dilute suspensions of nonadsorbing particles, j_e is the rate of liquid evaporation per unit length of the drying film, l is the length of the drying film, φ is the particle suspension volume fraction, and h and p are the crystal thickness

and porosity.¹¹ This model was extended to describe convective assembly with electrowetting by correlating the length of the drying film to the voltage V applied across the particle suspension and substrate. The parameters of the new model are illustrated in Figure 2.3.

When voltage is applied, the drying length is given by

$$l = l_0 + l_{EW} \quad (2.4)$$

where l_0 is the length of the film with no voltage applied and l_{EW} is the length by which electrowetting extends the film. The magnitude of the force from electrowetting on the film is given by

$$F_{EW} = \frac{\varepsilon_D \varepsilon_0 V^2}{2d} \quad (2.5)$$

where ε_D and d are the dielectric constant and thickness of the mica substrate.¹⁹ Dividing this force by the height of the film results in the equation for the pressure generated by electrowetting on the cross-section of the film per unit length of the meniscus.

$$P_{EW} = \frac{\varepsilon_D \varepsilon_0 V^2}{2dh} \quad (2.6)$$

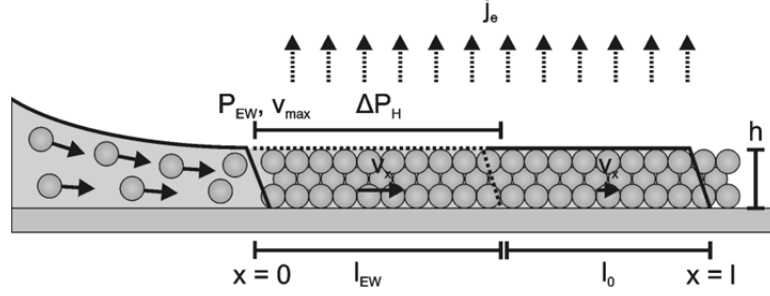


Figure 2.3. Schematic of the parameters for the model of voltage-driven extension of the particle suspension drying film. The voltage induces a pressure P_{EW} that pulls the drying film away from the droplet, increasing its length by l_{EW} from its original length l_0 . This spreading is limited by the pressure drop ΔP_H of the liquid flowing through the porous coating already deposited on the substrate. The liquid velocity v_x decreases as the liquid evaporates at a rate of j_e along the film. As the voltage increases the total length of the film l , the thickness of the deposited coating h increases as more particles are deposited at the growing crystal front.

The porous crystal coating deposited on the substrate introduces a drag force that opposes extension of the drying film by the electrowetting force. Darcy's Law, a conservation of momentum equation for flow through a porous media derived from the Navier-Stokes equations and given by

$$\frac{dP}{dx} = \frac{\mu}{k_D} v_x \quad (2.7)$$

for one-dimensional flow,²⁰ is used to evaluate the pressure drop for the penetration of the film into the crystal coating. In this equation, μ is the liquid viscosity and k_D is the experimentally determined Darcy permeability. Moving along the drying length away from the bulk suspension, the liquid evaporates and the velocity of the liquid in the meniscus is assumed to decrease according to the linear scaling relation

$$v_x = v_{max} \left(1 - \frac{x}{l} \right). \quad (2.8)$$

The maximum velocity v_{max} occurs at the boundary between the drying film and the bulk suspension and is calculated using the equation

$$v_{max} = \frac{j_e l}{h} \quad (2.9)$$

Substituting these velocity equations into Darcy's Law and integrating over the length that the film is extended by the electrowetting force l_{EW} yields the equation

$$\Delta P_H = \frac{\mu j_e}{k_D h} \left(\frac{1}{2} l_{EW}^2 + l_0 l_{EW} \right) \quad (2.10)$$

for the pressure drop of the film as it flows through the crystal coating. Balancing the pressure induced by electrowetting given by eq 2.6 and the hydrodynamic pressure drop given by eq 2.10, solving the resulting quadratic equation, and taking the physically meaningful positive root, yields the following equation for the drying length.

$$l = \sqrt{l_0^2 + \frac{k_D \epsilon_D \epsilon_0}{\mu j_e d} V^2} \quad (2.11)$$

The drying length with no applied voltage l_0 in the above equation is calculated from experimental data using eq 2.3. Corresponding to the experimental conditions, v_c is 47.5 $\mu\text{m/s}$ and ϕ is 0.16. The average number of particle layers deposited with no applied voltage is 1.19, so $(1-p)$ is 0.6046, corresponding to a monolayer of particles,¹³ and h is 1.19 μm , because the particles were 1 μm in diameter. The value of $j_e = 0.1 \mu\text{m/s}$ has been previously reported.¹³ The drying length with no applied voltage is 1800 μm , which was consistent with the length of an experimentally observed "wet" band trailing the particle suspension meniscus that appeared slightly darker than the dried crystal coating.

The thickness of a coating deposited by convective assembly over the voltage range of 0–250 V was estimated from the mass balance, eq 2.3, rearranged to the form

$$h = \frac{\beta j_e l \varphi}{v_c (1-p)(1-\varphi)}. \quad (2.12)$$

The experimental values for β , j_e , φ , v_c , and p are used in this equation, and the drying length of the meniscus extended by the electrowetting force is calculated using eq 2.11. The only fitting parameter for this model is the Darcy permeability. The value of $k_D = 1.6 \times 10^{-13} \text{ m}^2$ minimizes the sum of the squared deviations between the model predictions and experimental data, resulting in the curve plotted in Figure 2.2.

The Darcy permeability for this system is difficult to predict from theory. However, the validity of the above model can be evaluated by comparing the experimental best fit for k to two other cases for which k can be calculated: a channel filled with porous media and an open surface with no crystal coating. The Darcy permeability of a liquid flowing through a medium of uniform closely packed spheres of diameter D_P in a channel can be estimated using the Kozeny-Carman equation²⁰

$$k_{K-C} = \frac{D_P^2 p^3}{180(1-p)^2}. \quad (2.13)$$

For the relevant values of D_P and p , k_{K-C} is $9.4 \times 10^{-16} \text{ m}^2$. The Kozeny-Carmen permeability is smaller than the experimental permeability because a closed channel would restrict flow more than the open surface in the system described here.

Alternatively, a comparable “permeability” can be calculated on the basis of the hydrodynamic resistance experienced by a liquid flowing across an uncoated open surface by

solving the Navier-Stokes equations for steady-state, fully developed, unidirectional flow using the lubrication approximation. Integrating and applying the no slip boundary condition at the substrate and the zero shear stress boundary condition at the air interface yields

$$\frac{dP}{dx} = \left(\frac{2\mu}{y^2 - 2hy} \right) v_x. \quad (2.14)$$

By solving this equation instead of Darcy's Law, the effective permeability for a film flowing over a surface not coated with a crystal is

$$k_{surface} = \frac{h^2}{3} = 3.3 \times 10^{-13} \text{ m}^2. \quad (2.15)$$

This open surface permeability value is larger than the experimental data fit, which is expected because a liquid would flow more easily over an uncoated surface than through a porous crystal on a surface.

In summary, the model matches the experimental data when the permeability fitting parameter is less than the value for a packed closed channel but greater than the value for an uncoated open surface. Likewise, the experimental system, a liquid flowing through a bed of spheres open on one side, is physically between the two predictable cases, so the experimental fit permeability is reasonable. This result is significant because it supports the proposed mechanism by which the rate of convective assembly is increased by electrowetting driven extension of the drying film. The model additionally provides a means to tune the coating deposition process.

2.3.2 *Effect of Electric Field on Crystal Uniformity*

In addition to increasing the crystal assembly rate, the electric field improves the long range uniformity of the crystal structure, as seen by comparing the sizes of the crystal domains in the coatings shown in Figure 2.4a. This desirable effect was evaluated quantitatively by examining two sets of monolayer coatings, one deposited with no applied voltage and one deposited with 50 V applied. The applied voltage was low enough to prevent formation of multilayer coatings, which would complicate measurement of individual domain characteristics. The hexagonal packing crystal structure of the coatings, as visible in Figure 2.4b, results in three axes of symmetry through any node in the crystal. An area in a coating where the axes through all the particles are aligned in the same direction is defined as a crystal domain. Defects in the coating marked by dotted lines in the image are boundaries between crystal domains. Other defects in the coating appear where there are irregularities in particle spacing that occur during the coating drying process. However, these defects are within areas of uniform particle alignment and are, therefore, not considered domain boundaries. The uniformity of the coatings was characterized by the domain sizes and axes orientations.

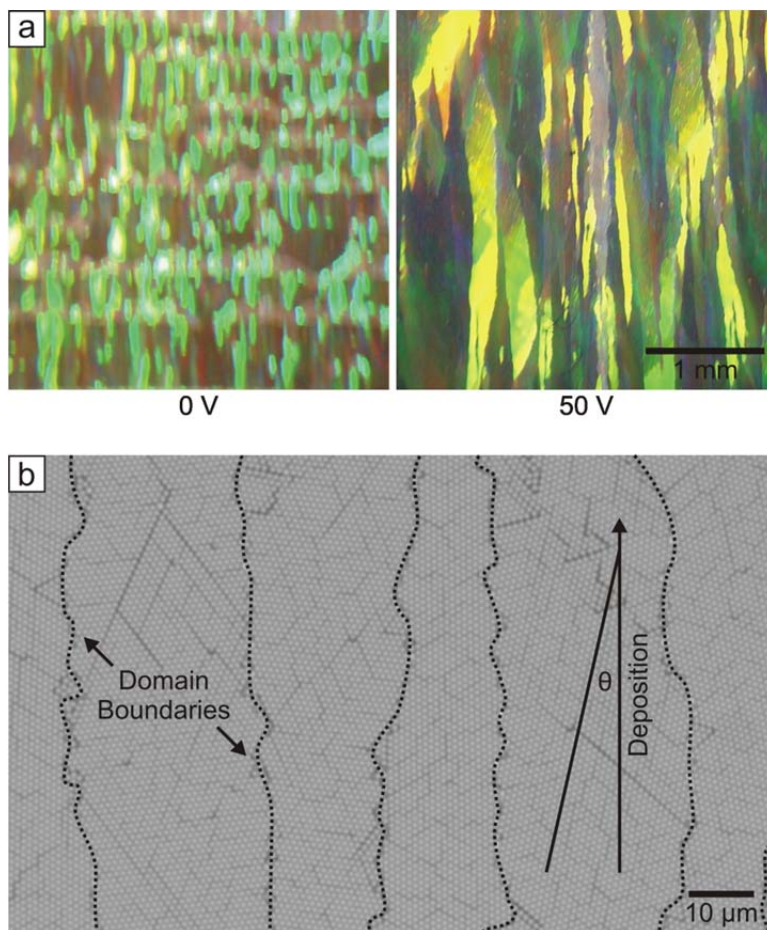


Figure 2.4. (a) Images of crystal domains in coatings deposited with and without an electric field and (b) optical micrograph showing individual particles in a crystal coating deposited without an electric field and the alignments of domains.

To analyze domain sizes, the coatings were illuminated with white light from the right, so that the different domains diffracted light of different wavelengths depending on the relative angle of orientation of their axes, as shown in Figure 2.4a. The length and width of each domain in the optical images were measured using Adobe Photoshop and multiplied to estimate the area. The domains were separated into three categories based on their areas: $0-10^4 \mu\text{m}^2$, $10^4-10^5 \mu\text{m}^2$, and $10^5-10^6 \mu\text{m}^2$. The areas of all of the domains in each category

were added to determine the fraction of the total coating composed of domains in each area range. The coatings assembled with no applied voltage were primarily composed of domains in the 10^4 – $10^5 \mu\text{m}^2$ range, while the coatings assembled with 50 V applied were composed mostly of domains an order of magnitude larger in the 10^5 – $10^6 \mu\text{m}^2$ size range, as shown by the histogram in Figure 2.5. Consistent with this analysis, the average domain size for the coatings assembled with no applied voltage was $1.2 \times 10^4 \mu\text{m}^2$ while the average domain size for the coatings assembled with 50 V applied was $6.4 \times 10^4 \mu\text{m}^2$. The increased domain size in coatings deposited in an electric field is believed to be a consequence of the electrowetting effect which is also responsible for the increased crystal assembly rate. Extension of the drying film in which the crystal assembles allows more time for particles to rearrange and pack with fewer defects before the coating dries and the particles become permanently immobilized.

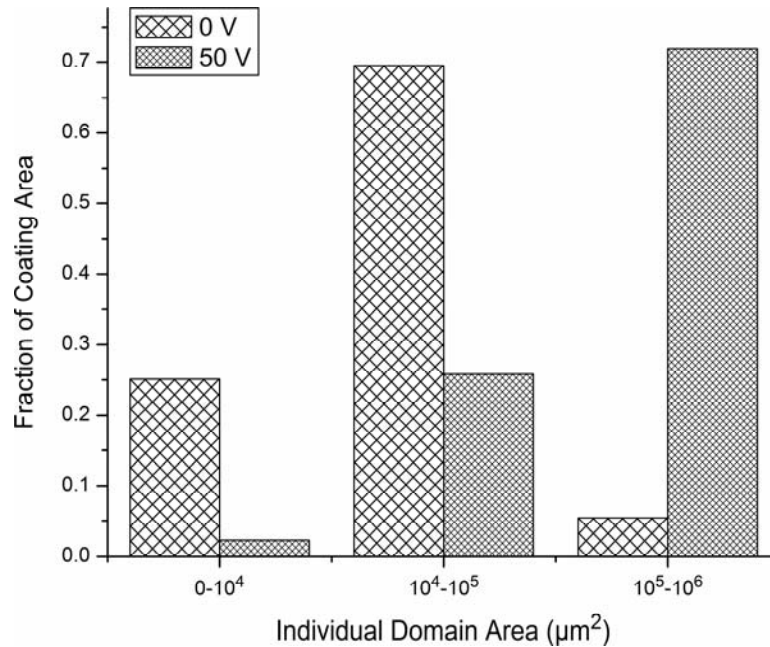


Figure 2.5. Histogram comparing the sizes of crystal domains in coatings deposited with and without an electric field. Coatings deposited in an electric field were made up of larger domains than coatings deposited with no electric field.

The coatings were also analyzed to determine if the electric field engendered a specific angle of domain alignment. The electric field that extends through the volume of the liquid meniscus was expected to induce particle chaining as observed in dielectrophoretic crystal assembly.⁴ The formation of short, loose chains of particles aligned perpendicular to the crystal front in the meniscus was observed during the experiment by optical microscopy. These chains were dragged toward and incorporated into the growing crystal front. If the chaining direction was maintained as the coating dried, it could lead to alignment of the particles in the crystal lattice such that the orientations of the axes of symmetry would be more uniform across the coating.

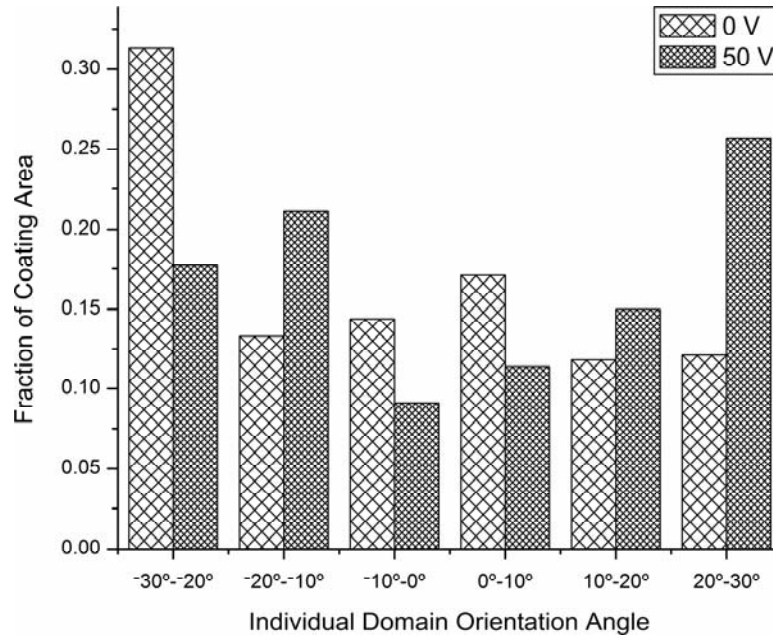


Figure 2.6. Histogram comparing the alignments of crystal domains in coatings deposited with and without an electric field. There was no clear effect of the domains in the coatings deposited in an electric field orienting along the field lines.

To evaluate whether the formation of suspended chains results in better domain orientation in the assembled crystals, the dry coatings were imaged at high magnification so that individual particles could be distinguished, as shown in Figure 2.4b. The hexagonal particle packing means that at least one of the axes of symmetry must be within 30° of the direction of the electric field lines. The data for the smallest angle at which the axes of symmetry of each domain deviate from the direction of the electric field were divided into 6 interval categories based on the domain orientation angle: $0^\circ\text{--}\pm 10^\circ$, $\pm 10^\circ\text{--}\pm 20^\circ$, and $\pm 20^\circ\text{--}\pm 30^\circ$. Domains designated with a 0° orientation angle had an axis of symmetry that was parallel to the electric field lines. This analysis revealed no obvious dependence of domain alignment on the presence of an electric field, as the histogram in Figure 2.6 shows. The

separate crystal domains are believed to grow from randomly oriented nuclei of particles that form in the convective front, a phenomenon previously reported for coatings deposited by evaporation-driven assembly.¹⁰ Although electric field induced particle chaining in the particle suspension meniscus was observed during crystal assembly, the chains are believed to conform to the domain alignments dictated by the already existing nucleation sites in the growing front as they pack into the crystal.

2.4 Conclusions

The results presented here demonstrate a new technique of convective assembly where the application of an electric field during the process increases the rate of colloidal crystal coating deposition and the size of crystal domains. Because of the electrowetting effect, the electric field extends the drying film where the crystal assembles. Compared to convective assembly without an electric field, the new method results in a fivefold increase in the rate of crystal assembly because of the larger liquid surface area available for evaporation. Thus, electric-field-assisted convective assembly is able to deposit in minutes coatings that would otherwise require hours for deposition by dip coating assembly.^{11,12} In addition, the sizes of the single crystal domains increase more than five times, though the orientations of their axes remain largely random. While the present method is unable to produce crystal domains as large as the ones obtained dielectrophoretically when an electric field is applied to a suspension of freely suspended particles,⁴ it results in permanently immobilized coatings featuring crystal domains with dimensions as large as several

millimeters. By rapidly producing well-ordered coatings, the method may be useful for large-scale production of better colloidal crystal films.

2.5 References

1. Pieranski, P. *Contemp. Phys.* **1983**, *24*, 25–73.
2. Giersig, M.; Mulvaney, P. *Langmuir* **1993**, *9*, 3408–3413.
3. Velev, O. D.; Bhatt, K. H. *Soft Matter* **2006**, *2*, 738–750.
4. Lumsdon, S. O.; Kaler, E. W.; Williams, J. P.; Velev, O. D. *Appl. Phys. Lett.* **2003**, *82*, 949–951.
5. Gupta, S.; Alargova, R. G.; Kilpatrick, P. K.; Velev, O. D. *Soft Matter* **2008**, *4*, 726–730.
6. Gangwal, S.; Cayre, O. J.; Velev, O. D. *Langmuir* **2008**, *23*, 13312–13320.
7. Dimitrov, A. S.; Takahashi, T.; Furusawa, K.; Nagayama, K. *J. Phys. Chem.* **1996**, *100*, 3163–3168.
8. Kralchevsky, P. A.; Denkov, N. D. *Current Opinion in Colloid & Interface Science* **2001**, *6*, 383–401.
9. Velev, O. D.; Lenhoff, A. M. *Current Opinion in Colloid & Interface Science* **2000**, *5*, 56–63.
10. Denkov, N. D.; Velev, O. D.; Kralchevsky, P. A.; Ivanov, I. B.; Yoshimura, H.; Nagayama, K. *Langmuir* **1992**, *8*, 3183–3190.
11. Dimitrov, A. S.; Nagayama, K. *Langmuir* **1996**, *12*, 1303–1311.
12. Jiang, P.; Bertone, J. F.; Hwang, K. S.; Colvin, V. L. *Chem. Mater.* **1999**, *11*, 2132–2140.
13. Prevo, B. G.; Velev, O. D. *Langmuir* **2004**, *20*, 2099–2107.
14. Prevo, B. G.; Kuncicky, D. M.; Velev, O. D. *Colloids and Surfaces A: Physicochem. Eng. Aspects* **2007**, *311*, 2–10.
15. Sasaki, M.; Hane, K. *J. Appl. Phys.* **1996**, *80*, 5427–5431.

16. Zhang, J.; Alsayed, A.; Lin, K. H.; Sanyal, S.; Zhang, F.; Pao, W.-J.; Balagurusamy, V. S. K.; Heiney, P. A.; Yodh, A. G. *Appl. Phys. Lett.* **2002**, *81*, 3176–3178.
17. Schope, H. J. *J. Phys.: Condens. Matter* **2003**, *15*, L533–L540.
18. Dushkin, C. D.; Nagayama, K.; Miwa, T.; Kralchevsky, P. A. *Langmuir* **1993**, *9*, 3695–3701.
19. Jones, T. B. *Langmuir* **2002**, *18*, 4437–4443.
20. Probstein, D. F. *Physicochemical Hydrodynamics: An Introduction*; Butterworths: Boston, 1989 ; pp 98–100.

Chapter 3

The Dynamics and Stability of Lubricating Oil Films During Droplet Transport by Electrowetting in Microfluidic Devices

3.1 Introduction

The concept of droplet microfluidics, in which discrete droplets are formed and manipulated in an immiscible liquid phase, is an alternative with distinct advantages to the continuous flow microfluidics devices.¹⁻³ Each droplet functions as an independent microreactor, so many parallel assays can be performed without resorting to highly repetitive and, therefore, complex device designs. Because protocols are executed by performing operations on droplets individually, flexibility in the types of assays that can be performed is achieved through the ability to change the composition, number, and sequence of droplets without altering the device itself. The continuous phase has several roles, including maintaining spacing between the droplets,⁴ preventing evaporation of the droplets,⁹ lubricating droplet motion,^{5,6} and inhibiting molecular transfer between droplets and adsorption from droplets to device surfaces.^{5,7} Consequently, the stability of this phase, particularly between the droplets and device surfaces where it exists as a fragile thin film, is critical to reliable device operation.

The oil films in microfluidic devices relying on electrowetting to manipulate droplets are a uniquely complex system, and the thickness and stability of the films have not yet been investigated extensively. Microfluidic devices operating by electrowetting typically consist of two parallel conducting plates separated by a narrow gap. The conductive layer on one plate is patterned to form an array of individually addressable electrodes and is covered by a

hydrophobic dielectric coating. A droplet sandwiched between the two plates and surrounded by an oil medium can be moved over the array by switching on an electrode beside the droplet, causing it to spread onto the newly activated surface, while simultaneously switching off the electrode directly under the droplet.⁸ By repeating this action, droplets can be transported, split, and merged in a highly controlled manner.⁹ The speed at which droplets are transported in the device is affected primarily by the magnitude of the voltage and the oil viscosity.¹⁰ The droplet speed increases with voltage between the minimum and maximum values imposed by contact angle hysteresis and saturation, respectively.¹¹ Increasing the oil viscosity slows the droplets.

The thin film between a solid surface and a tangentially moving fluid interface in pressure-driven flow systems has been studied for decades and is relevant to coating¹² and hydrocarbon extraction processes.¹³ While a variety of complex models have been developed to describe the flow in these films, most have as their starting point the work of Landau and Levich¹² on the liquid film formed on a flat plate vertically withdrawn from a liquid bath or of Bretherton¹⁴ on the film that forms around a bubble moving through a liquid-filled capillary. Both theories divide the flow into two regions—the first, a meniscus of gradually increasing curvature which is a transition from the bulk liquid to the second, a flat, thin film. By applying the method of asymptotic expansions to the differential equations and boundary conditions governing both regions, the film thickness D can be calculated using the equation

$$D = 1.34RCa^{2/3} \quad (3.1)$$

where the capillary number Ca is given by

$$Ca = \frac{\mu U}{\gamma}, \quad (3.2)$$

R is the radius of curvature of the meniscus or capillary, μ is the viscosity of the liquid in the film, U is the plate withdrawal or bubble speed, and γ is the surface tension of the liquid. Eq 3.1 is valid at Ca less than 0.01; at higher Ca , the film thickness reaches a plateau.¹⁵ More recently, a model confirmed that eq 3.1 is also accurate for a film that forms as a droplet moves through a Hele-Shaw cell, a narrow slit between two parallel plates that more closely matches the device geometry considered here.¹⁶ While the Landau-Levich and Bretherton theories assume an air-water interface, modifications to the models have also been made for systems consisting of two viscous phases. As the viscosity of the droplet phase increases, flows inside the droplet begin to affect the velocity at the droplet-film interface, causing liquid to be entrained in the film. The film thickness predicted by eq 3.1 increases by a factor of $2^{2/3}$ at high droplet viscosities and as large as $4^{2/3}$ at intermediate droplet viscosities relative to the continuous phase viscosity.^{13,17}

Addition of surfactant to either the droplet or continuous phase also affects the film thickness, as demonstrated by several studies extending the work of Bretherton on the system of a bubble or droplet moving through a capillary. Nonuniform distribution of trace amounts of surfactant over the interface can create stresses that entrain liquid into the film. During bubble motion, convective flows cause surfactant to accumulate at the leading end of the bubble and to become depleted in the adjacent region of the film. The lower interfacial tension in the bubble cap relative to the film creates a Marangoni stress that thickens the film by a factor as high as $4^{2/3}$.¹⁸ The extent of the film thickening from the surfactant

concentration gradient depends on the transport kinetics of the molecules. At low surfactant concentration, replenishment of displaced molecules at the interface is likely to be diffusion-limited, so the interfacial tension gradient is sustained.¹⁸ Likewise, slow adsorption or desorption of surfactant from the interface allows surfactant concentration and interfacial tension gradients to be maintained.¹⁹ However, at high bulk concentrations, rapid diffusion coupled to rapid adsorption or desorption to or from the interface can diminish the concentration gradient at the interface so that the film thickness is not increased.^{19,20} Rapid surface convection also precludes film thickening.¹⁸ The Marangoni effect also becomes insignificant at high bubble velocities.¹⁸

The oil films between droplets and substrates in electrowetting systems have been the subject of only a few studies. A theoretical analysis predicted that an oil layer of less than 400 nm thickness completely wetting a dielectric substrate in an aqueous medium would transition to a film with thickness on the order of 25 nm in equilibrium with a macroscopic oil droplet when electrowetting was induced by applying a voltage across the system.²¹ Van der Waals interactions provided the basis for the existence of this pseudopartial wetting state instead of a partial wetting state with the water directly contacting the dielectric around the oil droplet. For films of larger initial thickness, the electrostatic pressure engendered by the voltage may lead to spinodal dewetting, wherein capillary waves arise at the fluid interface and lead to break up of the film. Consistent with that expectation, an experimental investigation showed that an oil film entrapped by a water droplet spreading by electrowetting over a dielectric substrate dewetted into an array of discrete oil droplets over the surface when the equilibrium electrowetting radius was reached.²² The speed of the

droplet spreading and the oil meniscus receding was varied by adjusting the rate at which the voltage was increased from zero to a fixed value, and the thickness of the entrapped film was found to follow a relationship similar to the Landau-Levich dipcoating model modified to account for the electrostatic pressure. The oil droplet diameters corresponded to the wavelengths of variations in film thickness predicted by a linear stability analysis. The study suggested that the film thickness profile is governed by the dynamics of the receding oil meniscus.

While the previous investigations have provided some insight into the behavior of oil films during electrowetting, there are several important differences between those experiments and the configurations of lab-on-a-chip devices. In the previous experiments, applying voltage caused a spherical water droplet in ambient oil to approach and spread on a surface, symmetrically entrapping oil and forming a film. In the lab-on-a-chip devices, the droplets are confined between two plates and are, thus, disk-shaped, with oil films existing even before voltage is applied where the droplets are pressed flat against the plates. Rather than the centers of the droplets remaining stationary and the edges expanding to cover more of the dielectric surface as in the experiment described in the previous paragraph, the applied voltage causes the droplets move laterally through the device. The oil menisci recede at higher speeds because the voltage is switched from zero to a high voltage as a step rather than ramping the voltage, which is significant because the velocity of the receding meniscus is a critical parameter governing the film thickness. Moreover, the electrowetting effect occurs only at the surface coated with a dielectric layer; the film at the opposite surface has not yet been examined. This report presents an investigation of the behavior of oil films in an

electrowetting-actuated, droplet-based lab-on-a-chip device. The distinct dynamics of films at both surfaces are examined, and the conditions under which films are stable and unstable are explained. Finally, the effects on the films from surfactants, which are almost always present in chemical or biochemical analytical systems, are reported.

3.2 Materials and Methods

The lab-on-a-chip system used in the experiments described here consisted of two main components: a microfluidic cartridge in which droplets in a narrow, oil-filled gap between two parallel plates were moved in two dimensions by electrowetting and a computer-programmable electronic circuit that controlled the voltage applied to each electrode in the cartridge to cause droplets to undergo a user-defined sequence of actions. A new cartridge was used for each experiment. The oil films between the droplets and the cartridge surfaces were observed by interference microscopy.

3.2.1 Microfluidic Cartridge Construction

Each microfluidic cartridge, depicted in Figure 3.1, was made from two glass plates coated with a conductive layer of indium tin oxide (ITO). The optically transparent plates permitted microscopic observation of the oil films inside the cartridges. Electrowetting occurred at the surface of only one of the plates. The conductive layer on this plate functioned as a working electrode, and the surface was laminated with a polymer film which formed the dielectric layer necessary for electrowetting. The other plate, termed the reference surface, contacted the droplet directly to complete the circuit. Both plates were hydrophobized by a fluoropolymer using dip coating.

Two versions of the working electrode plate were fabricated. One type featured a continuous conductive layer and was used to make cartridges in which the droplets remained stationary during electrowetting. The other had an array of droplet-sized electrodes patterned into the ITO layer by standard photolithography and wet etching processes, allowing droplets to be transported laterally through the cartridge by sequentially applying voltage to a row of electrodes. Each plate had five parallel lanes of ten 1×1 mm electrodes and 2×3 mm reservoir electrodes at both ends of each lane. The two versions of the cartridge allowed the effects of electrostatic pressure and droplet motion on the oil films to be studied independently.

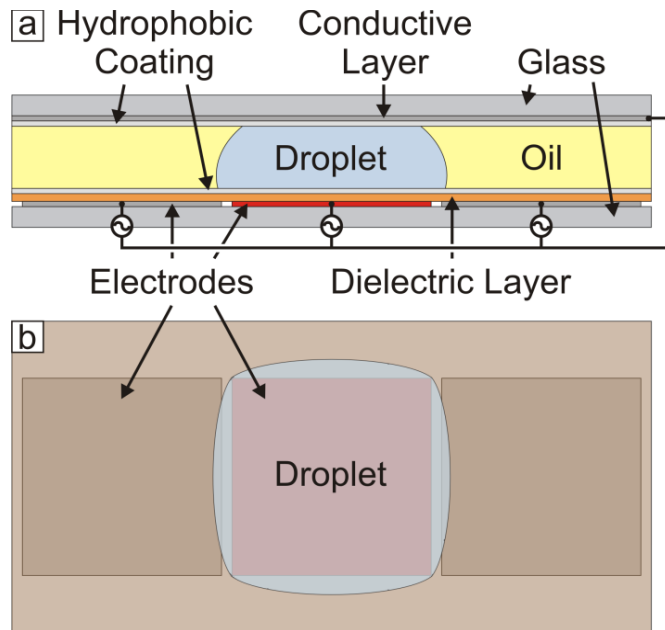


Figure 3.1. Schematic illustrating the (a) side and (b) top view of an electrowetting-actuated microfluidic device. Droplets are confined to an oil-filled slit between a top plate and substrate featuring an array of electrodes. By applying a voltage at an electrode (shown in red), a droplet can be moved there from an adjacent electrode by electrowetting.

After coating, the two plates were placed together with the conductive sides facing each other and held by microscope stage clips on an acrylic platform. The gap between the plates was filled with silicone oil. For the stationary electrowetting cartridges, a 300 nl water droplet was deposited into the oil using a pipette. Several microliters of water were loaded through holes drilled in the top plates into the reservoirs on the cartridges designed for droplet transport, and droplets were dispensed from the reservoirs using previously described electrode actuation sequences.⁹

3.2.2 Liquid Phase Materials

The silicone oil used to fill the microfluidic cartridges was 2 cSt trimethylsiloxy-terminated polydimethylsiloxane (PDMS) from Gelest (Morrisville, Pennsylvania). The droplet phase was deionized water to which potassium chloride was added at a concentration of 100 mM to ensure good conductivity as required for electrowetting. To study the effects of surfactants on the oil films, Tween 20 surfactant or Triton X-15 surfactant from Sigma-Aldrich (St. Louis, Missouri) was added to the droplet or oil phase, respectively. Surfactants are often classified by hydrophilic-lipophilic balance (HLB), a scale ranging from 0 to 20 on which 0 indicates a water insoluble molecule and 20 indicates a lipid insoluble molecule. The non-ionic surfactant Tween-20, commonly used in buffers for biochemical assays, has an HLB of 16.7, while the more lipophilic surfactant Triton X-15 has an HLB value of 4.9.

3.2.3 Electrical Instrumentation

Voltage was provided to each electrode on the cartridge by a computer-controlled circuit designed and built by Advanced Liquid Logic (Durham, NC) for commercial droplet-

based microfluidic products. The hardware was modified to allow the cartridges to fit on a microscope stage. Electrical potentials were generated and delivered through an array of 64 independently switchable pins. Switching of the voltage to the different electrodes was programmed and executed using software developed by Advanced Liquid Logic. For all experiments, except where stated otherwise, droplets were manipulated using voltage of 275 V at a frequency of 100 Hz.

3.2.4 Characterization

The oil films between droplets and device surfaces were examined by interference microscopy using an Olympus BX41 microscope operating in reflected light mode. A 550 nm bandpass filter was placed in the illuminating light path to provide a monochromatic beam. The films were observed through 10X, 20X and 40X objectives, and images and videos were recorded using a JAI CV-S3200 camera with DScaler software. Side-view, slow-motion videos of droplet transport were recorded using an EoSens mini2 camera from Mikrotron (Unterschleissheim, Germany) at a frame rate of 2500 fps and 10X magnification.

The interfacial tensions of the combinations of surfactant-containing droplet and oil phases were measured using a CAM 101 goniometer from KSV (Espoo, Finland). Droplets of the water phase were held at the tip of a needle immersed in the oil phase for 2 min to allow the surfactant concentration at the droplet surface to reach equilibrium. Then, 10 images of each droplet were recorded at 3 s intervals. The values for the interfacial tension were calculated based on the shapes of the droplets by an algorithm in the software accompanying the instrument.

3.3 Results

3.3.1 Static Oil Films

Oil films were initially observed immediately after loading a droplet into a cartridge and before applying voltage. An example of an interferograph of the film formed when the droplet was pressed flat against the cartridge is shown in Figure 3.2. The interference patterns appear in the film because the monochromatic light waves reflected from the cartridge surface and the oil-droplet interface interfere alternately constructively and destructively as the film thickness varies. The thickness at any point in the film can be calculated using the equation

$$h = \frac{\lambda}{2\pi n_f} \left(l\pi \pm \arcsin \sqrt{\Delta I} \right) \quad (3.3)$$

where λ is the wavelength of the light, n_f is the refractive index of the oil, and l is the order of interference.²³ The relative light intensity ΔI is calculated by

$$\Delta I = \frac{I_{max} - I}{I_{max} - I_{min}} \quad (3.4)$$

where I_{max} and I_{min} are the maximum and minimum light intensity in the film, and I is the light intensity at the point of the film being measured. For the present system, $\lambda = 550$ nm, $n_f = 1.39$, and the difference in the film thickness between two adjacent interference bands was 198 nm.

The broadening bands encircling the inside edge of the film, as in Box 1 of Figure 3.2, suggest that the oil meniscus surrounding the droplet transitions to a thin oil film rather than ending at a three-phase contact line. The interference patterns over the entire flattened

area of the droplet indicate that the oil film is continuous, yet of uneven thickness. Concentric rings of more closely spaced interference fringes, as in Boxes 2 and 3 of Figure 3.2, indicate oil dome-shaped lenses where the film is thicker to accommodate aberrations on the cartridge surface such as protrusions from the coating or dust particles. The large areas of consistent intensity indicate flat, thin films. The thickness of the film in these areas was estimated to be less than 50 nm by comparing the light intensity in these areas in images of several films to the darkest and brightest points in the same images and assuming the lowest order of interference. The film remained static as long as it was not perturbed.

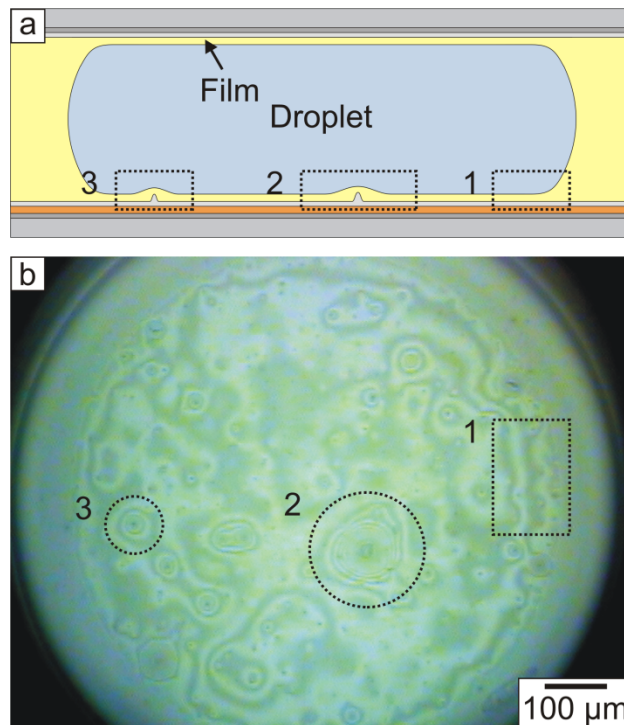


Figure 3.2. Schematic (a) and interference micrograph (b) showing a thin film between a droplet and cartridge surface before voltage was applied. The broadening interference bands around the edge of the film (1) show a transition from an oil meniscus to a thin film rather than a three-phase contact line. Oil lenses (2 and 3), circular regions where the film is thicker, appear in the center of the film.

3.3.2 Oil Films Formed During Stationary-Droplet Electrowetting

The next experimental observations included oil films formed when voltage was applied to induce electrowetting while droplets remained stationary in the cartridges featuring a single large working electrode surface, illustrated in Figures 3.3a and 3.3c. When voltage was applied, the film thinned at both the reference surface and the electrowetting surface, and the oil was displaced into lenses across the flattened area of the droplet, as observed to the right of the meniscus in Figure 3.3b. In addition to thinning, the film on the dielectric layer also expanded in area as the droplet spread due to electrowetting. As the oil meniscus receded around the droplet, waves formed and evolved into lenses in the newly created film, as shown in the boxes in Figure 3.3b. At the reference surface, the area of the film was reduced as the shape of the droplet changed to compensate for the spreading at the electrowetting surface. Because the oil meniscus was advancing, there was no wave formation in the film. When the electrodes were deactivated and the droplet returned to its original shape, the films returned to their original sizes and thicknesses, and the lenses flattened.

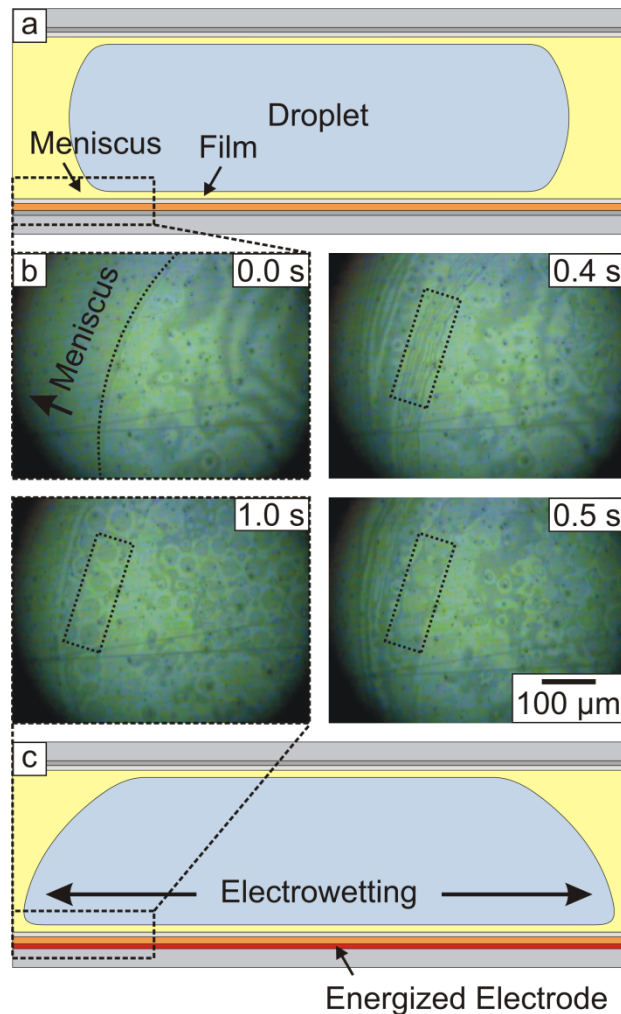


Figure 3.3. Schematics (a & c) and interference micrographs (b) showing the evolution of an oil film between a stationary droplet and the electrowetting surface after voltage was applied. (a) Initially, the droplet was symmetrical at the top and bottom surfaces of the cartridge. (b & c) When the voltage was applied, the droplet spread to cover more area of the dielectric film on the working electrode. Waves formed in the film at the receding oil meniscus and developed into circular oil lenses, as shown in the dotted box in (b). Oil was displaced into lenses in the center of the film because the electrostatic pressure thinned the film.

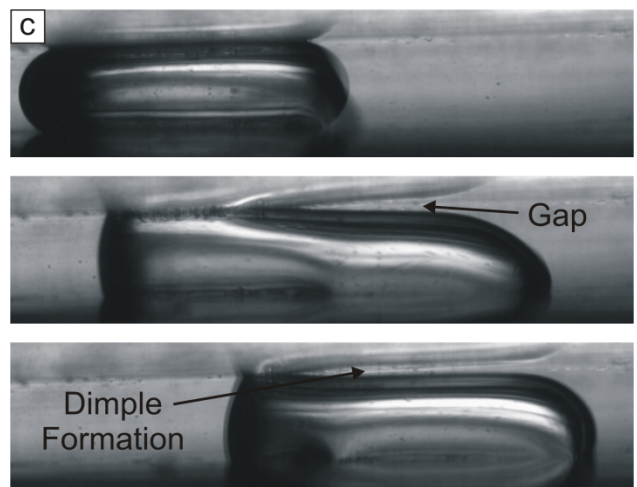
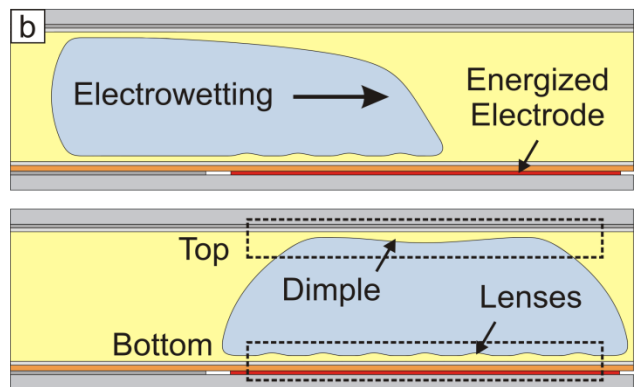
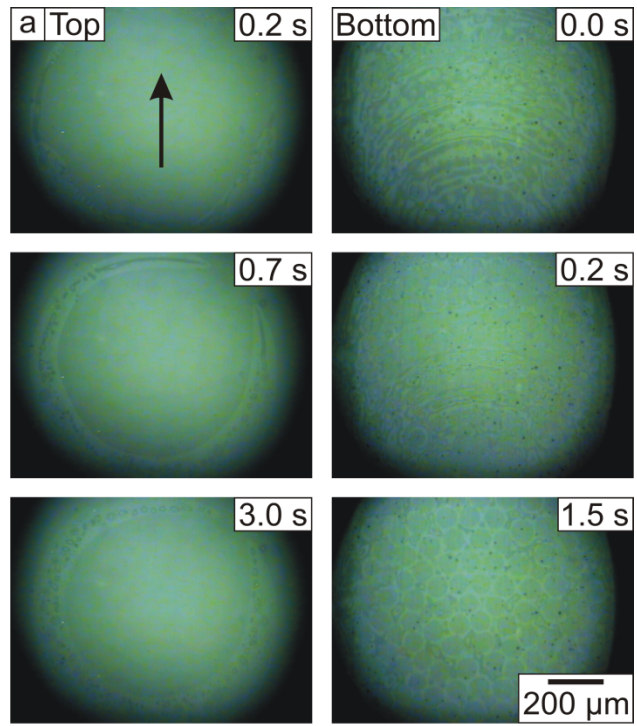
3.3.3 Dynamics of Oil Films During Electrowetting-Driven Droplet Transport

Finally, oil films were examined during electrowetting-driven translational droplet motion using the cartridges with patterned working electrode arrays beneath the dielectric

layers. The droplets were transported by switching off the electrode under the droplet while simultaneously switching on an adjacent electrode. As the droplet spread to wet the newly energized electrode, it briefly became stretched to cover the area of two electrodes, and the top of the droplet was pulled away from the reference surface, as illustrated in Figure 3.4b and shown in frames from a side-view recording of droplet transport in Figure 3.4c. As the droplet returned to a circular shape over the activated electrode, the top of the droplet reapproached the top plate, trapping a dimple of oil between the cartridge surface and the droplet. A ring-shaped region in which the droplet was pressed against the cartridge surface, shown in Figure 3.4a, surrounded the dimple and prevented it from draining into the bulk oil. The ring contained many small, irregularly shaped, and randomly positioned oil lenses.

At the electrowetting surface, as the droplet spread to wet the actuated electrode, concentric waves trailed the receding oil meniscus and transformed into circular oil lenses uniformly distributed over the newly formed film, as shown in Figure 3.4a. The interferographs were not sufficiently well resolved to determine if the film between the lenses became very thin or completely dewetted from the cartridge surface. The lenses remained of constant and uniform size and distribution throughout the film as long as a constant voltage was applied to the same electrode.

Figure 3.4. Top view (a) and side view (b & c) images (a & c) and schematics (b) showing the evolution of the oil films (a & b) and droplet shape (b & c) as a droplet was transported along a path of individual electrodes by electrowetting. When an electrode adjacent to a droplet was switched on, the droplet spread to wet the dielectric layer over that electrode, causing the top of the droplet to be pulled away from the cartridge surface and oil to fill the resulting gap (b & c). As the droplet motion completed, oil became trapped by the droplet reapproaching the cartridge surface, forming a dimple (a, top & b). At the bottom surface covered by the dielectric film, waves formed in the film as the oil meniscus receded and evolved into stable circular oil lenses (a, bottom & b).



3.3.4 *Effects of Voltage Magnitude and Frequency*

Reducing the magnitude of the voltage used to transport droplets allowed the oil films to remain continuously thick at the electrowetting surface. As the voltage decreased, droplet transport and the evolution of the oil film occurred more slowly, and the oil lenses that formed were larger and fewer in number. Table 3.1 lists the approximate droplet transport speeds, film evolution times, and average final oil lens diameters for each voltage level tested from 275 V, near the maximum voltage of the instrument, to 100 V, the minimum voltage at which transport could occur. The films at 225 and 175 V evolved in a similar pattern to the ones at 275 V, described in the previous paragraph. While the stability of the oil films between the lenses remains uncertain, the slower evolution of the films and the larger areas between the larger oil lenses that formed at these voltages allowed clearer observation of the evolution of the film in these spaces. Interference bands appeared between the lenses as they formed, indicating that a continuous oil film connected the lenses. As the lenses evolved to their final shapes and sizes, the interference fringes between them faded and disappeared one by one, indicating that the film was becoming thinner and flatter. When the films became completely flat, the uniform intensity did not allow assessing if the film was very thin or if complete dewetting had occurred. However, there was no observable formation of a triple-contact line. Thus, it seems reasonable to extrapolate that a flat, continuous oil film may also exist between the lenses under high voltage droplet actuation, when the smaller lenses and rapid film evolution made tracking the interference patterns more difficult. At 100 V, the droplets moved slowest, and the dimple at the reference surface was smaller, as shown in Figure 3.5a. Formation of waves at the electrowetting surface was not apparent. Rather,

broad interference bands encircled the center of the film, indicating a continuous film of gradually varying thickness. The film thinned slowly, and the oil drained into a single large lens in the center, as shown in Figure 3.5b. However, the interference patterns persisted throughout the film even after the equilibrium state was reached, indicating that a continuous oil film remained.

Table 3.1. Effect of voltage magnitude and frequency on droplet transport and oil film evolution.

Voltage (V)	Freq. (Hz)	Translational Droplet Speed (mm/s)	Film Evolution Time (s)	Average Oil Lens Diameter (μm)
100	100	1.5	61.0	332
175		2.8	17.4	179
225		4.1	4.7	128
275	10	17.1	2.1	57
	100	17.1	1.4	65
	1000	20.0	1.6	66

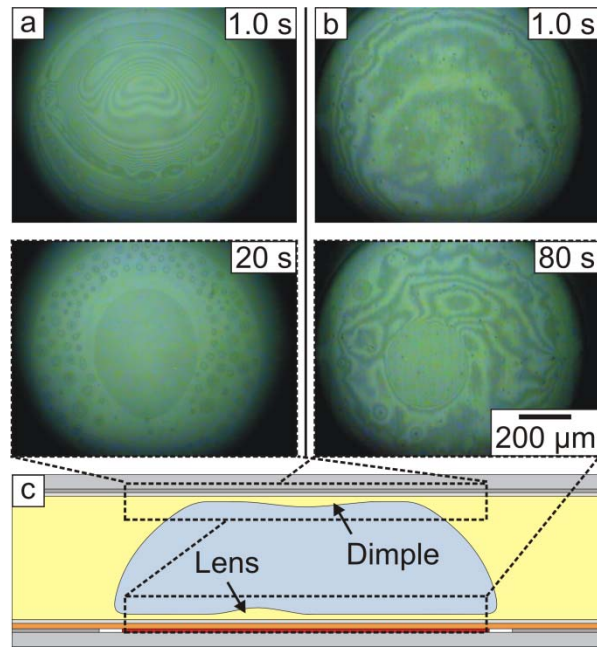


Figure 3.5. Images (a & b) and schematic (c) showing the evolutions of the oil films at the reference (a) and electrowetting (b) surfaces when droplets were transported at 100 V. The droplets moved more slowly at 100 V compared to when transport was actuated using 275 V in all other experiments. (a & c) The dimple that formed at the reference surface was smaller. (b & c) The film thinned more slowly, and only a single large oil lens formed in the film at the electrowetting surface.

While reducing the magnitude of the voltage applied to transport droplets allowed stable oil films to be maintained, reducing the frequency was found to destabilize the films. Films were observed during droplet actuation at 275 V and 10 Hz, 100 Hz, and 1000 Hz. There were no noticeable differences between the films at 100 Hz and 1000 Hz. At 10 Hz, there were also no noticeable differences in the films during droplet transport. However, after the droplets came to rest, they began to vibrate with the frequency of the applied voltage. The vibrations caused the dimple of oil at the reference surface to be squeezed into the oil meniscus, as seen in Figure 3.6a. The oil lenses in the film at the electrowetting surface also began vibrating and merging with each other, forming a percolated network, shown in Figure

3.6b. When the voltage was switched off, the lenses did not drain to reform a planar film. Instead, a contact line with the cartridge surface defined the edges of the lenses and indicated that the film had ruptured between them. The ac frequency was translated into droplet vibrations as the droplet spread to cover more of the dielectric layer at the voltage peaks and relaxed to a smaller diameter when the amplitude was zero.

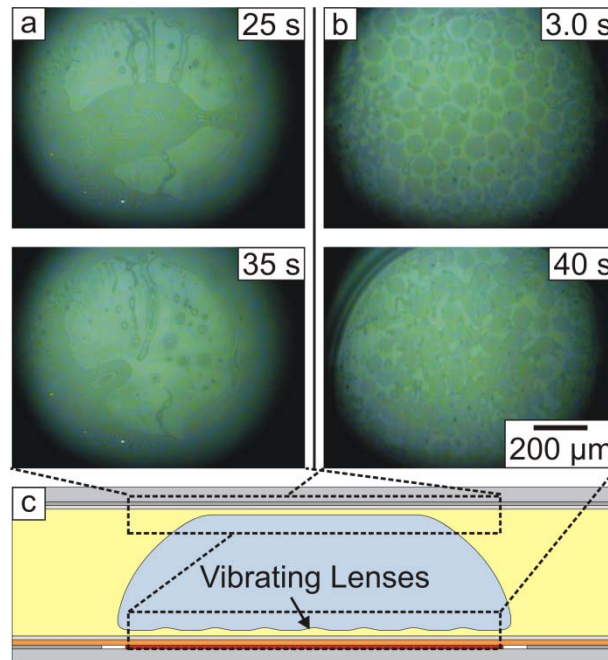


Figure 3.6. Images (a & b) and schematic (c) showing how the evolutions of the oil films at the reference (top) (a) and dielectric-coated (bottom) (b) surfaces changed when a 10 Hz ac voltage was used to transport droplets instead of a standard 100 Hz ac signal. The droplet vibrated with the lower frequency electric field. (a & c) At the top surface, the vibrations caused the dimple in the center of the film to be squeezed out into the oil meniscus. (b & c) At the bottom surface, the oil lenses vibrated and merged with each other, and the film ruptured.

3.3.5 *Effects of Surfactants*

The presence of surfactants in either the droplet phase or the oil phase also affected the stability of the oil films. First, films were examined when Tween-20 was added to the droplets in concentrations ranging from 0.0001% to 10.0% and no surfactant was added to the oil. The formation of the dimple at the reference electrode surface did not appear to be affected by the surfactant. At the electrowetting surface, the period of the waves forming in the film during droplet transport decreased as the concentration of Tween-20 increased, and the oil lenses that subsequently formed were smaller in diameter and more numerous, as listed in Table 3.2. When no surfactant was present in the system or at low Tween-20 concentrations, oil lenses were uniformly distributed up to the edges of the films, as Figure 3.7a shows. When the Tween-20 concentration exceeded 0.01%, the formation of a ring around the perimeter of the film that was void of lenses was observed. As lenses approached this ring, they morphed into streams that drained into the oil meniscus, as seen in Figure 3.7b. When the voltage was switched off, the interference patterns in the films in systems with high surfactant concentration indicated a ring around the edge of the droplet where the film had ruptured separated by a circular contact line from a continuous oil film under the center of the droplet, as Figure 3.7d shows. Such film rupturing behavior was not seen in systems with low surfactant concentration, as Figure 3.7c shows. These observations suggest that the surfactant in the droplet caused the film to rupture at the perimeter of the droplet. Increasing the Tween-20 concentration from 0.1%, close to the critical micelle concentration (CMC), to 10.0% did not significantly affect the film behavior, an expected result since the adsorption of surfactant at the oil-droplet interface reaches a maximum at the CMC. By reducing the

actuation voltage to 100 V, stable oil films could be maintained with droplet Tween-20 concentration as high as 10.0%. Films were also examined in the inverse case when Triton X-15 was added to the oil phase and no surfactant was added to the droplet phase. The Triton X-15 in the oil phase had similar effects on the film as addition of Tween-20 to the droplet phase. Film rupturing at the perimeter of the droplet occurred at lower concentrations of oil phase surfactant, 0.003% Triton X-15, compared to the concentration of Tween-20 in the droplet required to disrupt the films.

Table 3.2. Effect of surfactant concentration on droplet-oil interfacial tension and film behavior.

Concentration	Interfacial Tension (mN/m)	Average Oil Lens Diameter (μm)	State of Film
Tween 20 Added to Droplet Phase			
0.0003%	42.8	92.5	Full of Lenses
0.003%	39.4	50.8	Full of Lenses
0.01%	30.5	25.9	Complete Draining at Perimeter
0.03%	10.9	27.8	Complete Draining at Perimeter
0.1%	6.82	23.7	Complete Draining at Perimeter
1.0%	7.43	21.8	Complete Draining at Perimeter
10.0%		19.5	Complete Draining at Perimeter
Triton X-15 Added to Oil Phase			
0.0001%	30.0	96.3	Full of Lenses
0.0003%		92.6	Full of Lenses
0.001%	26.4	91.4	Full of Lenses
0.003%	30.9	95.9	Complete Draining at Perimeter
0.01%	22.8	86.7	Complete Draining at Perimeter
0.03%	11.4	71.4	Complete Draining at Perimeter
0.1%	8.78	50.0	Complete Draining at Perimeter
0.3%		32.4	Complete Draining at Perimeter
1.0%	8.93	35.4 – too small to measure	Complete Draining at Perimeter

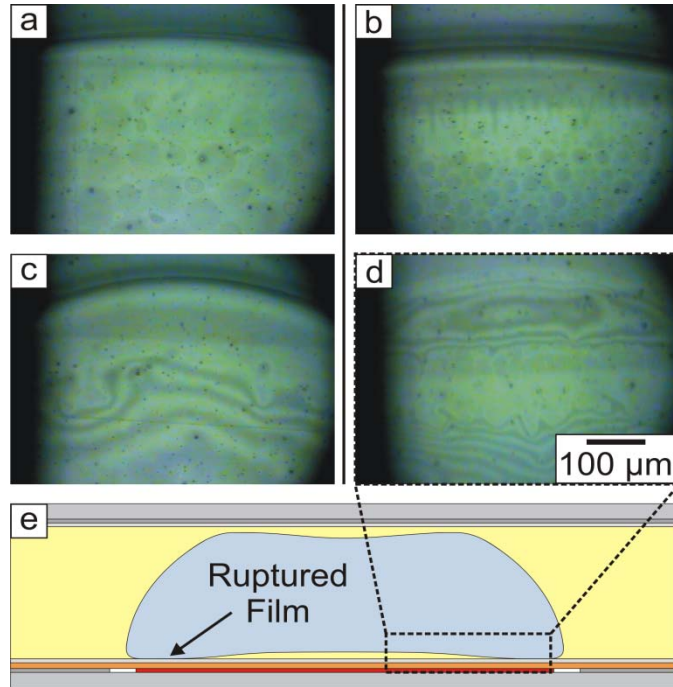


Figure 3.7. Images (a–d) and schematic (e) showing the evolution of the oil film at the electrowetting surface when surfactant (Tween-20) was added to a droplet at concentrations of 0.003% (a & c) and 0.1% (b & d). Images (a) and (b) show the films with voltage applied while images (c) and (d) show the films after the voltage was switched off. (a & c) At low surfactant concentration, lenses were observed all the way to the edge of the film. (b, d & e) At higher concentrations, the film ruptured around the perimeter of the droplet and was not restored when the voltage was switched off, as indicated by lenses streaming into the oil meniscus with the voltage applied and the band around the perimeter of the droplet bordered by a clear contact line instead of continuous interference patterns after the voltage was switched off.

3.4 Discussion

The thermodynamic equilibrium state of the oil wetting film between a water droplet and the microfluidic device surface can be estimated from the spreading parameter

$$S = \gamma_{DW} - \gamma_{DO} - \gamma_{OW} \quad (3.5)$$

where γ_{DW} , γ_{DO} , and γ_{OW} are the device-water, device-oil, and oil-water surface energies. The pendant drop method was used to measure $\gamma_{OW} = 46$ mN/m. The values of $\gamma_{DW} = 46$ mN/m

and $\gamma_{DO} = 3$ mN/m were calculated via Young's equation using values of water and oil contact angles of 112° and 39° and surface energies in air of water, oil, and fluoropolymer of 73 mN/m, 21 mN/m, and 19 mN/m, respectively. Thus, the estimated value of $S = -3$ mN/m was obtained, indicating that the oil should be only partially wetting. The negative value for the estimated spreading parameter suggests that the oil film is thermodynamically unstable or marginally stable. However, kinetic hydrodynamic effects and disjoining pressure also contribute to the film stability.^{24,25}

The kinetic film stability is governed by the balance of the capillary pressure from the curvature of the sides of the droplets and the disjoining pressure between the cartridge surface and the oil-water interface. The capillary pressure is given by eq 1.15. The radius of curvature R at the sides of the droplet, assumed to be $160 \mu\text{m}$ based on a contact angle of 160° and gap height of $300 \mu\text{m}$. Thus, the capillary pressure is 286 Pa. The disjoining pressure is given by eq 1.3 and may include structural, dispersion, and electrostatic components.

Structural forces are typically significant only at length scales of the same order of magnitude as the sizes the molecules in the film. The molecular weight of the PDMS that composes the oil is 410 g/mol, corresponding to an average number of 8 repeat units and approximate contour length of 2 nm.²⁶ Based on the scale of the interference bands from the experiments, the film thickness is expected to range from 10–100 nm. While structural forces may not be important, dispersion and electrostatic forces may both be operative.

The dispersion component of the disjoining pressure can be estimated from eq 1.4. The Hamaker constant for the water-oil-device system can be estimated from the Lifshitz

theory on the basis of the dielectric constant and refractive index of each material²⁷ and was calculated to be 3.33×10^{-22} J using dielectric constants of 80.1, 2.8, and 2.05 and refractive indices of 1.33, 1.39, and 1.34 for water, silicone oil, and the fluoropolymer coating on the device surfaces, respectively. The positive value for the Hamaker constant indicates that the dispersion forces between the film surfaces are attractive and destabilizing. The dispersion contribution to the disjoining pressure for films of thickness 100 – 10 nm can be estimated as 0.018 – 18 Pa.

While the silicone oil is considered nonpolar, accumulation of even a small number of charges at the film surfaces can engender a significant repulsive force. The electrostatic component of the disjoining pressure is given by eq 1.10. The distribution of charges in the film can be determined from the Poisson-Boltzmann equation, given by eqs 1.5 – 1.9 and the solution for which at the film surface can be arranged to relate the surface charge σ to the film thickness h ²⁷

$$\sigma = \frac{-1}{\epsilon\epsilon_0} \left(\frac{2kTK}{ze} \right) \tan \left(\frac{Kh}{2} \right) \quad (3.6)$$

Assuming $T = 298$ K and $z = 1$, a sufficient repulsive pressure to sustain a film thickness of 32.0 – 33.6 nm against a capillary pressure of 286 Pa would be provided by a density of only of one charge per 1.0 – 100 nm². Thus, a small amount of charge at the film interfaces may explain the stable oil films observed with stationary droplets.

A voltage applied across the film to drive electrowetting engenders an electrostatic pressure between the oil-water and dielectric-working electrode interfaces that thins the film. This pressure can be calculated using the equation

$$P_{EW} = \frac{\varepsilon_D \varepsilon_0 V^2}{2d} \quad (3.7)$$

where ε_D and d are the dielectric constant and thickness of the dielectric layer covering the working electrode surface and V is the applied voltage. The destabilizing energy from the applied voltage is only 12 mN/m at 100 V, comparable to the interfacial energies of the system without applied voltage, but much higher, 93 mN/m, at 275 V. The relative magnitudes of the electrowetting energies may partially explain the stable, continuous oil film when electrowetting is driven at 100 V but possible dewetting of the film into lenses at 275 V.

When droplets are transported translationally through a microfluidic cartridge between discrete electrodes by electrowetting, the electrostatic pressure described in the previous paragraph as well as the entrainment of oil from the droplet motion competingly influence the film profile. The effect of the droplet motion on the film is described by the Landau-Levich theory, wherein the thickness of a wetting film behind a receding meniscus increases with the speed of the meniscus according to eqs 3.1 and 3.2. Increasing the applied voltage increases the force moving the droplet but also increases the electrostatic pressure thinning the film. A simple scaling analysis based on existing models of the hydrodynamic and electrical forces on the film can explain the experimental results of stable films when droplets are transported with low voltages but possibly unstable films at high voltages. The following relation between droplet velocity and applied voltage has been derived earlier

$$\frac{\varepsilon_D \varepsilon_0}{2d} (V - V_T)^2 = B \left(\frac{\mu_w U}{\gamma_{ow}} \right) \gamma_{ow} + \left(\frac{mL}{H} + s \right) \mu_o U + \zeta U \quad (3.8)$$

where V_T is the threshold voltage at which the droplet begins to move, μ_W and μ_O are the viscosities of the water and oil, L is the electrode pitch, H is the distance between the two plates composing the device, and B , m , s , and ζ are empirically determined parameters.²⁰ The left side of the equation describes the electrical driving force while the terms on the right side describe the dissipative forces due to flow inside the droplet, oil flow around the droplet, and friction with the device surfaces. The displacement of oil is the dominant force resisting droplet motion, so, assuming that the first and last terms from the right hand side are negligible, $U \sim V^2$. According to eqs 3.1 and 3.2, $h \sim U^{2/3}$, and, thus, $h \sim V^{4/3}$. As eq 3.7 indicates, $P_{EW} \sim V^2$. Therefore, the electrostatic pressure increases faster with voltage than the film thickening effect from the fluid dynamics. At low voltages, the droplet motion may cause the film to thicken, while at high voltages, the electrostatic pressure may become predominant and destabilize the film.

A more detailed theory for film destabilization during electrowetting has been developed by Staicu and Mugele.²² They described entrapment and subsequent spinodal decomposition of oil films after voltage was applied to a sessile droplet above an open surface. The description of the film behavior matches our observations for droplets transported using higher voltages. The experimentally observed trends for the diameters of the oil lenses d_{lens} of $d_{lens} \sim \gamma_{OW}$ and $d_{lens} \sim 1/V$ are consistent with the model for the wavelength of the film instability developed by Staicu and Mugele. At low voltage, however, the results of the earlier sessile droplet experiments and the present droplet transport experiments diverge. In the sessile droplet experiments, the applied voltage was 25 V, and the dielectric thickness was 0.8 μm . In the droplet transport experiments, the lowest applied

voltage was 100 V, and the dielectric thickness was 13 μm . Thus, the electrowetting energy, proportional to V^2/d , was equivalent for both systems. The speed of the receding oil meniscus was different between the two systems. In the sessile droplet experiments, the voltage was ramped from 0 – 25 V gradually to control the rate of droplet spreading, and the maximum speed of the meniscus was approximately 0.6 mm/s. In the droplet transport experiments, the voltage was switched instantaneously from 0 V to 100 V, and the speed of the meniscus was 1.5 mm/s. The higher speed of the meniscus in the droplet transport experiments may have resulted in entrapment of a thicker oil film than in the sessile droplet experiments. The film may have been sufficiently thick that the waves in the free film interface did not cause the film to rupture. While oil films in microfluidic devices operated at high voltage rupture by the mechanism described previously by Staicu and Mugele, that behavior can be avoided by operating devices at low voltage where film thickening from faster droplet transport is the primary effect.

The dimple of oil at the reference electrode surface forms by a different mechanism than the oil lenses in the film at the electrowetting surface. During transport, the droplet is first stretched onto the energized electrode and pulled away from the top plate. The droplet then reapproaches the top plate as it reassumes its original disk shape. The radial flow of oil out of the gap between the droplet and top plate is faster and the pressure normal to the droplet surface engendered by the flow is higher at the perimeter of the droplet than at the center. Thus, the film thins fastest at the perimeter of the droplet. Eventually, the perimeter of the droplet becomes pressed flat against the top plate, trapping the oil above the center of the droplet and completing formation of the dimple. This dimpling behavior has been well

characterized by other researchers studying droplets moving perpendicularly to flat, nondeformable surfaces.²⁵

Surfactants have multiple effects on the oil films. Trace surfactants are expected to be always present as contaminants and residuals of the device and oil manufacturing processes. These molecules result in film thickening during droplet transport by the Marangoni effect as described in Section 3.1. Deliberate addition of surfactant to the droplets or oil suppresses the concentration gradients that lead to film thickening. The added surfactant also produces more deformable fluid interfaces by lowering the interfacial tension, as evidenced by the shorter period for the waves that arise in the film upon droplet transport. The thinner and more deformable nature of the films may also explain why they rupture at the electrowetting surface with surfactants present. When a droplet moves, the film thickens, and when the droplet comes to rest, the film returns to its equilibrium thickness. The pressure gradient-driven dimpling effect described in the previous paragraph is also active as this film thins. The deformable, surfactant-laden droplet interface may respond more noticeably than the surfactant-free interface to the tangential pressure gradient from the flow out of the film, and because the film is thinner with surfactant added, the droplet may rapidly contact the device surface, displacing the oil film in a ring pattern. Minimizing the concentration of surfactant added to the system is desirable for maintaining stable lubricating films.

3.5 Conclusions

The dynamics of oil films lubricating water droplets moving through microfluidic devices have been observed and described with droplet actuation by electrowetting. In the absence of applied voltage, the films may have been stabilized by a small amount of charge adsorbed to the device surface and oil-droplet interface. When voltage was applied, the droplet spread across the electrowetting surface, expanding the area of the film. The effect of electrowetting on the film was determined by competing actions of liquid entrainment from the motion of the receding oil meniscus, which increased with droplet velocity, and electrostatic pressure that thinned the film, which increased with the applied voltage. At low voltage, the electrostatic pressure was small, and the film remained continuous during droplet transport. At high voltage, the electrostatic pressure became dominant, and the film decomposed into an array of oil lenses. Stretching of the droplet during transport followed by a return to a circular shape caused a dimple of oil to be trapped between the droplet and the reference surface of the device. The films were destabilized by vibrations induced by low-frequency voltage and by addition of surfactants to the droplet or the oil. Surfactants always present in the system at trace concentrations are believed to redistribute during droplet transport, setting up interfacial tension gradients that drive oil flow into the film by the Marangoni effect. Adding surfactants at higher concentrations suppressed the surface concentration gradients that engender film thickening and made the oil-droplet interfaces more deformable and susceptible to dimpling and rupture at the droplet perimeter during transport.

The observed film phenomena have important implications for the performance of assays in microfluidic devices in which many droplets travel over the same areas on the surface of the device. The insights from this study can be used to select conditions under which a continuous oil film is maintained to prevent adsorption of molecules to and from the device surfaces. Low voltage should be used to actuate droplet transport to minimize the electrostatic pressure that thins the films and can cause spinodal decomposition. The ac frequency should be on the order of 100 Hz or higher to prevent droplet vibrations that can cause the films to rupture. Although often necessary for assays, addition of surfactants to the droplet or oil phases is undesirable from the perspective of oil film stability. Implementation of surfactants, coatings, or filler fluids that will enhance the wettability of the device surfaces by oil instead of water is an important next step in the development of more robust droplet-based microfluidic devices.

3.6 References

1. Fair, R. B.; Khlystov, A.; Tailor, T. D.; Ivanov, V.; Evans, R. D.; Griffin, P. B.; Srinivasan, V.; Pamula, V. K.; Pollack, M. G.; Zhou, J. *IEEE Des. Test Comput.* **2007**, *24*, 10–24.
2. Pollack, M. G.; Pamula, V. K.; Srinivasan, V.; Eckhardt, A. E. *Expert Rev. Mol. Diagn.* **2011**, *11*, 393–407.
3. Guo, M. T.; Rotem, A.; Heyman, J. A.; Weitz, D. A. *Lab Chip* **2012**, *12*, 2146–2155.
4. Theberge, A. B.; Courtois, F.; Schaerli, Y.; Fischlechner, M.; Abell, C.; Hollfelder, F.; Huck, W. T. S. *Angew. Chem. Int. Ed.* **2010**, *49*, 5846–5868.
5. Srinivasan, V.; Pamula, V. K.; Fair, R. B. *Lab Chip* **2004**, *4*, 310–315.
6. Chatterjee, D.; Shepherd, H.; Garrell, R. L. *Lab Chip* **2009**, *9*, 1219–1229.

7. Link, D. R.; Grasland-Mongrain, E.; Duri, A.; Sarrazin, F.; Cheng, Z.; Cristobal, G.; Marquez, M.; Weitz, D. A. *Angew. Chem. Int. Ed.* **2006**, *45*, 2556–2560.
8. Pollack, M. G.; Fair, R. B.; Shenderov, A. D. *Appl. Phys. Lett.* **2000**, *77*, 1725–1726.
9. Pollack, M. G.; Shenderov, A. D.; Fair, R. B. *Lab Chip* **2002**, *2*, 96–101.
10. Ren, H.; Fair, R. B.; Pollack, M. G.; Shaughnessy, E. J. *Sensor Actuat. B* **2002**, *87*, 201–206.
11. Berthier, J.; Dubois, P.; Clementz, P.; Claustre, P.; Peponnet, C.; Fouillet, Y. *Sensor Actuat. A* **2007**, *134*, 471–479.
12. Landau, L.; Levich, B. *Acta Physicochim. URS* **1942**, *17*, 42–54.
13. Schwartz, L. W.; Princen, H. M.; Kiss, A. D. *J. Fluid Mech.* **1986**, *172*, 259–275.
14. Bretherton, F. P. *J. Fluid Mech.* **1961**, *10*, 166–188.
15. Ruschak, K. J. *Ann. Rev. Fluid Mech.* **1985**, *17*, 65–89.
16. Park, C.-W.; Homsy, G. M. *J. Fluid Mech.* **1984**, *139*, 291–308.
17. Hodges, S. R.; Jensen, O. E.; Rallison, J. M. *J. Fluid Mech.* **2004**, *501*, 279–301.
18. Ratulowski, J.; Chang, H.-C. *J. Fluid Mech.* **1990**, *210*, 303–328.
19. Stebe, K. J.; Barthès-Biesel, D. *J. Fluid Mech.* **1995**, *286*, 25–48.
20. Stebe, K. J.; Lin, S.-Y.; Maldarelli, C. *Phys. Fluids A* **1991**, *3*, 3–20.
21. Quilliet, C.; Berge, B. *Europhys. Lett.* **2002**, *60*, 99–105.
22. Staicu, A.; Mugele, F. *Phys. Rev. Lett.* **2006**, *97*, 167801.
23. Sheludko, A. *Adv. Colloid Interface Sci.* **1967**, *1*, 391–464.
24. Derjaguin, B.; Obuchov, E. *Acta Physicochim. URS* **1936**, *5*, 1.
25. Ivanov, I. B.; Dimitrov, D. S. *Thin Liquid Films*; Dekker: New York, 1988.
26. Gill, R.; Mazhar, M.; Félix, O.; Decher, G. *Angew. Chem.* **2010**, *122*, 6252–6255.
27. Israelachvili, J. N. *Intermolecular and Surface Forces, Second Ed.*; Academic Press: London, 1991.

Chapter 4

Electric-Field-Controlled Flow in Nanoscale-Thin Wetting Films

4.1 Introduction

Nanoscale flow systems are emerging research tools for fields including biochemistry, polymer and colloid science, and even information technology.¹⁻⁴ As discussed in Section 1.4.5, nanofluidic devices may have applications in biological analysis at the single molecule level. Devices may be fabricated using lithography or polymer embossing methods, as explained in Section 1.4.3. However, these techniques for fabricating nanochannels include many delicate processing steps and must be performed in a clean room.

As an alternative to these closed channel nanofluidic devices, which require complex methods for fabrication, a system based on nanoscale-thin wetting films flowing over open surfaces is demonstrated and characterized here. The wetting films flow through two-dimensional channels defined by areas of low and high surface energy. Surface energy patterns have been used to confine liquids between two parallel plates, creating microfluidic channels without side walls,^{5,6} and to control wetting by thin films⁷⁻¹⁰ and spreading of lipid monolayers.¹¹ However, the system described here has several unique aspects that make it more amenable to the applications typically envisioned for nanofluidic devices. The nanofilms reported here are water films, an essential medium for analysis of biomolecules and the most common liquid for systems making use of electrostatic effects, while the liquid in previously reported thin film flow systems was silicone oil.^{7,8} Here, flow in the films is driven by an electric field, while previous researchers have employed temperature⁷ or pressure-gradient-driven flow.^{8,11} Electric-field-driven flow has the advantages of being

readily controllable and reversible and provides a platform for charge-based separations. Models for electroosmotic flow in nanoscale-thin wetting films have been proposed^{12,13} but not demonstrated experimentally as far as the authors are aware. Finally, surface energy patterns are created here by microcontact printing,¹⁴ a simpler method than the photolithography^{7,8,11} or atomic-force-microscopy-based^{9,10} techniques used in previous studies. The following sections describe the construction of the nanoscale-thin wetting film flow system and characterization of its performance on the basis of film thickness, electroosmosis, and electrokinetics.

4.2 Materials and Methods

4.2.1 Flow System Construction

The flow systems were based on mica substrates over which water was transported in thin wetting films between droplets held by capillary forces in chambers on opposite ends of the substrates. Each flow system was constructed immediately before use from a freshly cleaved sheet of grade V1 mica from Ted Pella (Redding, CA), which provided a clean, hydrophilic, and molecularly smooth surface required for nanoscale-thin wetting film formation. After cleaving, the mica surface was rinsed with deionized (DI) water and dried in a stream of air. The droplet chambers were fabricated from PC3L-0.5 CoverWell perfusion chambers from Grace Bio-Labs (Bend, OR). These perfusion chambers consisted of a 600- μm -thick silicone spacer with an adhesive coating on one side and a plastic sheet bonded to the other side. The chambers were cut to create a semicylindrical cavity open on the rectangular face and were attached to the substrate with their open sides facing each other at

a separation of about 1 cm, as illustrated in Figure 4.1. The substrate and chambers were held together in a clamp to avoid using additional liquid adhesives which could contaminate the mica surface. The clamp consisted of one bottom plate large enough to support the mica substrate, and two narrow top plates the width of each of the chambers. The narrow plates were attached to the large plate with screws and pressed the chambers against the mica surface.

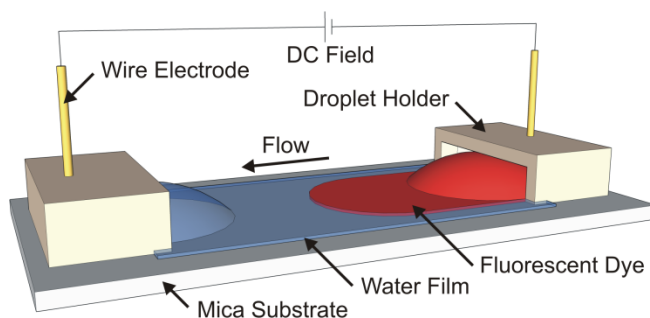


Figure 4.1. Schematic of the nanoscale-thin wetting film flow system. The water film formed spontaneously on the mica substrate in a closed experimental cell at high humidity. Droplets on opposite ends of the substrate provided contact between the film and wire electrodes and supplied fluorescent dye to track the flow in the film induced by a dc voltage applied between the electrodes.

Nanoscale-thin wetting film formation and flow occurred on the open mica surface between the two droplets. Two-dimensional channels restricting the film flow were defined by wettable and nonwettable areas on the surface. Hydrophobic patterns were formed by microcontact printing of an alkane monolayer,¹⁴ while the exposed mica between the monolayers remained hydrophilic. A stamp with depressed features corresponding to the desired channel design was fabricated by soft lithography¹⁵ from a Sylgard 184 silicone elastomer kit from Dow-Corning (Midland, MI) using a 10:1 weight ratio of elastomer base

to curing agent. A solution of 0.1% (v/v) trichlorododecylsilane in hexane, both from Sigma-Aldrich (St. Louis, MO), was spread onto the stamp surface using a cotton swab. Then the stamp, attached to a translation stage to maintain its position to micrometer precision, was pressed against the mica surface for 10 min, as depicted in Figure 1.2. A covalently linked dodecane monolayer was formed at the mica surface in contact with the raised areas on the stamp by reaction of the silane groups with the hydroxyl groups on the mica. After removing the stamp, the surface was rinsed thoroughly with DI water to remove unreacted silane molecules.

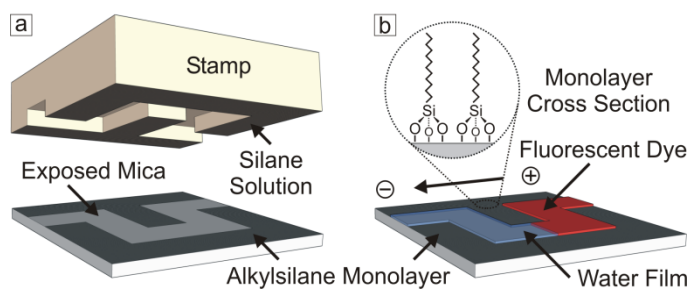


Figure 4.2. Schematic of (a) the creation of two-dimensional channels by microcontact printing and (b) flow through the channels. A dodecylsilane monolayer was deposited where the raised areas of the stamp contacted the mica substrates. The nanoscale wetting film was restricted to the bare mica between the hydrophobic silane patches.

Following the deposition of the channel pattern, the substrate was incubated in a 10 mM solution of NaCl from Alfa Aesar (Ward Hill, MA) in DI water for 1 hour to achieve equilibrium between the surface charges of the mica and the electrolyte solution of the film. After incubation, the droplet chambers were filled with 10 mM NaCl solution. The droplets in some of the experiments also contained a fluorescent dye. To measure the film thickness

based on the fluorescence intensity of the film, 0.1 mg/ml Rhodamine B from Sigma-Aldrich (St. Louis, MO) was added to the solution. Rhodamine B has a low molecular weight and high diffusivity, so it was rapidly transferred into the film. To track the liquid motion in the film, the droplets contained 2.0 mg/ml Texas Red dye conjugated to 10,000 MW dextran from Invitrogen (Carlsbad, CA). The dextran-Texas Red conjugate was selected as an alternative flow marker with the potential to decrease the effects of diffusion and electrophoresis when correlating the motion of the dye to the electroosmotic flow of the film. The molecule has a higher molecular weight than Rhodamine B and is described by the manufacturer as neutral, while Rhodamine B has a positive charge.

The substrate was sealed in a 10 cm diameter by 1 cm tall disk-shaped cell to maintain high humidity conditions necessary for wetting film formation. Inside the cell, the substrate was placed on a platform inclined 2.5° which allowed gentle draining to prevent formation of thick wetting films near saturation humidity. The bottom of the cell around the platform was filled with 10 mM NaCl solution. The cell featured a glass window in the lid for observation of the film by optical microscopy and ports for connecting the flow system to a voltage source. Copper wires were placed in contact with the electrolyte droplets via holes in the tops of the chambers to connect the system to a dc power supply from Extech Instruments (Waltham, MA) (model 382213). Water was spread on the surfaces between the cell and the lid and in the ports for the wires to fill any crevices and prevent dry air from entering the cell, and the lid of the cell was closed tightly with screws. The substrates were incubated in the cells for 1 hr to achieve equilibria in temperature and humidity before any measurements were made.

4.2.2 Characterization of Wetting Films and Flow Behavior

The electrophoretic mobility of the dextran-Texas Red flow marker was measured by a custom-built capillary electrophoresis instrument with a 47 cm long, 50 μm diameter uncoated glass capillary. A photomultiplier detector with laser excitation was positioned 36 cm from the capillary inlet. The detector had a red channel with a 514 nm laser and a 585 nm emission filter and a green channel with a 488 nm laser and a 525 nm emission filter. Prior to use, the capillary was rinsed first with 1.0 M NaOH, then with DI water, and finally with a 10 mM NaCl solution. First, the speed of the electroosmotic flow in the capillary was determined from the time required to replace the 10 mM NaCl solution in the capillary with a 9.5 mM NaCl solution placed in the inlet reservoir at 17 kV applied voltage. The electrical current was observed to decrease linearly as the lower ionic strength solution filled the capillary. The time at which the current reached a stable value, indicating that the electrolyte replacement was complete, was used to calculate the electroosmotic mobility, which was $3.4 \times 10^4 \mu\text{m}^2 \text{V}^{-1} \text{s}^{-1}$. Next, the velocity of the dextran-Texas Red conjugate moving through the capillary was measured. A mixture of 2.0 $\mu\text{g}/\text{ml}$ dextran-Texas Red conjugate and 1.0 nM BODIPY FL, another neutral marker, was loaded into the capillary inlet. The Texas Red was detected via the red channel and the BODIPY was detected via the green channel. The mobility of the BODIPY was equal to the electroosmotic mobility of the liquid in the capillary, indicating that the BODIPY was charge neutral. The times required for the dyes to reach the detector were used to calculate the apparent mobilities of 5.7×10^4 and $3.5 \times 10^4 \mu\text{m}^2 \text{V}^{-1} \text{s}^{-1}$ for the dextran-Texas Red conjugate and BODIPY, respectively. The

electrophoretic mobility of the dextran-Texas Red molecule was the difference between the observed mobility and the electroosmotic mobility, or $2.2 \times 10^4 \mu\text{m}^2 \text{V}^{-1} \text{s}^{-1}$.

The wetting films were characterized by interference microscopy and fluorescence microscopy using an Olympus BX-61 microscope (Tokyo, Japan) in reflected light mode. The cell containing the flow system was placed on the microscope stage, and the film was observed through the glass window in the top of the cell. A 550 nm filter was placed in the illuminating light path to provide monochromatic light for interference microscopy. A 41002a filter set from Chroma Technology (Bellows Falls, VT) was used for fluorescence microscopy. Images of the films were recorded with an Olympus DP70 CCD camera.

4.3 Results

4.3.1 Initial Demonstration of Wetting Film Formation and Flow

The nanoscale-thin film flow system was characterized on the basis of wetting behavior and flow performance using interference and fluorescence microscopy. First, qualitative observations confirmed the formation of a thin wetting film and the capability of inducing flow by application of an electric field. Examination of the droplet menisci provided evidence for a wetting film on the mica rather than a dry substrate. An example of the interference fringes appearing at the edge of a droplet is shown in Figure 4.3a. Each fringe in the interference pattern corresponded to a 207 nm change in liquid height. The interference fringes broadened at the edge of the meniscus, indicating curvature consistent with a transition to a thin wetting film instead of a liquid-solid contact line at the edge of the droplet. Fluorescence of uniform intensity, as shown on the right side of Figure 4.3b, was

observed farther away from the edge of the droplet than the interference fringes, supporting the existence of a uniform wetting film into which the dye diffused during the incubation period.

The fluorescence and interference microscopy characterization of the system in the areas where the substrates were patterned with two-dimensional channels also provided information about the thin wetting film. A sharp drop in the fluorescence intensity was observed where the film met the edges of the dodecane monolayers. Extending from this boundary, a fluorescence pattern matching the channel pattern appeared. Figures 4.3c and 4.3d show the same substrate area in brightfield and fluorescence microscopy modes, respectively. No interference fringes were observed in the brightfield micrograph along the edges of the patterned hydrophobic areas (Figure 4.3c). However, the “channels” were clearly distinguishable in the fluorescence micrographs, proving that both the water film on the mica and the silane layers were very thin. Flow in the 2D channel was tracked by a change in position of the dye front, shown in Figure 4.3d. Application of an electric field between the liquid droplets caused the dye to continue to move along the channel at a speed an order of magnitude faster than molecular diffusion. Reversing the polarity of the dc field caused the direction of the flow to reverse and the fluorescence front to recede.

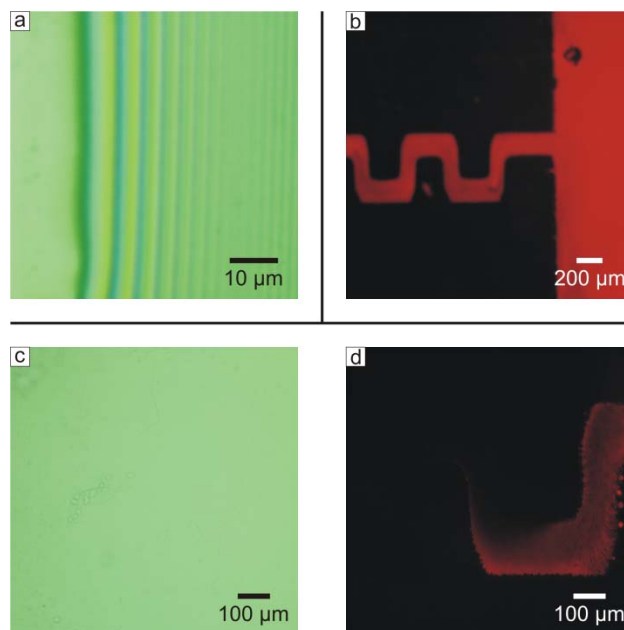


Figure 4.3. Brightfield (a and c) and fluorescence (b and d) micrographs showing (a) interference fringes indicating the transition between a droplet and a thin film and (b-d) a thin film containing dye flowing through a two-dimensional channel. Images (c) and (d) were taken at the same area of the substrate in both illumination modes, but both the film and the hydrophobic monolayer are too thin to be seen in brightfield microscopy mode (c).

4.3.2 Measurement of Film Thickness

After confirming the formation of wetting films on the mica substrates, quantitative measurements of film thickness were performed. Two alternative approaches based on interference microscopy and fluorescence microscopy, respectively, were used to estimate the film thickness. Images of interference patterns were processed to measure the reflected light intensity along the transitions from droplets to films, as exemplified in Figure 4.4. The area of uniform intensity on the right side of the inset image corresponds to the thin film, while the alternating dark and bright bands on the left side of the image indicate the gradually decreasing thickness of the droplet meniscus. The thickness of the film can be calculated from the equation

$$h = \frac{\lambda}{2\pi n_f} \left(l\pi \pm \arcsin \sqrt{\Delta I} \right) \quad (4.1)$$

where

$$\Delta I = \frac{I_{max} - I}{I_{max} - I_{min}}, \quad (4.2)$$

λ is the wavelength of light, here 550 nm, n_f is the refractive index of the film, l is the order of interference, and I is the intensity of light measured at any point between the intensity maxima, I_{max} , and minima, I_{min} , of the interference bands.¹⁶

For the purpose of estimating the film thickness, the intensity value of the zeroth order interference minima, the dark band nearest to the thin film, was used for I_{min} . Likewise, I_{max} was taken to be the value of the zeroth order interference maxima, the intensity corresponding to an infinitely thin film. Absent a film of thickness approaching zero in this system from which to measure I_{max} directly, its value was determined from higher order interference extrema. This calculation was complicated by the decrease of the intensity of the fringes as the order of interference increased. The probability of interference between reflections off of the air-water interface and the substrate from the same wave decreases as the film thickness increases, as interference between two different waves does not occur if the waves are incoherent. The value of I_{max} was extrapolated from the best fit of $|I_{ext} - I_{avg}|$ and x for all of the clearly distinguishable intensity extrema I_{ext} . The average intensity, I_{avg} , is indicated by the short-dashed line in Figure 4.4, and x is the position along the meniscus perpendicular to the interference fringes. Data from images of six different films were fitted to a cubic function, the simplest type of equation which matched the trend of the data. The

estimate of I_{max} is represented by the top long-dashed line in Figure 4.4. Using the value of the average intensity of the uniform film for I along with eqs 4.1 and 4.2, an estimate of $h = 35.0 \pm 7.3$ nm was obtained for the film thickness.

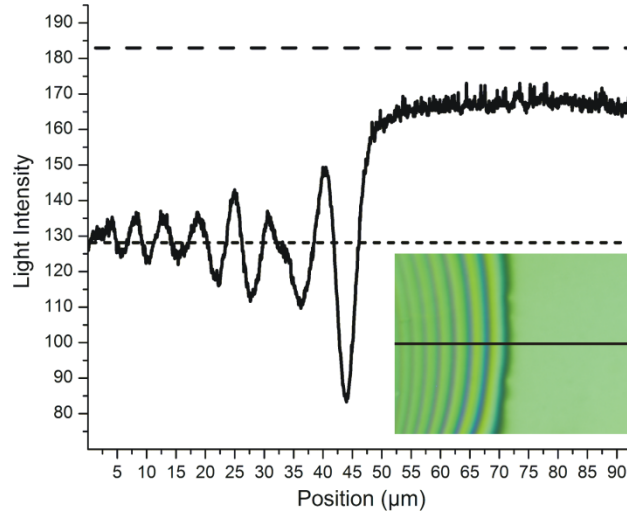


Figure 4.4. Plot of the light intensity from an image (inset) of an interference pattern at the transition from a droplet to a thin film presumed to be in the zeroth order of interference. The height of the liquid changed by 207 nm over one intensity wavelength. The film thickness was estimated from the value of the uniform light intensity of the film on the right side of the plot relative to the fitted trend for the position of the intensity minima and maxima of the interference fringes.

The second method for quantifying the film thickness was based on the measured intensity of a known concentration of fluorescent dye in the film. A simple calibration curve,

$$h = \frac{I - I_{bg}}{a}, \quad (4.3)$$

was established for determining the film thickness h from the fluorescence intensity I . I_{bg} was the background fluorescence of the system. The value of the parameter a was determined by uniformly spreading 10 μ l of varying concentrations of dye solution over 1 cm^2 areas

constrained by patterned dodecane monolayers on a mica substrate and measuring the intensities of the resulting 10 μm thick films. The concentrations of the solutions were chosen so that the total amount of dye per unit area in the films equaled the amount of dye in 15 – 200 nm thick films containing 0.1 mg/ml Rhodamine B solution. Then, flow systems were assembled with 0.1 mg/ml Rhodamine B solution in the droplet chambers and a pattern of parallel, straight channels on the substrate. During the incubation period, the dye diffused into the thin film between the droplets, producing areas of uniform fluorescence matching the channel pattern, similar to the systems shown in Figure 4.3. The intensities of the dye in the channels and the surface between the channels were measured to determine I and I_{bg} , respectively. By using eq 4.3, the film thickness was estimated to be $h = 21.9 \pm 11.4$ nm.

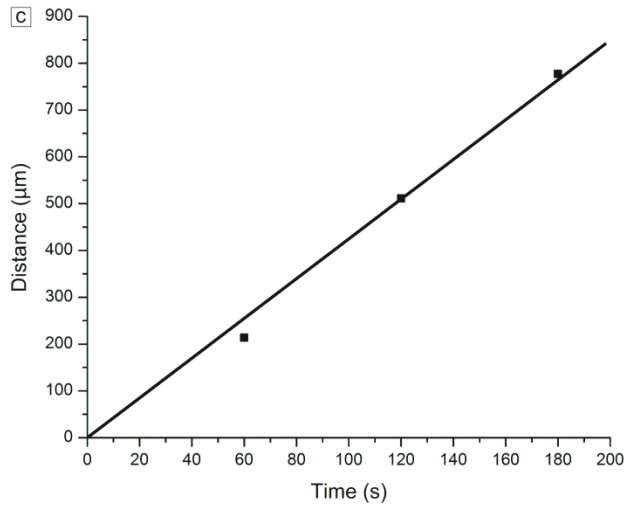
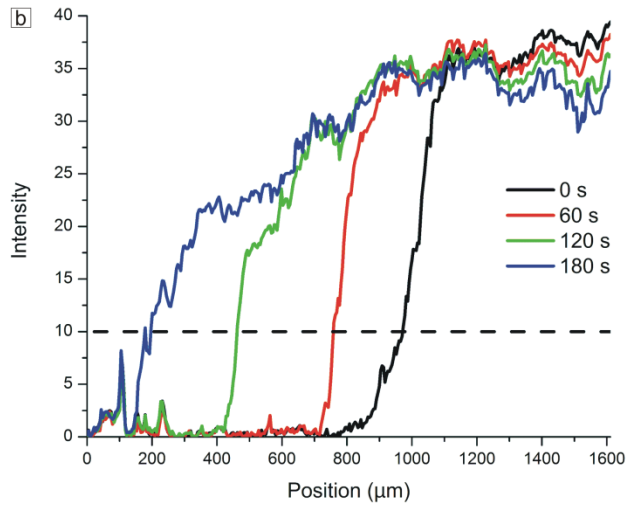
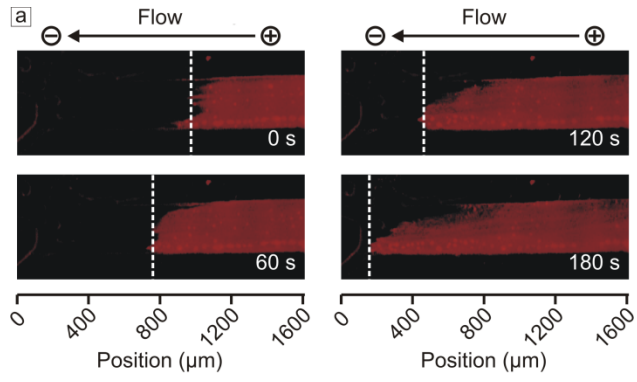
4.3.3 Measurement of Electroosmotic Mobility

In addition to the film thickness, the velocity of the flow in the film was also measured. The substrates for these experiments were patterned with a set of parallel straight channels between the two droplets containing the dextran-Texas Red fluorescent flow marker. The width and pitch of the channels was 300 μm . Application of a dc electric field across a solution can cause liquid flow by electroosmosis and transport of charged molecules or particles by electrophoresis. The field-induced flow or molecular motion can be characterized by the mobility μ , given by eq 1.16. In the thin film flow system, the observed mobility of the flow marker is the sum of the electroosmotic mobility of the liquid and the electrophoretic mobility of the molecule and is given by the equation

$$\frac{U_{Obs}}{E} = \mu_{Obs} = \mu_{EO} + \mu_{EP} = \frac{U_{EO} + U_{EP}}{E} \quad (4.4)$$

The electrophoretic mobility of the dextran-Texas Red conjugate marker was determined by capillary electrophoresis as described in Section 4.2.2. The marker had a slightly positive charge with a mobility of $2.2 \times 10^4 \mu\text{m}^2 \text{V}^{-1} \text{s}^{-1}$. To characterize the mobility of the thin wetting film, the propagation rate of the flow marker was measured in several experiments at different voltages applied across the film. The marker speed was measured from periodically recorded fluorescence microscopy images of a fixed area on a substrate while a set of constant dc fields was applied between the droplets. At each time point, the position along the length of a channel where the average fluorescence intensity across the width of the channel reached a threshold value was recorded, as depicted in Figures 4.5a and 4.5b. A linear regression was performed on the position and time data to determine the speed of the flow marker for each experiment, as illustrated in Figure 4.5c.

Figure 4.5. Example of (a) fluorescence micrographs and (b and c) plots used to estimate the velocity of marker motion in the wetting film. (a) In a dc field, fluorescent dye was observed to travel from the droplet at the cathode, into the film, and toward the droplet at the anode. (b) The fluorescence intensity along a two-dimensional channel was plotted at regular time intervals. The positions at which the fluorescence intensities reached a threshold value are indicated by the dashed lines. (c) The plotted slope of these positions versus time yielded the speed of the film.



For each experiment, the flow velocity was measured first with 5 V applied between the droplets. Then, the applied voltage was changed to another value ranging from 2.5 V to 15 V, and the speed was measured again. The applied voltage was divided by the measured distance of separation between the two droplets to determine the electric field strength. The first measurement of the speed in each experiment at the same applied voltage provided a basis for comparing the speeds of flows at different electric field strengths on different mica substrates, which may be subject to some variation in surface charge. Thus, the second speed for each experiment was normalized using the equation

$$U_{2,norm} = \frac{U_1}{U_{1,avg}} U_2 \quad (4.5)$$

where U_1 and U_2 are the first and second speed measurements for each experiment and $U_{1,avg}$ is the average of the first speed measurements for all the experiments. The normalized velocity data are plotted in Figure 4.6. The resulting aggregate mobility of the fluid and the marker in the thin film flow system is the slope of the line through the speed and electric field data, which was determined to be $2.8 \times 10^3 \pm 0.9 \times 10^3 \mu\text{m}^2 \text{V}^{-1} \text{s}^{-1}$.

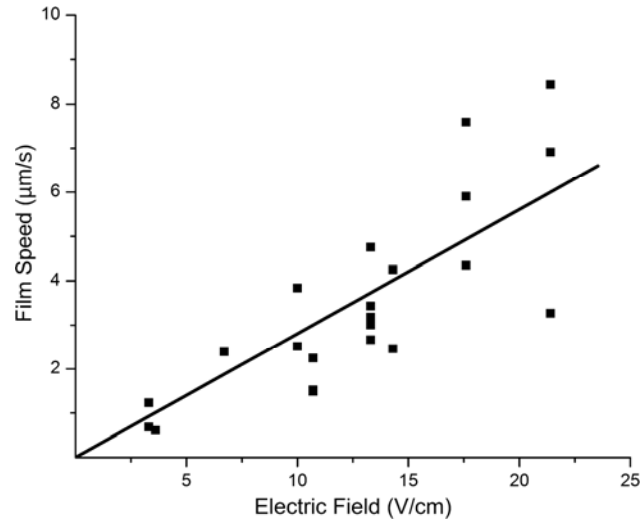


Figure 4.6. Plot of film electroosmotic mobility versus electric field strength for the nanoscale-thin film flow system. Each point represents an experiment of the type depicted in Figure 4.5. The slope of the line through the data is the aggregate electroosmotic mobility of the fluid and the flow marker.

4.4 Discussion

The thickness of the wetting film is determined by the balance between the disjoining pressure and the capillary pressure, as illustrated in Figure 4.7 and discussed in Section 1.2. On this basis, the film thickness was predicted from theory by first calculating the capillary pressure and equating that value to the disjoining pressure to calculate the corresponding film thickness.

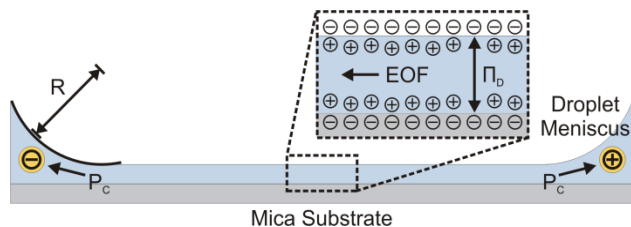


Figure 4.7. Schematic of the physical principles of film formation and electroosmotic flow (EOF). The film is supported by the disjoining pressure, Π_D , which arises from repulsion between charges at the air-water interface and the mica surface. The capillary pressure, P_C , at the droplet menisci of radius of curvature R drains and thins the film. EOF occurs when the positive counterions at the mica surface are attracted toward a negatively charged electrode and drag the film liquid in the same direction.

The capillary pressure was calculated using eq 1.15. The radius R was evaluated from the interference images by measuring the position of each clearly resolved interference extrema, where the height of the meniscus was unambiguously known, and fitting those points to a circle by minimizing the sum of the squared deviations. The capillary pressure of the meniscus was thus estimated to be $P_C = 110$ Pa.

In aqueous systems, the disjoining pressure is dominated by electrostatic repulsion, which depends on the surface potentials of the air-water interface and the mica. The potential gradients are described by the Poisson-Boltzmann equation, which cannot be solved analytically for the case of parallel planes with dissimilar surface potentials. A simple but likely accurate calculation of the disjoining pressure of the film was performed using an equation for the interaction energy between parallel planes of dissimilar surface potential developed by Ohshima et al.¹⁷ and based on a power series expansion to a third approximation for the potential. The equation was differentiated with respect to the distance separating the planes to calculate the force of repulsion between them, which is equivalent to

the disjoining pressure. Mica is a naturally occurring mineral, and the proportions of its constituent Si, Al, Fe, Mg, Na, and K atoms can vary, making the surface potential difficult to know *a priori*.¹⁸ In the calculation, the surface potential of mica ranged from -130 mV to -60 mV as reported in the literature.¹⁸ Similarly, a range of -65 mV to -35 mV was used for the surface potential of the air-water interface because its nonrigid nature makes this value difficult to measure experimentally.¹⁹⁻²¹ With these values for the potentials at the interfaces, the value for the distance separating the surfaces was varied until the calculated disjoining pressure equaled the capillary pressure. Thus, the film was theoretically predicted to be between 23.8 and 27.7 nm thick.

The repulsion forces between parallel planes of different dissimilar potentials can also be obtained by using exact solutions of the Poisson-Boltzmann equation that have earlier been calculated numerically and compiled into a table.²² The available tabulated data includes results for surface potentials and disjoining pressures close to but not exactly equal to the values for the thin film flow system. The surface potential pair listed in the table that most closely matches the mica-water and air-water interfaces is -103 mV and -46 mV. For these potentials and disjoining pressures of 63 Pa and 171 Pa, which are above and below the value of 110 Pa estimated for the wetting films, surface separation distances of 24.3 nm and 27.4 nm are given. These distances are within the range of film thicknesses calculated using the Poisson-Boltzmann approximation, confirming the results of that calculation. The film thickness calculated from theory falls between the film thicknesses measured experimentally by fluorescence microscopy and interference microscopy. Error in the interference-based measurement may have resulted from an overevaluation of the maximum light intensity

extrapolated to zero thickness. All experimental and theoretical evidence taken together suggests that the thicknesses of the films in the nanoscale-thin film flow system are most likely to be within the 20 – 35 nm range.

The observed mobility of the dextran-Texas Red flow marker in the film can arise from molecular diffusion or electrophoresis of the flow marker through the film or from electroosmotic transport of the liquid. The data in Figure 4.6 indicate no measureable collective diffusion at 0 V/cm, and, thus, transport of the dye appears to be influenced only by electrokinetics effects. The potential contribution of diffusion to the overall transport of the flow marker can be evaluated theoretically by first calculating the diffusivity of the dextran molecule using the Einstein-Stokes equation,

$$D = \frac{kT}{6\pi\eta R_h}, \quad (4.6)$$

where k is the Boltzmann constant, η is the viscosity of the liquid media, T is the temperature, and R_h is the hydrodynamic radius of the molecule. The value of $R_h = 3$ nm reported for 9,000 MW dextrans²³ results in a diffusivity estimate of $81 \mu\text{m}^2 \text{s}^{-1}$. The average displacement of a molecule by diffusion over time t can be calculated by the relationship $r = \sqrt{2Dt}$. The dextran velocity of diffusion was predicted to be $0.94 \mu\text{m/s}$ over 180 s, the time scale of the experiment. This estimated diffusion is comparable to the measured mobility at low fields (≈ 3 V/cm). The reasons for the much smaller actual diffusion transport of the dye include possible adsorption and friction of the molecular species in the film, as discussed further in the text.

The relative importance of electrophoresis and electroosmosis to the flow marker motion were evaluated next. The expected electroosmotic mobility of water adjacent to a mica surface was calculated using eq 1.17. Assuming a value of -72 mV^{24} for the zeta potential of the mica substrate yields an electroosmotic mobility of $5.7 \times 10^4 \text{ } \mu\text{m}^2 \text{ V}^{-1} \text{ s}^{-1}$, which is nearly three times higher than the measured electrophoretic mobility of the flow marker ($2.2 \times 10^4 \text{ } \mu\text{m}^2 \text{ V}^{-1} \text{ s}^{-1}$). Following eq 4.4, the combined electrophoretic and electroosmotic mobilities of the marker and fluid add to an effective mobility of $7.9 \times 10^4 \text{ } \mu\text{m}^2 \text{ V}^{-1} \text{ s}^{-1}$. This estimate is one order of magnitude larger than the experimentally measured value.

The reason for the much lower experimentally measured mobility of the fluid together with the marker in the nanofilm than the one estimated above on the basis of the bulk electrokinetics theory has yet to be clarified in depth. Electrokinetic phenomena depend on the dielectric permittivity and viscosity of the liquid media and the surface charge of particles or channel walls, as shown by eq 1.17. The properties of water are well known and not likely to be different in the film, but the zeta potential of mica has not been highly accurately characterized. By rearranging eq 1.17, the zeta potential corresponding to the experimental electroosmotic mobility was calculated to be -3.6 mV (neglecting for simplicity the secondary effect of electrophoresis). The zeta potential is the electrical potential of the shear plane in the liquid at the idealized boundary between ions which move with the liquid and immobile ions adjacent to the solid surface. Using the Guoy-Chapman model of the counterion layer, the potential Ψ at any distance x from the surface can be calculated from the equation

$$\Psi = \frac{4kT}{e} \gamma e^{-\kappa x}. \quad (4.7)$$

For the literature values of $\zeta = -72$ mV and the corresponding surface potential $\Psi_s = -100$ mV, the plane of slip would be situated 0.21 nm from the mica surface, while for $\zeta = -3.6$ mV, the plane of slip should be positioned 9.7 nm away from the mica surface. A possible reason for such a large shift in the plane of slip is penetration of water into the mica surface, forming a thick gel-like hydration layer where ion and dextran mobilities are inhibited. However, previous researchers have argued that mica behaves more like a solid, impenetrable surface and a hydration layer could only exist at subnanometer thickness.²⁵ A more likely scenario is that the molecules of the fluorescently labeled dextran marker used to track the flow of the film were slowed down by friction in the nanoscale thin film and/or adsorption on the mica surface. Such behavior has been reported as the reason for reduced mobilities of other polymers and proteins in microscale systems^{26–28} and is consistent with the independently observed suppressed molecular diffusion of the marker. Overall, the data prove that the mobility of the fluid and dextrans in the nanofilm under the action of the electric field is easily initiated, measured, and reproduced. Thus, the results demonstrate a means to controllably transport molecular species in a nanoscale confined liquid.

4.5 Conclusions

A novel nanofluidic system based on electroosmotic flow in patterned nanoscale-thin wetting films has been demonstrated and characterized. The films were confined laterally in two-dimensional channels by microcontact printing of alkylsilane monolayers, creating nonwetting areas on the substrates. The thicknesses of the films were estimated to be below a

few tens of nanometers from interferometry and fluorescence intensity measurements. The velocity of the fluorescent species in the film was determined to increase linearly with the magnitude of the applied dc field, consistent with electroosmotic fluid and electrophoretic molecular transport. However, the combined mobility of the molecules and fluid was measured to be an order of magnitude lower than the theoretical estimate, likely because of adsorption of the molecular flow markers to the mica surface. Indeed, the most significant challenge in this investigation was to measure the characteristics of such a thin film without changing its properties. On the other hand, the information gathered from such systems may aid in the future characterization of nanofluidic processes.

The primary advantage of the nanoscale-thin wetting film flow system concept is the simplicity of fabrication compared to the more typical closed channel systems of similar dimensions. Once the template for the two-dimensional channel pattern was produced, no complex lithography or clean room procedures were required, and the devices were constructed in minutes from inexpensive materials. The open surface of this flow system makes it analogous to a nanoscale conveyor belt rather than a nanoscale pipe and permits the use of analytical techniques, such as scanning probe microscopy, that are not compatible with closed channel systems. This concept may provide a basis for a readily accessible platform for analysis of individual molecules.

4.6 References

1. Eijkel, J. C. T.; van den Berg, A. *Microfluid. Nanofluid.* **2005**, *1*, 249–267.
2. Abgrall, P.; Nguyen, N. T. *Anal. Chem.* **2008**, *80*, 2326–2341.

3. Prakash, S.; Piruska, A.; Gatimu, E. N.; Bohn, P. W.; Sweedler, J. V.; Shannon, M. A. *IEEE Sens. J.* **2008**, *8*, 441–450.
4. Sparreboom W.; van den Berg, A.; Eijkel, J. C. T. *Nat. Nanotechnol.* **2009**, *4*, 713–720.
5. Zhao, B.; Moore, J. S.; Beebe, D. J. *Science* **2001**, *291*, 1023–1026.
6. Lam, P.; Wynne, K. J.; Wnek, G. E. *Langmuir* **2002**, *18*, 948–951.
7. Kataoka, D. E.; Troian, S. M. *Nature* **1999**, *402*, 794–797.
8. Darhuber, A. A.; Troian, S. M.; Reisner, W. W. *Phys. Rev. E* **2001**, **64**, 031603.
9. Fukuzawa, K.; Deguchi, T.; Kawamura, J.; Mitsuya, Y.; Muramatsu, T.; Zhang, H. *Appl. Phys. Lett.* **2005**, *87*, 203108
10. Checco, A.; Gang, O.; Ocko, B. M. *Phys. Rev. Lett.* **2006**, *96*, 056104.
11. Czolkos, I.; Erkan, Y.; Dommersnes, P.; Jesorka, A.; Orwar, O. *Nano Lett.* **2007**, *7*, 1980–1984.
12. Petrov, A. G.; Smorodin, V. Y. *PMM-J. Appl. Math. Mech.* **1993**, *57*, 577–581.
13. Joo, S. W. *Microfluid. Nanofluid.* **2008**, *5*, 417–423.
14. Kumar, A.; Biebuyck, H. A.; Whitesides, G. M. *Langmuir* **1994**, *10*, 1498–1511.
15. Xia, Y.; Whitesides, G. M. *Annu. Rev. Mater. Sci.* **1998**, *28*, 153–184.
16. Sheludko, A. *Advan. Colloid Interface Sci.* **1967**, *1*, 391–464.
17. Ohshima, H.; Healy, T. W.; White, L. R. *J. Colloid. Interf. Sci.* **1982**, *89*, 484–493.
18. Israelachvili, J. N. *J. Chem. Soc. Farad. T.* **1978**, *74*, 975–1001.
19. Takahashi, M. *J. Phys. Chem. B* **2005**, *109*, 21858–21864.
20. Creux, P.; Lachaise, J.; Graciaa, A.; Beattie, J. K. *J. Phys. Chem. C* **2007**, *111*, 3753–3755.
21. Yaminsky, V. V.; Ohnishi, S.; Vogler, E. A.; Horn, R. G. *Langmuir* **2010**, *26*, 8061–8074.
22. Devereux, O. F.; de Bruyn, P. L. *Interaction of Plane-Parallel Double Layers*; The M.I.T. Press: Cambridge, 1963.

23. Ioan, C. A.; Aberle, T.; Burchard, W. *Macromolecules* **2000**, *33*, 5730–5739.
24. Scales, P. J.; Grieser, F.; Healy, T. W. *Langmuir* **1990**, *6*, 582–589.
25. Israelachvili, J. N. *J. Colloid. Interf. Sci.* **1985**, *110*, 263–271.
26. Stuart, M. A. C.; Mulder, J. W. *Colloid Surface* **1985**, *15*, 49–55.
27. Zembala, M.; Adamczyk, Z. *Langmuir* **2000**, *16*, 1593–1601.
28. Norde, W.; Rouwendal, E. *J. Colloid. Interf. Sci.* **1990**, *139*, 169–176.

Chapter 5

Summary and Outlook

5.1 Summary

This dissertation describes how electric fields may be used to control the shape of and flow in thin wetting films, which play important roles in coating, lubrication, and microfluidics. Results from three projects are included. In the first project, the electrowetting effect was used to control the length of the micrometer-thick films in which colloidal crystal coatings of polymer microspheres were formed by convective assembly. An electroconvective coating apparatus was constructed where the particle suspension was pinned at the intersection of a moving top plate and a substrate and two electrodes in contact with the suspension and beneath the substrate were introduced. The coatings formed in the wetting film that extended from the meniscus of the suspension while dragging the top plate and simultaneously applying voltage between the electrodes. Both the rate of deposition and the size of the crystal domains in the coatings were found to depend on the length of the film. By applying voltage to extend the film, the surface area of the wetting film available for evaporation was enlarged, accelerating the flux of particles from the bulk suspension to the film and the rate of crystal growth. The longer film also increased the time available for particles to rearrange and conform to the ideal packing structure, resulting in formation of colloidal crystal coatings with fewer defects. A model based on a combination of mass balance, fluid flow, and electrowetting was developed and showed a good agreement with the experimental data.

In the second project, the evolution and stability of oil films in electrowetting-actuated microfluidic devices were examined. The system consisted of nanoliter water droplets confined in a thin, oil-filled gap over an array of electrodes. A thin layer of oil separated the droplets from the device surfaces. The oil films lubricated the droplet motion and prevented adsorption of molecules from the droplet to the device surfaces. By sequentially switching the voltage along the electrode array, droplets could be transported in two dimensions around the device. The oil films were observed to transition from micrometer to nanometer thickness when voltage was applied. At low voltages, the films thinned slowly, while at high voltages the films dewetted into arrays of droplets as the electrostatic pressure on the film overcame the film thickening engendered during transport by the inelasticity of the droplet surface. Vibrations from low frequency electric fields and addition of surfactants to the droplets or the oil phase also destabilized the films.

In the third project, electroosmotic flows in nanoscale-thin wetting films of water were demonstrated. The films formed on highly hydrophilic and molecularly smooth mica surfaces in a saturation humidity environment. The thickness of the films was determined to be tens of nanometers using interference and fluorescence microscopy. Flow was initiated by applying voltage between electrodes in contact with droplets at opposite sides of the film and tracked with a fluorescent dye. The relationship between the applied voltage and the flow rate was determined to be linear and consistent with the theory of electroosmosis. Microcontact printing of hydrophobic silane monolayers on the substrates was used to confine the film to two-dimensions to create virtual channels. The results could find applications in innovative bio-nanofluidic lab-on-a-chip devices.

5.2 Outlook

Wetting films are integral to many important industrial processes, not the least of which is application of coatings. Evaporation from a solvent is a primary mechanism by which the materials that form coatings are deposited, and the characteristics of the liquid film directly affect the final state of the coating.¹ As demonstrated through the coating assembly project described in Chapter 2, electric fields may be used to efficiently tune coating processes by providing control over the shape of the wetting film. The convective assembly method in general is highly versatile, having been demonstrated with particles ranging from gold nanoparticles of 12 nm in diameter² to live cells and microspheres of 10 μm in diameter.³ In addition to controlling the film spreading, the electric field may find dual use in directing the alignment of the constituent particles.⁴ More broadly, the method developed through this research may be useful in any evaporation-driven process affected by liquid shape, but may be most applicable for high-value coatings and assemblies for which the added complexity of introducing the electric field would be justified by the gain in control of the micro- or nanostructure of the material.

Another industrially important process in which wetting films are critical is lubrication. The effect of electric fields on lubricating films has been explored in Chapter 3 for the case of droplet-based microfluidic devices. While microfluidic devices may not be a traditional example of a lubrication problem, friction is certainly an issue in these systems because the surface area to volume ratio for the moving liquids is high. The microfluidics technology is rapidly becoming commercialized by an assortment of new enterprises, such as Advanced Liquid Logic, Fluidigm, and Raindance Technologies, and adopted by well-

established firms including Agilent, Abbot, and PerkinElmer, among many others. The knowledge gained through this research will be immediately applicable in designing lab-on-a-chip devices with reduced inter-assay contamination and may serve as a starting point for investigating lubricating films in other system in which electric fields are present. While the work in this dissertation is focused primarily on the effects of electric fields on film stability, extending the research to evaluate also films of electrorheological fluids⁵ could enable the development of devices in which the lubrication is tuned by the electric field.

Nanoscale-thin wetting films may provide a foundation for new research tools in nanotechnology. The electroosmotically driven aqueous wetting film flow system described in Chapter 4 features film thicknesses of a few tens of nanometers, approaching the dimensions of macromolecules and biomolecules. Thus, thin films may provide an elegant means by which individual molecules may be isolated without requiring complex processing to fabricate nanoscale structures, while electric fields may be used to drive liquid flow and transport or align molecules in the films. This technique can be of high value to studies of the physics of flow and of individual biomolecules.

Sheiko and coworkers have developed a technique for visualizing flows of polymer brush monolayers using atomic force microscopy.⁶ The conformations of the molecules were observed to depend on the pressure driving the flow and the frictional coefficient of the substrate.⁷ The flow coupled with adsorption of polymer side chains to the substrate resulted in ordering of the polymer backbones along a single axis⁸ and scission of the covalent bonds in the backbone⁹ at predictable points along the pressure gradient.¹⁰ During the research for this dissertation, preliminary work was performed in collaboration with the Sheiko group to

show how the electric field-driven wetting film flow system may be used to characterize flows of polymer monolayers. The polymer brushes were deposited in a hydrophilic channel on a patterned substrate, and atomic force microscopy was used to image the individual molecules, as shown in Figure 5.1. With this system, the effects of lateral confinement on the monolayers may be studied. The electric field may provide direct control over the flow or orientation of the molecules to further elucidate the relationship between molecular conformation and macroscopic flow behavior.

The platform may also facilitate bioanalytical procedures on individual molecules. Confinement in the film could force extension of DNA molecules for analysis.¹¹ Channel patterns could be designed to position molecules for individual base detection using demonstrated methods for single molecules based on fluorescence¹² or conductance.¹³ Electrophoretic separations of very small quantities of biomolecules could also be implemented in this device using the dc field applied along the film.

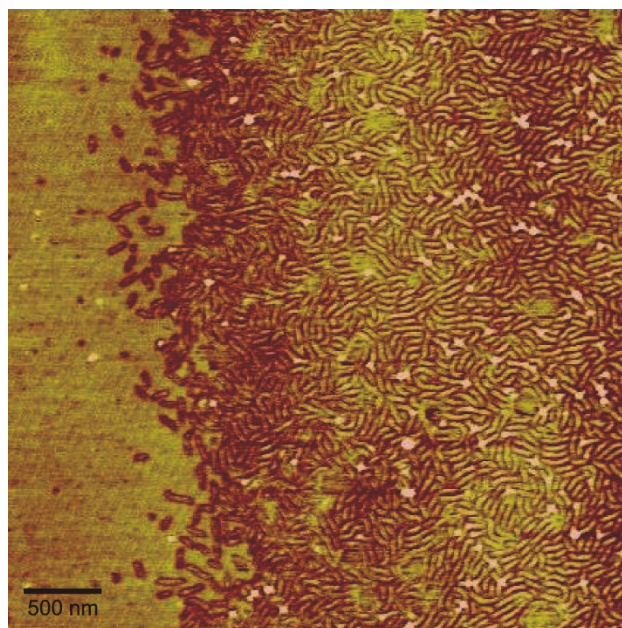


Figure 5.1. Atomic force micrograph of polymer brushes (right) moving along the wall of a “virtual channel” (left).

5.3 References

1. Ruschak, K. J. *Annu. Rev. Fluid Mech.* **1985**, *17*, 65–89.
2. Prevo, B. G.; Fuller, J. C.; Velev, O. D. *Chem. Mater.* **2005**, *17*, 28–35.
3. Jerrim, L. B.; Velev, O. D. *Langmuir*, **2009**, *25*, 5692–5702.
4. Mittal, M.; Furst, E. M. *Adv. Mater.* **2009**, *19*, 3271–3278.
5. Halsey, T. C. *Science* **1992**, *258*, 761–766.
6. Sun, F.; Sheiko, S. S.; Möller, M.; Beers, K.; Matyjaszewski, K. *J. Phys. Chem. A* **2004**, *108*, 9682–9686.
7. Xu, H.; Sun, F. C.; Shirvanyants, D. G.; Rubinstein, M.; Shabratov, D.; Beers, K. L.; Matyjaszewski, K.; Sheiko, S. S. *Adv. Mater.* **2007**, *19*, 2930–2934.
8. Xu, H.; Sheiko, S. S.; Shirvanyants, D.; Rubinstein, M.; Beers, K. L.; Matyjaszewski, K. *Langmuir* **2006**, *22*, 1254–1259.
9. Sheiko, S. S.; Sun, F. C.; Randall, A.; Shirvanyants, D.; Rubinstein, M.; Lee, H.; Matyjaszewski, K. *Nature* **2006**, *440*, 191–194.

10. Park, I.; Shirvanyants, D.; Nese, A.; Matyjaszewski, K.; Rubinstein, M.; Sheiko, S. S. *J. Am. Chem. Soc.* **2010**, *132*, 12487–12491.
11. Krishnan, M.; Mönch, I.; Schwille, P. *Nano Lett.* **2007**, *7*, 1270–1275.
12. Braslavsky, I.; Hebert, B.; Kartalov, E.; Quake, S. R. *P. Nat. Acad. Sci. USA* **2003**, *100*, 3960–3964.
13. Xu, B.; Zhang, P.; Li, X.; Tao, N. *Nano Lett.* **2004**, *4*, 1105–1108.